UCID-21195

The LLNL Sonic Probe for In-situ Stress Measurements

— A Progress Report on the Second-Generation Tool —

Nai-hsien Mao

Prepared for
Morgantown Energy Technology Center
Morgantown, WV

September 1987

Lawrence Livermore National Laboratory

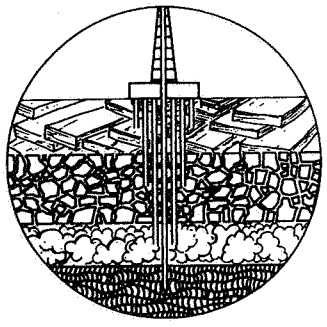

Unconventional Gas Program

Eastern Devonian Shales Research

DISCLAIMER

Printed in the United States of America
Available from
National Technical Information Service
U.S. Department of Commerce
5285 Port Royal Road
Springfield, VA 22161

Price Code	Page Range
A01	Microfiche
Papercopy Prices	
A02	001-050
A03	051-100
A04	101-200
A05	201-300
A06	301-400
A07	401-500
A08	501-600
A09	601

CONTENTS

ABSTRACT

The Lawrence Livermore National Laboratory's Unconventional Gas Program is pursuing the development of a borehole sonic tool to estimate in-situ rock stresses. A first-generation probe was developed in 1981-83 and the concept was confirmed in laboratory tests in large rock blocks. A patent (U.S. Patent No. 4,641,520) for the technique and apparatus was issued by the United States Patent and Trademark Office on February 10, 1987.

The second-generation LLNL sonic in-situ stress probe system was developed in 1984-86. It consists of the new LLNL sonic in-situ stress probe, a new data acquisition system which includes a Tektronix 7D20 digitizer, and new software to control it. Twelve cylindrical wedge transducers in 4 groups were embedded in a polyurethane loading cell. Each group has one transmitter and two receivers. From the travel time difference and the separation of the two receivers, absolute velocities can be calculated. New equations for back-calculation of stresses were derived to take the advantage of these absolute velocity measurements. The probe is also equipped with a dual pressurization system so that the pressures behind the transducers and bladder are separately controlled. The new system was assembled and checked in the laboratory, and then an initial field test of the modified probe was carried out at the Climax mine, Nevada Test Site, Nevada. This report discusses the new stress probe system, the laboratory test results, and the field test results. Recommendations are made for further development.

LIST OF FIGURES

LIST OF TABLES

1. INTRODUCTION

This research is a part of the Unconventional Gas Program at LLNL (Heuze, 1986). This report summaries the progress of the continued development of a borehole ultrasonic stressmeter at LLNL. In a previous study (Mao et al., 1983), a first-generation probe was built, and it was demonstrated in the laboratory that stresses in a large rock block under boundary loads could be back-calculated from measured stress-induced velocity anisotropy around a borehole drilled in the block. A patent for the technique and apparatus was issued by the United States Patent and Trademark Office (Mao, 1987). This report gives the rationale for improving the original system, describes the new stress tool system, and relates the results of the new laboratory tests and of the first field trial.

2. RATIONALE FOR THE MODIFICATIONS

Previous experience indicated that modifications could be made in at least three areas; i.e., the data acquisition system, the travel time measurement, and the velocity-pressure calibration approach to gain more control and to obtain better results.

The second-generation LLNL sonic in-situ stress probe has twelve transducers in four groups. Each group has one transmitter and two receivers. All the transducer housings are embedded in a polyurethane loading cell with a maximum capacity of 10,000 psi (69 MPa) (Figure 1).

2.1 Data Acquisition System

Previous experiment used a boxcar integrator (PAR Model 160) to sample the signal and to average it for digitization. One major problem with a boxcar integrator is the control of a common trigger time for all files; in the previous version, the trigger used a mechanical switch. It would be more desirable for the trigger system to be electronically controlled by software. The new system selected is a Tektronix 7D20 Digitizer; it is a plug-in unit for the Tektronix 7000 series oscilloscope. This configuration gives a fully

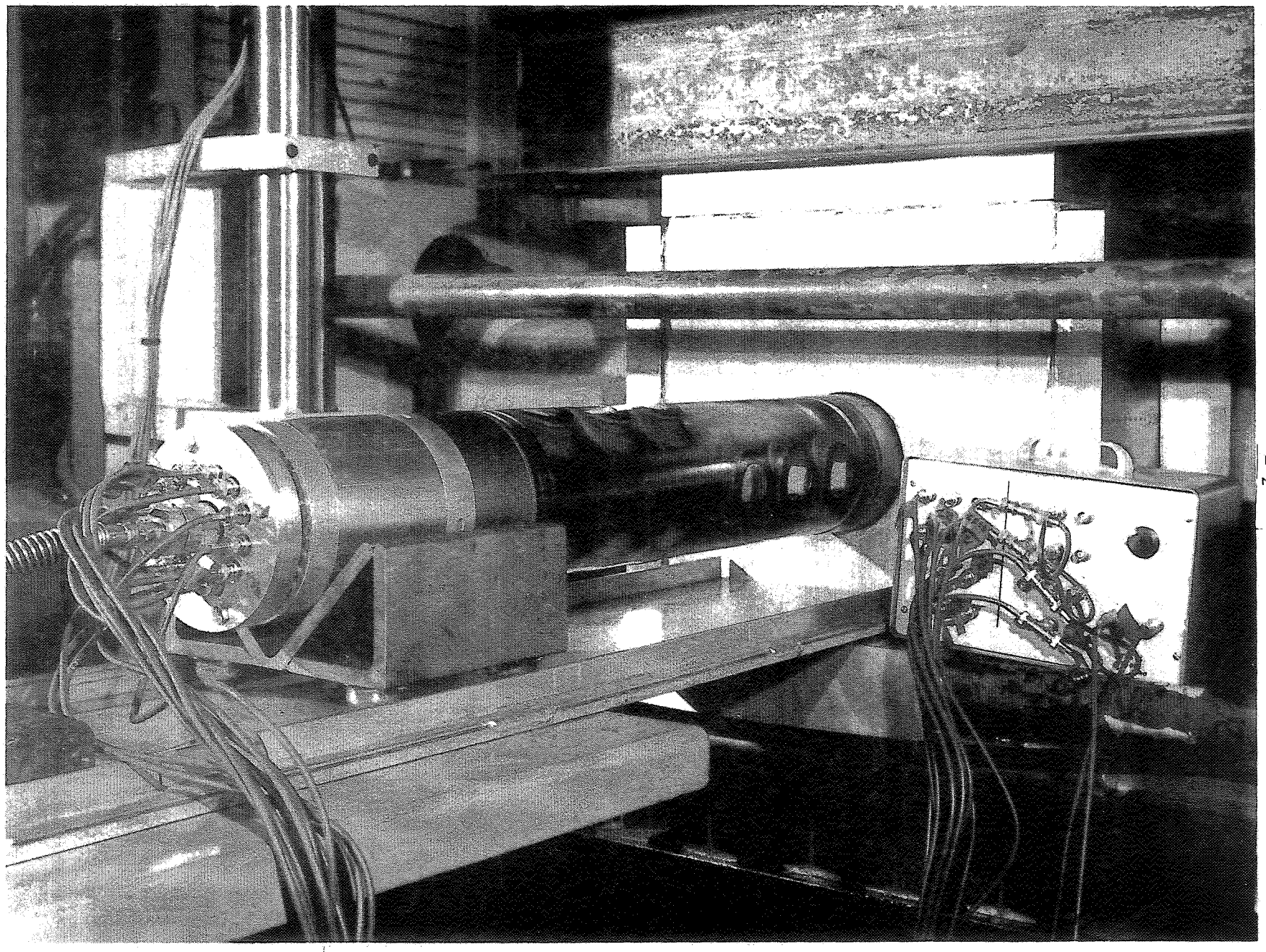

Figure 1. The LLNL sonic in-situ stressmeter.

programmable digitizing oscilloscope. It allows control not only of the relative trigger time for different files but also of the absolute trigger time for each signal. It also has signal averaging capability and memory to store and display up to 6 waveforms.

A new data acquisition computer program was written, as well (Christensen 1986). The software runs on a LSI-11 mini computer and controls both the Tektronix digitizing oscilloscope and the Hewlett-Packard 3497A Data Acquisition Control Unit (DACU), through the General Purpose Interface Bus (GPIB). The program reads data from the pressure gages and the load cells, using the 3497A DACU, and displays these data on a CRT. This mode continues until the user presses an "s" key to store the information. The program, then, initializes the 7D20 Digitizer to parameters that have been selected to ensure the proper triggering of the oscilloscope. The operator can choose to change the attributes, such as triggering, acquire, readout, and cursor, or to store the cursor waveform of the 7D20 on the hard disk of LSI-11. The storage of the waveform also includes information about all attributes. After the waveform is stored, the 3497A DACU reads the pressure gage and load cell data again and stores these new readings at the end of the file. Therefore, one can check whether the pressure gage and load cell readings are stable during the waveform digitization.

2.2 Absolute Travel Time Measurement

The approach used for the in-situ stress measurement is to back-calculate the stresses from the stress-induced velocity anisotropy around a borehole. In the early experiments, only relative travel time between different orientations or different loading conditions was measured. However the equations used for the back calculation of stresses are in terms of relative velocity changes; thus one had to make an additional approximation to justify using travel time instead of velocity for data reduction. The new probe has two receivers for each set of transducers. This allows measurements of absolute travel time, thus absolute velocity, for each orientation or loading condition.

2.3 In Situ Calibration

For field measurements, the measured stress-induced velocity anisotropy is obtained under a particular stress condition. In order to determine the magnitude of the stress, one has to measure the velocity-stress coupling coefficients. One way to carry out the calibration is to measure it on oriented cores in the laboratory. However there are drawbacks for this approach: first, microfractures generated during coring may change the acoustic property of the rock too much to recover its in-situ character; and secondly, it is generally very expensive to have an oriented core. Another way to measure the velocity-stress coupling coefficients is to pressurize the hole with a bladder system and measure the pressure effects in-situ. We chose the later approach.

3. EQUATIONS USED FOR STRESS CALCULATION

Most equations used in the report on the first-generation probe (Mao et al., 1983) are still valid. However, we modified some of them because of the change in loading condition due to the bladder system.

For a circular hole with the long axis in the z-direction in an isotropic material, the radial (σ_r) and tangential (σ_θ) stresses can be expressed as functions of the principal stresses (Timoshenko and Goodier, 1951) as shown in Figure 2:

$$\sigma_r = \frac{\sigma_x + \sigma_y}{2} \left[1 - \left(\frac{r_i}{r}\right)^2\right] + \frac{\sigma_x - \sigma_y}{2} \left[1 + 3\left(\frac{r_i}{r}\right)^4 - 4\left(\frac{r_i}{r}\right)^2\right] \cos 2\theta \qquad (1)$$

$$\sigma_\theta = \frac{\sigma_x + \sigma_y}{2} \left[1 + \left(\frac{r_i}{r}\right)^2\right] - \frac{\sigma_x - \sigma_y}{2} \left[1 + 3\left(\frac{r_i}{r}\right)^4\right] \cos 2\theta \qquad (2)$$

where σ_x and σ_y are the two principal stresses in the x-y plane, r_i is the radius of the hole, and θ is the angle counterclockwise from the x-direction.

For $r = r_i$,

$$\sigma_r(r=r_i) \; 0 \qquad (3)$$

$$\sigma_\theta(r=r_i) = (\sigma_x + \sigma_y) - 2(\sigma_x - \sigma_y) \cos 2\theta \qquad (4)$$

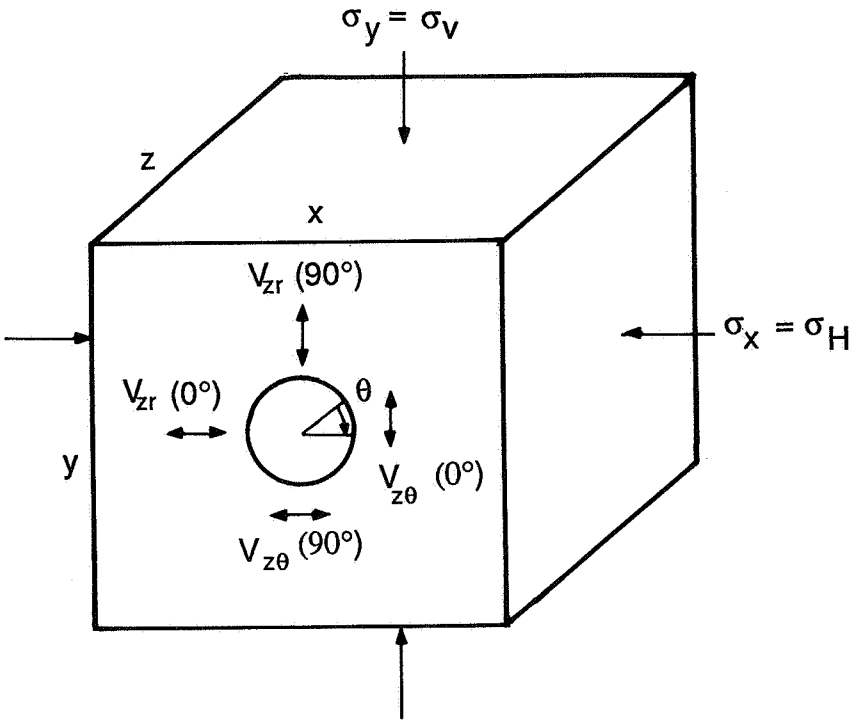

Figure 2. Coordinates for stresses in a laboratory setup.

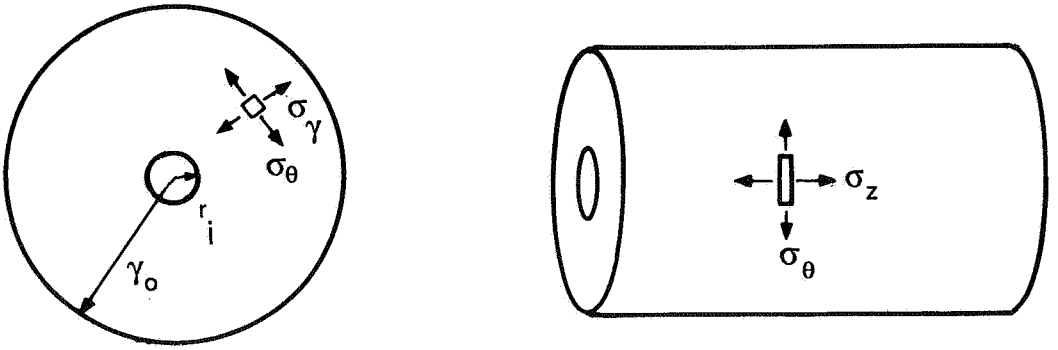

Figure 3. Coordinates for a thick-wall cylinder.

If we have a thick wall cylinder (see Figure 3) with inner radius r_i and outer radius r_o, and internal pressure P, then the radial and tangential stresses (σ_r and σ_θ) due to P are (Miller and Doeringsfeld, 1955):

$$\sigma_r = \frac{P(r_i^2)}{(r_o^2 - r_i^2)} \left[\left(\frac{r_o}{r}\right)^2 - 1\right] \tag{5}$$

$$\sigma_\theta = \frac{-P(r_i^2)}{(r_o^2 - r_i^2)} \left[\left(\frac{r_o}{r}\right)^2 + 1\right] \tag{6}$$

where tension is negative and compression is positive.

For $r = r_i$,

$$\sigma_r\ (r = r_i) = P \tag{7}$$

$$\sigma_\theta\ (r = r_i) = -P\ \frac{r_o^2 + r_i^2}{r_o^2 - r_i^2} \tag{8}$$

The total stresses will be the combination of the effects both due to the external loading and internal pressure. By combining Eqs. 3 and 7 and Eqs. 4 and 8, we have:

$$\sigma_r(r = r_i) = P \tag{9}$$

$$\sigma_\theta(r = r_i) = \left(-P\ \frac{r_o^2 + r_i^2}{r_o^2 - r_i^2} + \sigma_x + \sigma_y\right) - 2\ (\sigma_x - \sigma_y)\ \cos 2\theta \tag{10}$$

Eqs. 9 and 10 imply that for a given external loading and orientation, both σ_r and σ_θ are proportional to the applied internal pressure. For a laboratory setup of r_i=3" and r_o=9.5", assuming σ_x=1000 psi (6.9 MPa), σ_y=2000 psi (13.8 MPa), P varies from 0 to 1000 psi (0 to 6.9 MPa), we have

$$R = \frac{r_o^2 + r_i^2}{r_o^2 - r_i^2} = 1.222$$

and

$$\sigma_r\ (r = r_o) = P \tag{11}$$

$$\sigma_\theta\ (r = r_o) = (3000 - 1.222\ P) + 2000\ \cos 2\theta \tag{12}$$

Figure 4 shows the results of Eqs. 11 and 12 where σ_r increases with P and σ_θ decreases with P but in a slightly larger rate. Therefore we expect that V_{zr} will increase with P and $V_{z\theta}$ will decrease with P.

For field test, r_o approaches infinity. Thus R = 1. The stresses change due to P will be the same for both σ_r and σ_θ, but they will be in opposite directions.

4. STRESS EFFECT ON SOUND WAVE VELOCITIES

Under triaxial loading, for sound waves propagating in the principal stress z-direction, $\sigma_x \neq \sigma_y \neq \sigma_z \neq 0$ in general. The total stress effect on velocity is the linear combination of the stress effects due to all components loaded individually (Mao et al., 1983). The linear equations for the velocities in the principal stress directions are:

$$\begin{aligned} V_{zz}^2 &= V_{zzo}^2 + A_{zz}\,\sigma_x + B_{zz}\,\sigma_y + C_{zz}\,\sigma_z \\ V_{zx}^2 &= V_{zxo}^2 + A_{zx}\,\sigma_x + B_{zx}\,\sigma_y + C_{zx}\,\sigma_z \\ V_{zy}^2 &= V_{zyo}^2 + A_{zy}\,\sigma_x + B_{zy}\,\sigma_y + C_{zy}\,\sigma_z \end{aligned} \tag{13}$$

where V_{ij} is the velocity of a body wave propagating in the i-direction with particle motion in the j-direction and V_{ijo} is the stress-free velocity. A_{ij}, B_{ij}, and C_{ij} are the velocity stress coupling coefficients for the principal stresses in the x-, y-, and z-directions. For isotropic solids, $C_{zx} = C_{zy}$, $A_{zz} = B_{zz}$, $A_{zx} = B_{zy}$, and $A_{zy} = B_{zx}$.

Consider the elastic waves traveling in the z-direction along the axis of the borehole (Figure 2). The body wave velocities are V_{zz}, V_{zr}, and $V_{z\theta}$ for the compressional wave, the radially polarized shear wave, and the tangentially polarized shear wave, respectively. Under triaxial loading, the stress effect on velocity should have the following form (Mao et al., 1983):

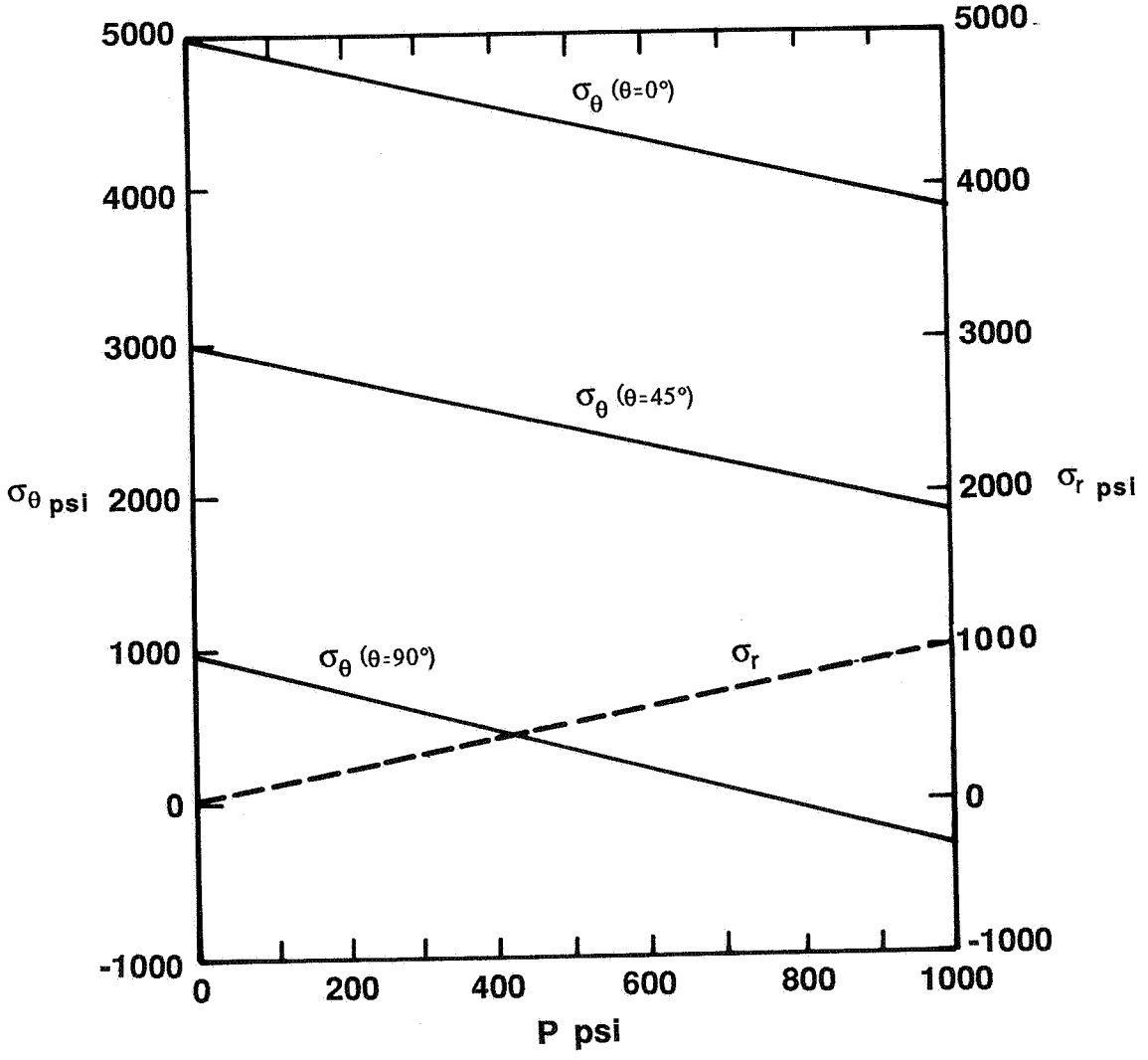

Figure 4. Stresses vs internal pressure for a thick-wall cylinder.

$$V_{z\theta}^2\,(0°) - V_{z\theta o}^2\,(0°) = A\sigma_\theta(0°) + B\sigma_r\,(0°) + C\sigma_z(0°) \tag{14}$$

$$V_{z\theta}^2\,(90°) - V_{z\theta o}^2\,(90°) = A\sigma_\theta(90°) + B\sigma_r(90°) + C\sigma_z(90°) \tag{15}$$

$$V_{zr}^2\,(0°) - V_{zro}^2\,(0°) = A\sigma_r(0°) + B\sigma_\theta\,(0°) + C\sigma_z(0°) \tag{16}$$

$$V_{zr}^2\,(90°) - V_{zro}^2\,(90°) = A\sigma_r(90°) + B\sigma_\theta(90°) + C\sigma_z(90°) \tag{17}$$

where $\sigma_z(0°) = \sigma_z(90°)$ and for $r = r_i$, $\sigma_r = 0$. Furthermore, for a homogeneous material, $V_{zro}(0°) = V_{z\theta o}(90°)$, and $V_{zro}(90°) = V_{z\theta o}(0°)$.

Thus for Eqs. (14) - (17), we have

$$V_{z\theta}^2\,(0°) - V_{zr}^2\,(90°) = A\sigma_\theta\,(0°) - B\sigma_\theta\,(90°) \tag{18}$$

For Eqs. (15) - (16), we have

$$V_{z\theta}^2\,(90°) - V_{zr}^2\,(0°) = A\sigma_\theta\,(90°) - B\sigma_\theta\,(0°) \tag{19}$$

For Eqs. (18) - (19), we have

$$V_{z\theta}^2\,(0°) - V_{zr}^2\,(90°) - V_{z\theta}^2\,(90°) + V_{zr}^2\,(0°)$$

$$= (A+B)\,[\sigma_\theta\,(0°) - \sigma_\theta\,(90°)] \tag{20}$$

For Eqs. (18) + (19), we have

$$V_{z\theta}^2\,(0°) - V_{zr}^2\,(90°) + V_{z\theta}^2\,(90°) - V_{zr}^2\,(0°)$$

$$= (A-B)\,[\sigma_\theta\,(0°) + \sigma_\theta\,(90°)] \tag{21}$$

From Eq. (4), we have

$$\sigma_\theta\,(0°) - \sigma_\theta\,(90°) = -\,4\,(\sigma_x - \sigma_y)$$

$$\sigma_\theta\,(0°) + \sigma_\theta\,(90°) = 2\,(\sigma_x + \sigma_y)$$

Therefore Eq. (20) is

$$\sigma_x - \sigma_y = \frac{1}{4(A+B)} \{ [V_{z\theta}^2 (90°) - V_{zr}^2 (0°)] - [V_{z\theta}^2 (0°) - V_{zr}^2 (90°)] \} \quad (22)$$

and Eq. (21) is

$$\sigma_x + \sigma_y = \frac{1}{2(A-B)} \{ [V_{z\theta}^2 (90°) - V_{zr}^2 (0°) + [V_{z\theta}^2 (0°) - V_{zr}^2 (90°)] \} \quad (23)$$

Let

$$\Delta V_a^2 = V_{z\theta}^2 (90°) - V_{zr}^2 (0°)$$

$$\Delta V_b^2 = V_{z\theta}^2 (0°) - V_{zr}^2 (90°)$$

then from Eqs. (22) + (23), we have

$$\sigma_x = \frac{1}{8(A^2-B^2)} [(3A +B) \Delta V_a^2 + (A + 3B) \Delta V_b^2] \quad (24)$$

From Eqs. (23) - (22), we have

$$\sigma_y = \frac{1}{8(A^2-B^2)} [(A + 3B) \Delta V_a^2 + (3A +B) \Delta V_b^2 \quad (25)$$

Therefore, from Eqs. (24) and (25) if we know A and B and measure ΔV_a^2 and ΔV_a^2, we can back-calculate σ_x and σ_y . It is worth noting that ΔV_a^2 and ΔV_b^2 are velocity differences of different modes and of different orientations. It is only possible to measure these differences when we can measure the absolute velocities.

5. LABORATORY TEST OF THE MODIFIED STRESSMETER-PROBE

The probe shown on Figure 1 was designed and fabricated by Serata Geomechanics, Inc. It was tested and calibrated at LLNL. It was designed for 6" diameter holes, which is the typical size used as the overcoring hole for the U.S. Bureau of Mines (USBM) Borehole Deformation Stress Gage. Thus one can field this probe in a hole where in-situ stresses were determined from the USBM gage measurements, and compare the two sets of results. Twelve cylindrical wedge transducers in 4 groups are embedded in a inflatable polyurethane loading cell which has a maximum capacity of 10,000 psi (69 MPa) and can be used to measure the stress-velocity relationship in-situ. We calibrated the bladder system in a 6" diameter steel tube up to 6000 psi (41.4 MPa) and found no leakage. The laboratory setup is shown in Figure 5. The probe was later retrofitted for a dual pressurization system so that the pressures behind transducers and bladder are separately controlled. Each group has one transmitter and two receivers. From the travel time difference and the separation of the two receivers, absolute velocities can be calculated. As stated earlier, this provides much better stress estimates due to less assumptions involved. Figure 6a shows the waveforms from both the near and the far pairs measured within a hole of a large block of Nugget sandstone. Figure 6b shows the cross-correlation results. The calculated velocities are 2.350 and 2.326 km/s for tangentially and radially polarized shear waves respectively.

The orientation of applied stresses can be estimated from the measured velocity anisotropy around a hole. Figure 7 shows a plot of relative travel time of tangentially polarized shear waves as a function of transducer orientation. A vertical load of 1000 psi (6.9 MPa) and a horizontal load of 2500 psi (17.24 MPa) were applied. The orientation of 90° was located at the bottom of the hole, and 0° and 180° were both horizontal. As expected the velocity at 90° was the fastest of all. Should we not know the stress orientation, we would choose 90° as one of the principal stress direction.

Figures 8a to 8d show the received signals generated from the 12 transducers embedded in urethane placed inside a 6" hole of a large block of Nugget sandstone. Figures 8a and 8b are two sets of data from radially polarized transducers positioned 90° to each other. Similarly Figures 8c and 8d are two

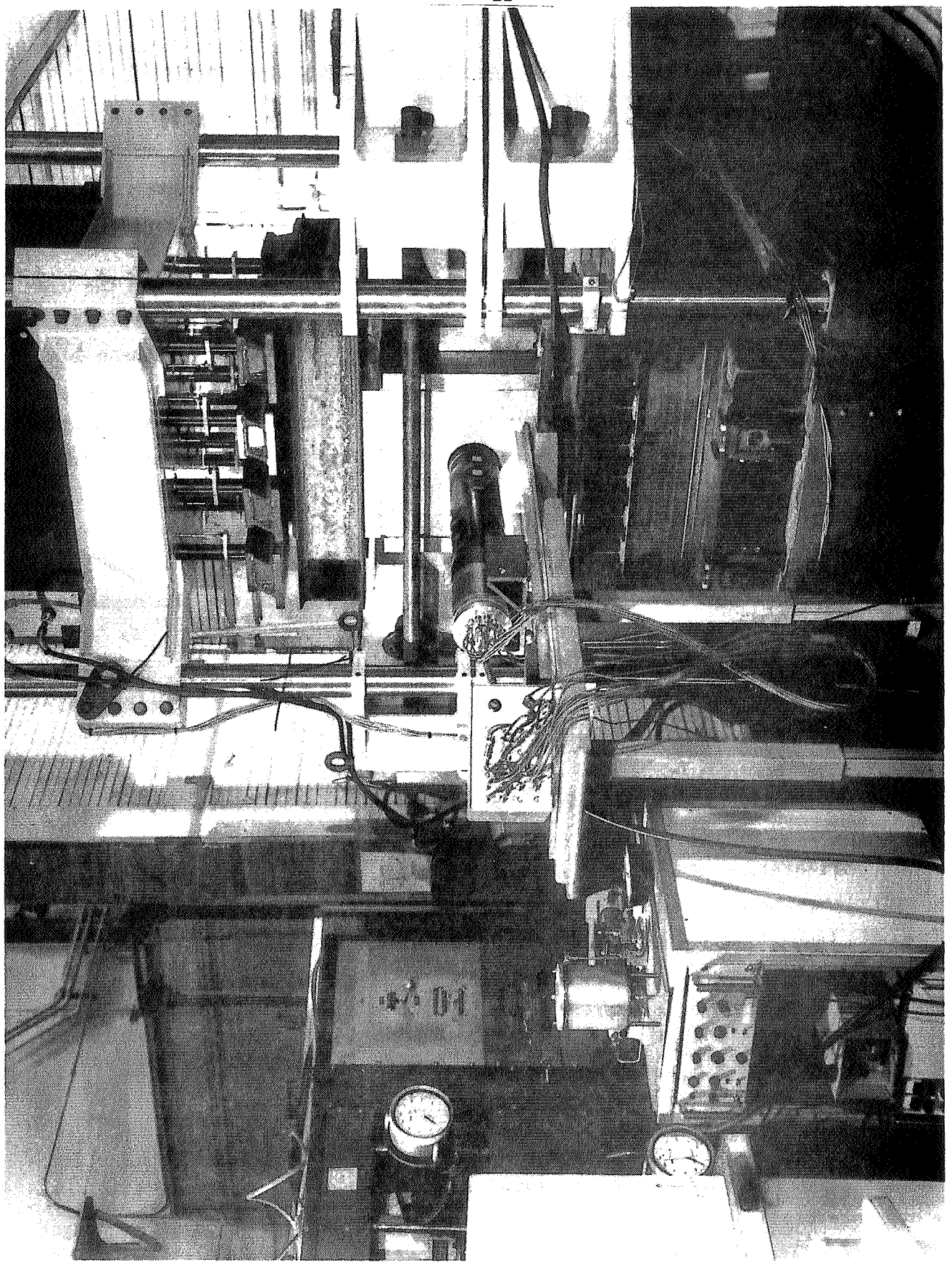

Figure 5. The LLNL sonic in-situ stressmeter in a laboratory setting.

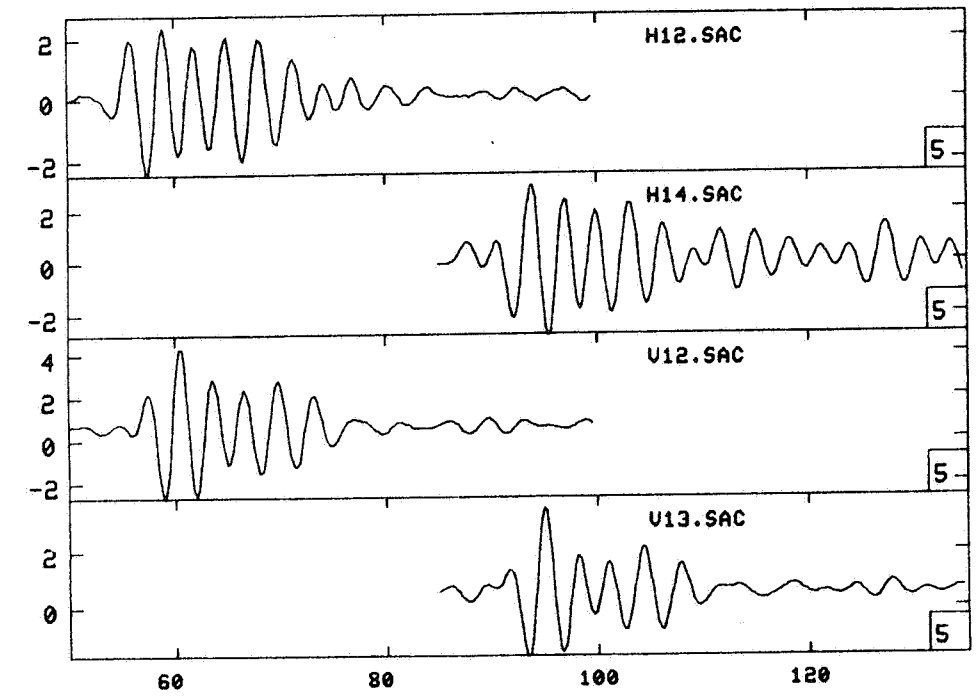

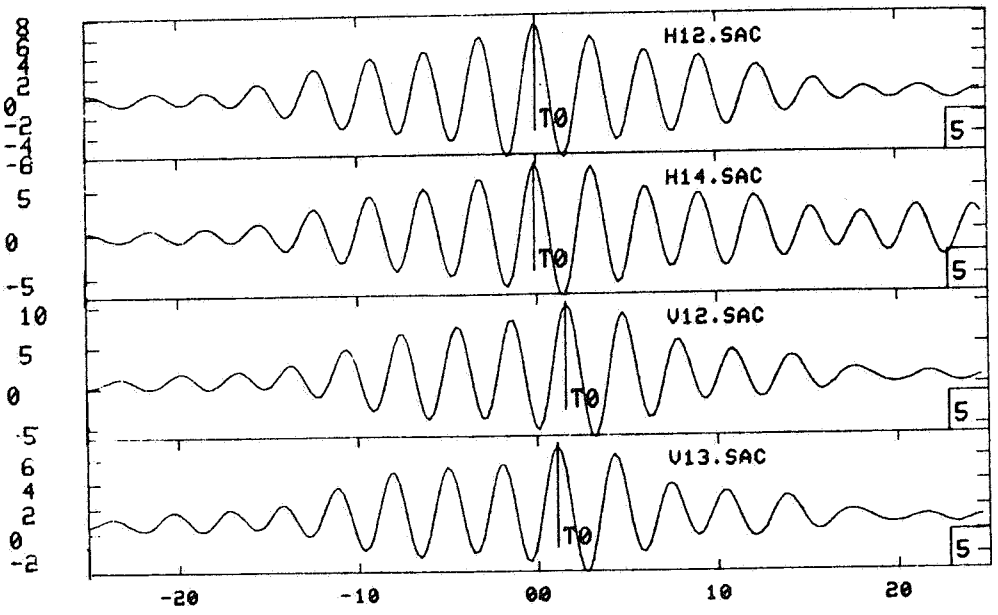

Figure 6. The travel time data from both near and far pair transducers.

a. waveform.

b. cross-correlation results.

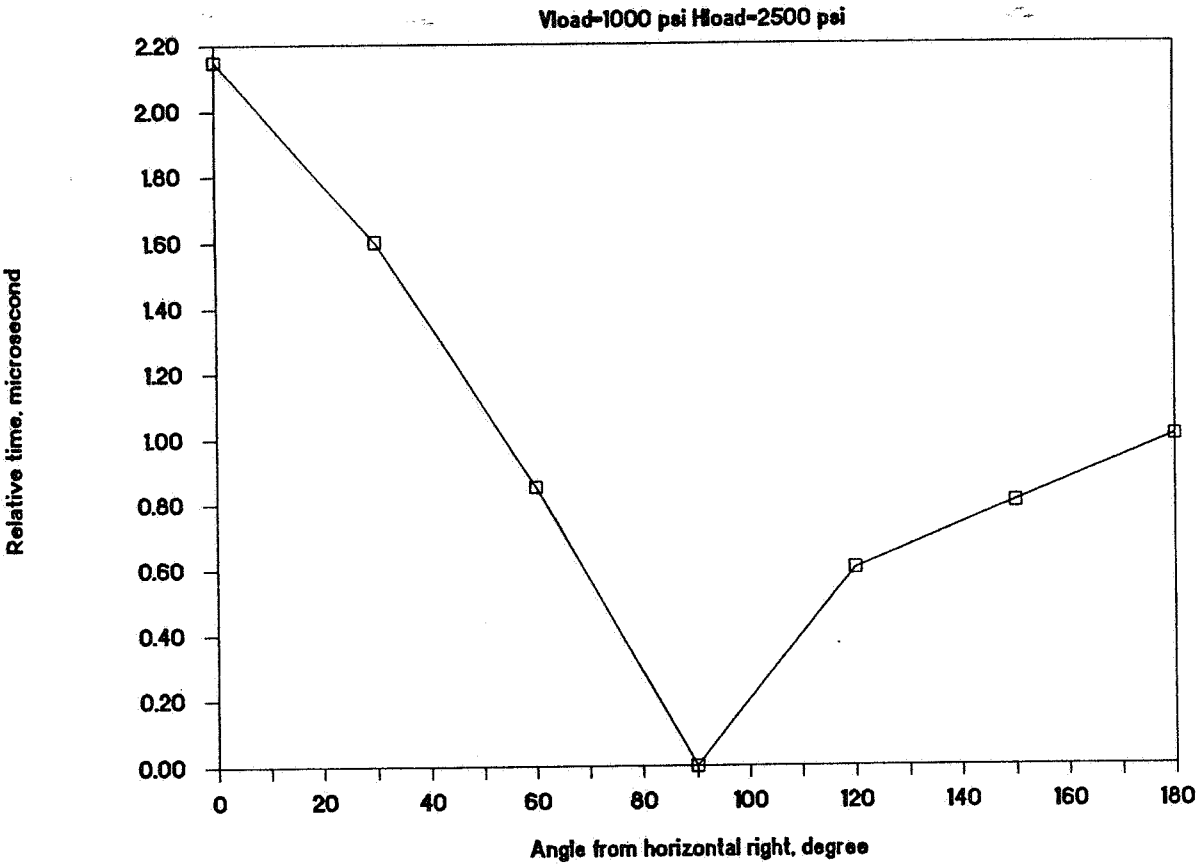

Figure 7. Relative travel time of tangentially polarized shear wave as a function of transducer orientation.

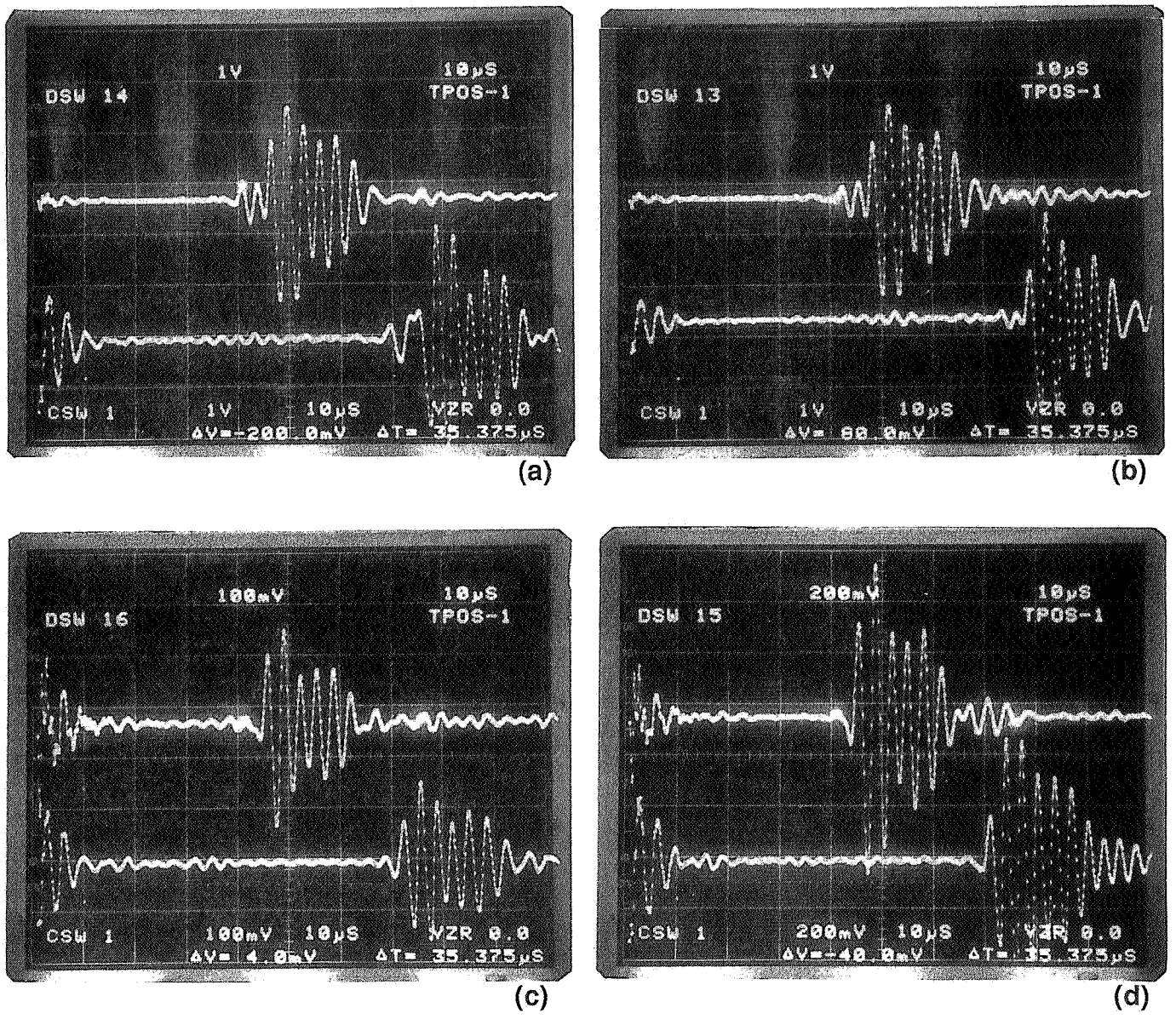

Figure 8. Waveforms generated from 12 transducers inside a 6" hole of a large block of Nugget Sandstone.

a. from radially polarized transducers at 0°.

b. from radially polarized transducers at 90°.

c. from tangentially polarized transducers at 0°.

d. from tangentially polarized transducers at 90°

sets of data from tangentially polarized transducers positioned at 90° to each other. There are two signals for each sets, i.e., the far pair and the near pair. The waveforms of all received signals are very similar. Thus it ensures good results for estimating the travel time difference using a cross-correlation technique.

6. FIELD TESTING AT THE CLIMAX MINE

6.1 The Climax Mine

The Climax Mine is located 420 m below the surface in the Climax granite stock at the Nevada Test Site (NTS), Nevada. It was used as a generic test site for the Spent Fuel Test. Over 900 data channels were installed to monitor the response of the rock to the heat, radiation, and stress changes. Among these studies, the U. S. Bureau of Mines Borehole deformation gage and the Australian CSIRO Hollow Inclusion Stress Cell were used to measure in-situ stresses (Creveling et al., 1984) and IRAD GAGE vibrating-wire stressmeters were installed in the facility to measure the change in in-situ stress (Mao, 1984). The hole selected for the field test is a horizontal hole located in the pillar of the north heater drift (Figure 9). Creveling et al. (1984), reported that the major secondary principal stress is predominantly vertical and has a maximum value of no more than 2000 psi (13.8 MPa); the minimum secondary principal stress is nearly horizontal and is generally less than 700 psi (4.83 MPa). IRAD gages are commonly used to monitor the in-situ stress changes. However, if the gage rock interface is preserved through overcoring, together with subsequent laboratory calibration under biaxial condition, the IRAD data can be used to estimate the magnitude of in-situ stresses as well. Such estimated stresses were in good agreement with those measured by borehole deformation gage (Mao, 1984).

6.2. Operating Procedure

The proposed operating procedure for a field test is:

* Select a 6" hole, preferably an overcoring hole for the USBM gage. Examine the hole with a borescope to locate a section of the hole for test. This section should be as smooth and void of fractures as possible for optimum probe seating in the hole.

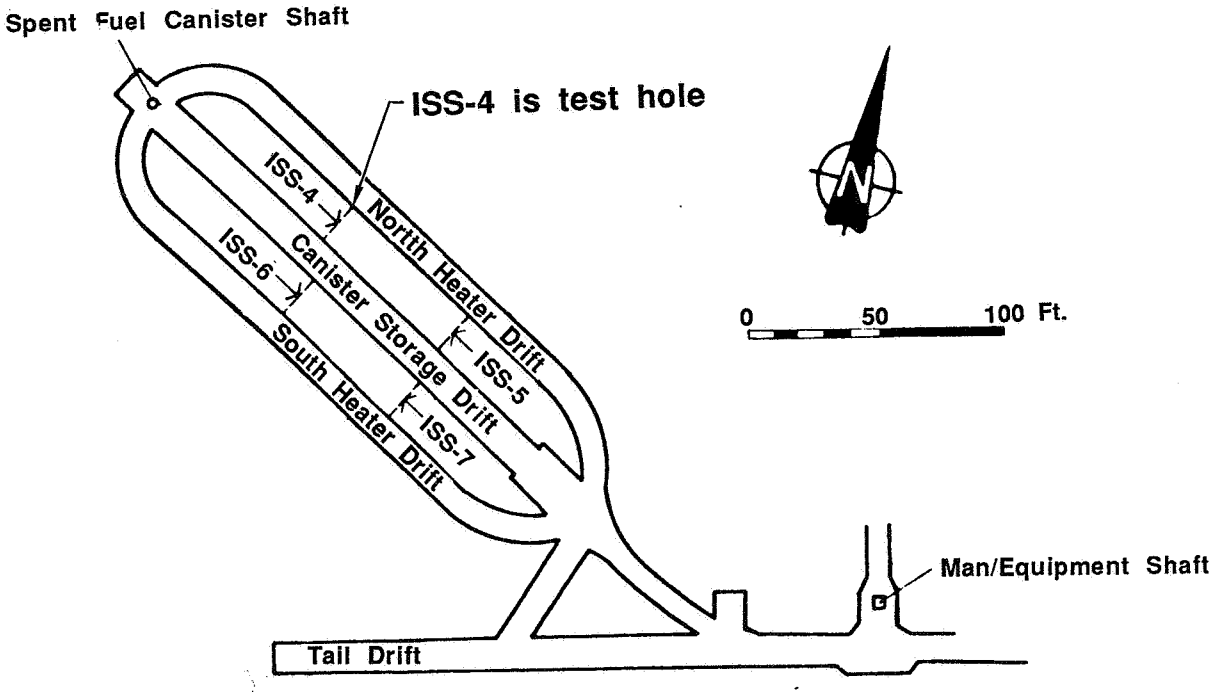

Figure 9. Map of the Climax Mine.

* Insert the probe into the hole and measure the travel times as a function of orientation in an increment of 30°, to cover at least 180°.

* Plot the measured travel times as a function of orientation to determine the locations for the maximum and minimum travel time. These orientations are assumed to be the secondary principal stress directions.

* Realign the transducers according to the determined orientation and measure the travel times from all pairs of transducers as their initial readings.

* Increase the bladder pressure and measure the pressure effect on travel time.

* Analyze data using cross-correlation.

* Compare back-calculated stresses with previous measurements.

For the initial field test at the Climax mine, the main purpose was to test the performance of the probe rather than the procedure. Since the orientation of the secondary principal stresses at the test hole was known from previous results, we decided to align the probe in those directions and to measure the absolute travel time and its pressure effect first. The main reason for doing this is to avoid repositioning of the transducers at the beginning of the test.

6.3. Field Data

The field test at Climax was carried out from May 12 to May 16, 1986, in the horizontal hole (ISS-4) shown on Figure 9. The field setup is shown on Figures 10a and 10b. Difficulties with the tool in the beginning were mainly due to poor electrical connection of the wires either in the transducers or inside the bladder. We managed to repair all of them in the field. However when the stressmeter was emplaced in the hole, the signals from one set of

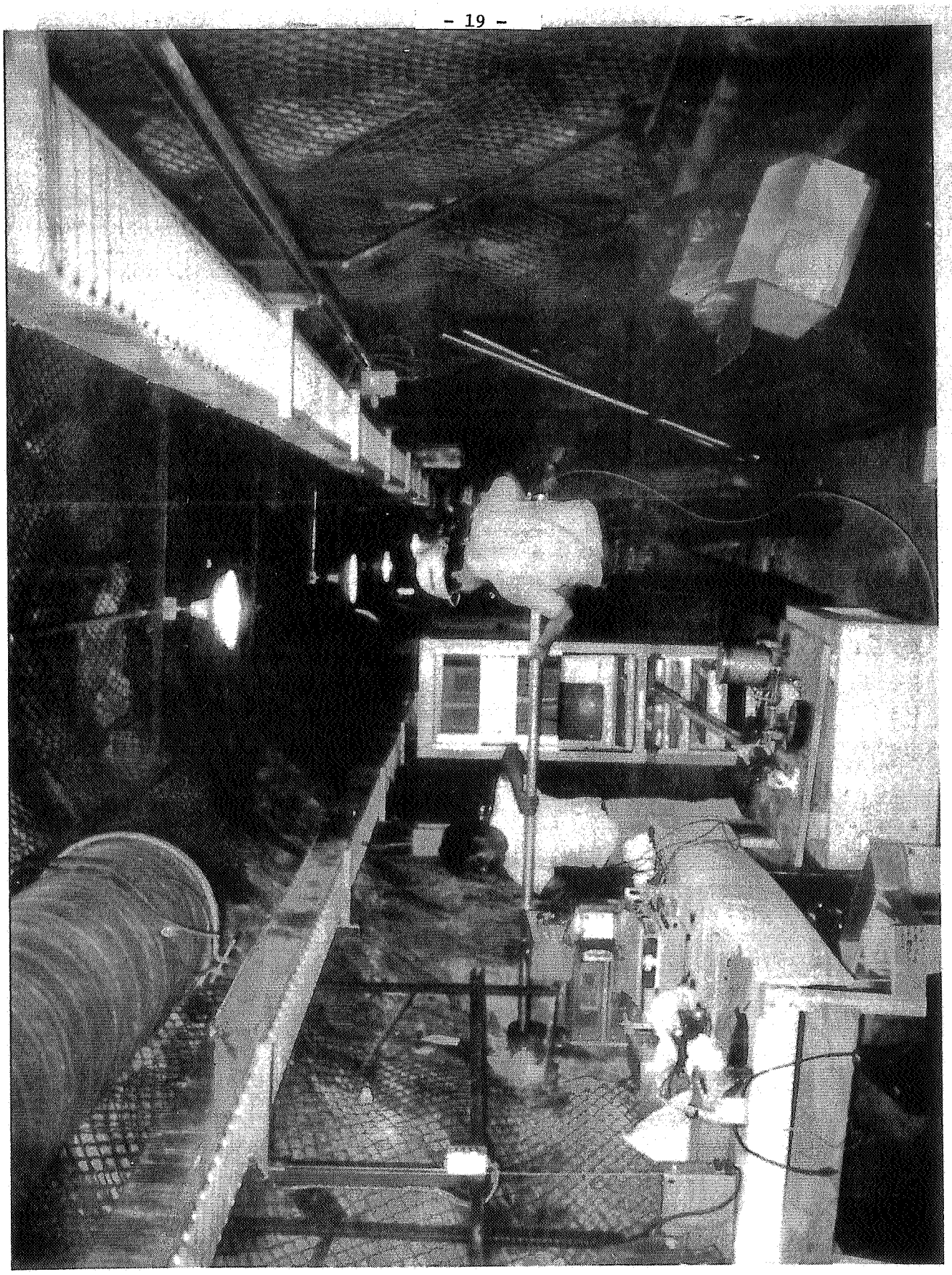

Figure 10a. Field set up of stressmeter.

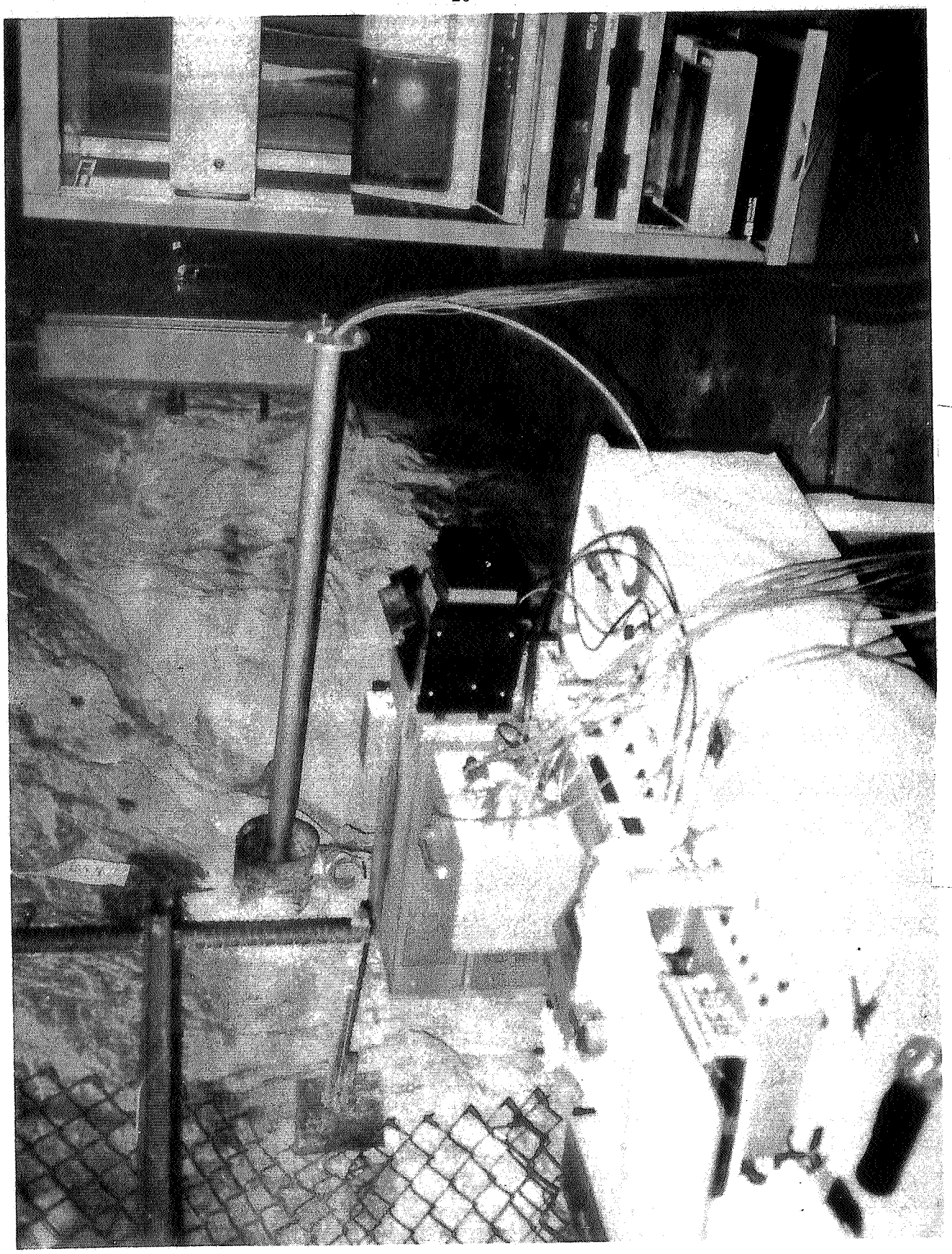

Figure 10b. Field set up of stressmeter.

polarized transducers were lost, possibly due to the failure of the transmitter. Because of time constraints (the Climax mine was being reopened for only a few days), we decided to proceed with only 3 sets of transducer working. A total of 58 files were taken to determine the stress effects on velocities and the velocity anisotropy around the hole. The bladder was pressurized in 500 psi (3.45 MPa) increments up to 3000 psi (20.69 MPa). The dual pressurization system worked fine.

We took two types of data. One type includes the absolute velocity and the pressure effect on velocities. For this type of measurement, the transducers were fixed in position while the pressure was changed. The second type of data is the orientational effect on velocities. We repositioned the transducers clockwise every 30 degree for each set of data. The waveforms of this type of data often change from measurement to measurement because of the change of coupling between transducer and rock, after repositioning.

Figure 11 shows the locations of the transducers. There are 4 sets of transducers in the stressmeter. Each set consists of one transmitter and two receivers. The transmitters are always near the center. For future reference, the file names are designed to show the type of measurement, which transducers are involved, the location of transducers, and the pressure. The first letter indicates the type of measurement where C is for pressure records and D is for orientation records. This is followed by two digits to indicate the transmitter and the receiver. We used "01" and "02" to indicate "10 to 11" and "10 to 12". For type C records the 4th symbol is a letter indicating the location of the transducers: D for down, U for up, and R for right. In the D records, the fourth symbol is always the letter C (for clockwise). The last two digits are the pressure in 100 psi (0.69 Mpa) (i.e., 05=500 psi (3.45 MPa) etc.) for C records, or amounts of 10 degrees (i.e., 06=60 degree, etc.) from vertical up for D records. This labeling is repeated in the legend to the tables summarizing the data.

The field data were recorded on a LSI-11 computer. At LLNL, this information was transferred to a PRIME computer via a CDC 7600 computer. All the timing analyses of the data were performed on the PRIME computer.

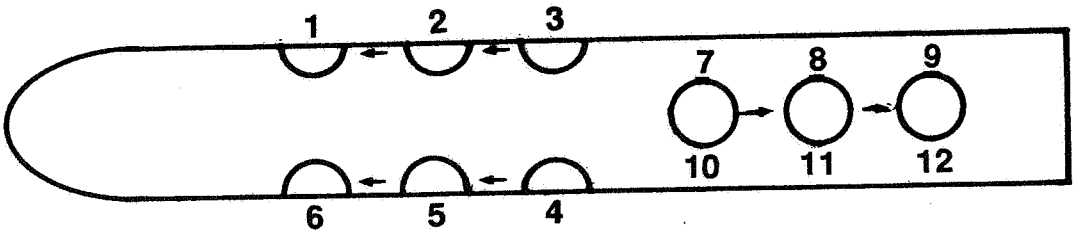

Figure 11. Transducer locations of LLNL stress probe.

7. ANALYSIS OF FIELD TEST DATA

Close examination of the digitized data indicates that

* The quality of the field data varies from record to record.

* Some discrepancies were found between the digitized data and the original Polaroid picture of the waveform on the scope just before digitization. Figure 12a shows the original scope picture of C31D00 and Figure 12b shows the digitized data of the same waveform. Approximately 7 microseconds of record are missing from the digitized data. In another case (C64U00) a discrepancy of 1.9 microsecond was observed (Figure 13). The discrepancy also exists for other records but generally is less than 1 microsecond.

* Some inconsistencies were observed for redundant data.

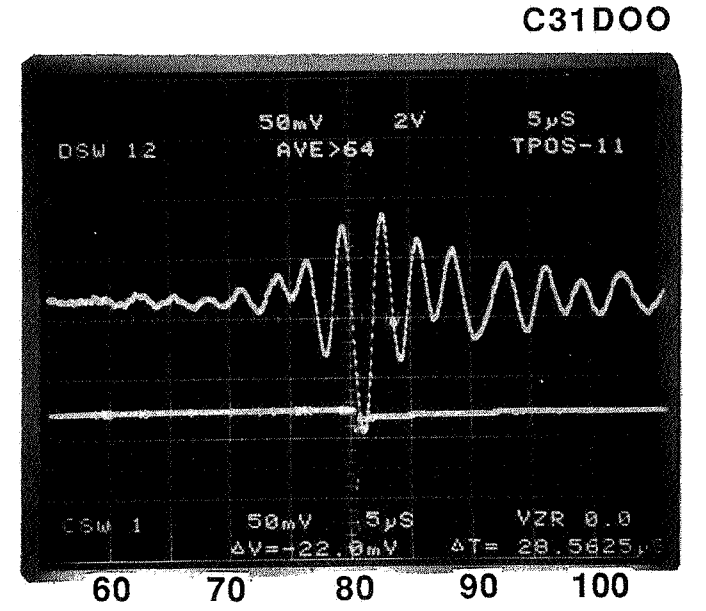

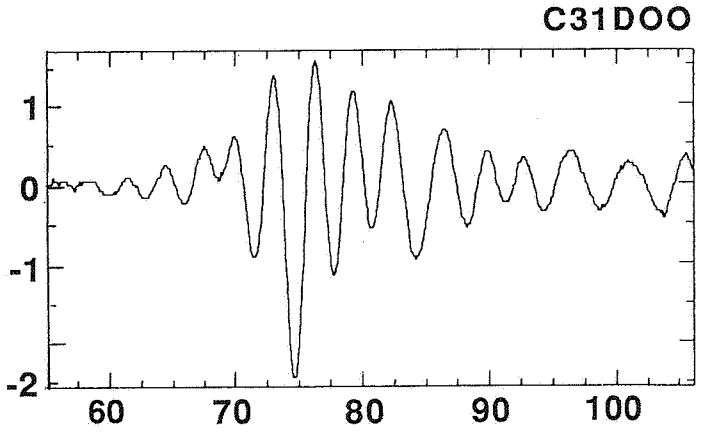

Figure 12. Timing discrepancy for C31D00

a: Polaroid picture before digitization.

b: Digitized waveform.

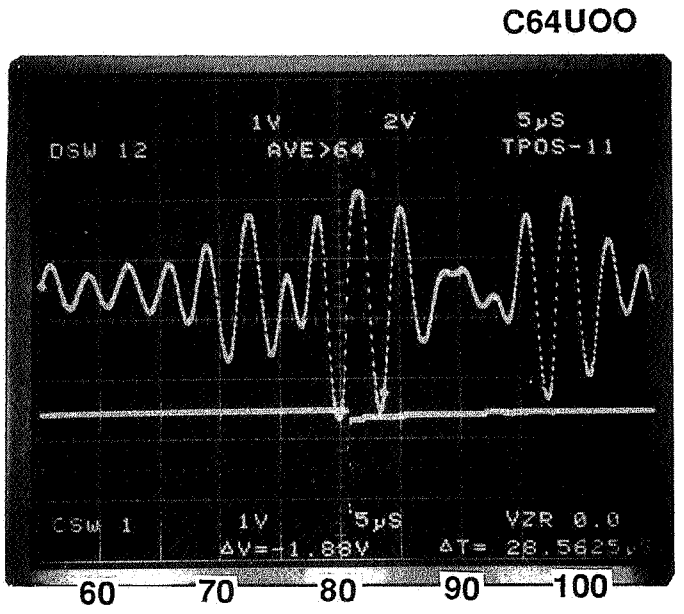

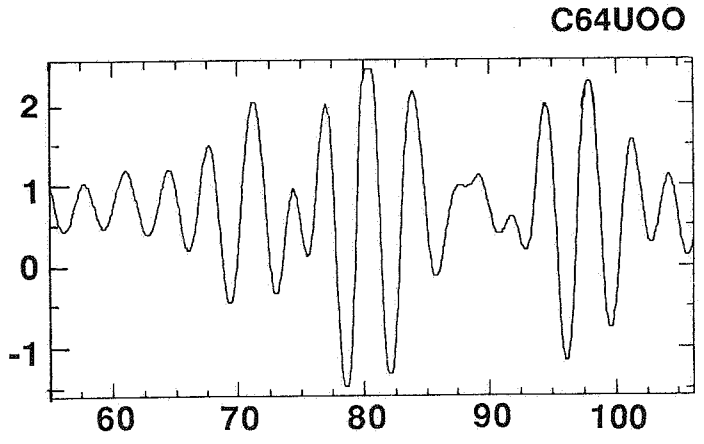

Figure 13. Timing discrepancy for C64U00.

a: Polaroid picture before digitization.

b: Digitized waveform.

After extensive analysis, we finally identified the causes of the timing error for the field data. Two types of error were found: timing errors due to operational mistake and systematic error generated by the data acquisition program. The general procedure used to digitize the waveform consists of the following steps:

* Select the transducer pair.

* Set trigger to external and positive slope.

* Average the signal and switch on HOLD to freeze the waveform.

* Run the digitizing program.

It turned out that the default setting of the trigger mode in the data acquisition program is "trigger by channel 1". The program switches the trigger mode to channel 1 every time it is run. If this is not reset to external trigger before the next run, the digitized waveform is triggered from channel 1 rather than from external. The timing error from these two trigger modes depends on the signal of channel 1. A timing difference of 1.91 microsecond was obtained in a test run; this is comparable to the case for C64U00. Also if the trigger mode is external but the trigger slope is changed from positive on to positive off, a timing error of 8.6 microsecond is observed; this was likely the case for C31D00.

Furthermore, the digitized window is slightly larger than that indicated by the grid of the scope. For a time base of 5 microsecond per division, the grid indicates a window of 50 microsecond but the waveform has a span of 51.1875 microsecond. The data acquisition program digitizes the whole waveform but assumes that it only has a span of 50 microsecond. This explains those cases with a discrepancy of less than 1 microsecond between the Polaroid pictures and the plot of the digitized data. The correction factor is 51.1875/50=1.02375. Therefore all cross-correlation data should be multiplied by 1.02375. The timing error due to operational error was corrected by comparing the same peak on the Polaroid picture as that on the digitized

plot. This correction also contains a systematic error which depends on the location of the peak.

We corrected the system error of the field data by multiplying all raw data by a constant of 1.02375. The relative timing of all files was redetermined from the corrected data using cross-correlation technique. The results are shown in Appendices A and B. Appendix A contains all the plots of the raw waveforms and cross-correlation results. Appendix B contains all the Tables (1 through 4) of data from the cross-correlation results: i.e., the absolute velocity, the pressure effect, the orientation effect, and the waveform quality evaluation. The relative timing (DT) was determined by comparing the peaks of the cross-correlated files. The carrier frequency is 300 kHz which implies that the period is about 3.3 microsecond. If a peak is missed, it will result in an error of 3 to 4 microseconds. In the case of constant frequency, the time difference between peaks is a constant; however, if the frequency content of a wave train varies with time due either to interference or to other causes, then the time difference between two peaks will vary too. In Table 1 we have included the relative time determined from neighboring peaks under the headings of DT0, DT1, and DT2. T0, T1, and T2 are the calculated time difference from DT0, DT1, and DT2 respectively. T_{av} is the mean of the three calculated time differences. In many cases the mean values are more consistent. It should be noted that DT1 is the time difference determined from cross-correlation for the selected peak.

Table 1 shows the results for absolute velocities; a detailed legend explains the Table headings. The absolute velocity is calculated from the time difference between the far pair and the near pair of transducers. The calculated velocities under different pressures are also shown in this table. In each set of data, the files in the last row are D records which are the starting data for the orientation run after the pressure run. In other words, they are also the files of the end of the pressure run. In general the velocities at the beginning and the end of the pressure run show good agreement (1%) for the 0 and 180 degree cases, and a 3% difference for the 90 degree case. However, the pressure effect on the absolute velocities is not well represented. It seems that most of the effect occurs during the first 500 psi (3.45 MPa), with almost no effect for higher pressure. We will discuss the pressure effect in detail, later.

The results of pressure effect on travel time is shown in Table 2. There are three sets of data as in the case of absolute velocity. Each set has two groups one for the near pair and one for the far pair transducers. In general the pressure effect from the near pair is quite different from that from far pair and the pressure effect is seen largely only for the first 500 psi (3.45 MPa). There are several possible reasons for these irregularities. Note that the dual pressure system for the probe was designed to exclude the transducers from the probe pressure which is much much higher than that inside the transducer housing. This arrangement has no serious effect on the near pair of transducer, but it creates a non-uniform loading on the path between the transmitter and the receiver for the far pair. Furthermore the internal pressure system produces a relatively small pressure effect. As shown in Equations 11, 12 and Figure 7, internal pressure gives an increase in σ_r and a decrease in σ_θ. Since σ_r and σ_θ are opposite in sign, the combined pressure effect is the net effect and is smaller than that from either σ_r or σ_θ alone. It is also quite possible that the initial pressure effect is a result of crack closure. After crack closure, the pressure effect is much smaller and the quality of the present data set is not good enough to measure that effect.

In a homogeneous material, the velocity anisotropy around a borehole may be represented by an ellipse; hence the magnitude of the velocity is a periodic function with 180 degree lag. In other words the velocities from locations 180 degree apart should be equal. In Table 3, we also included the results from "reverse cross-correlation". For instance, in addition to the time difference between D32C18 and D32C21 etc, we also determined the time difference between D32C36 and D32C21 etc. By averaging these two sets of results, we forced the time difference between D32C18 and D32C36 to zero. This is shown in the last column under the subheading of Average. The results are also plotted in Figure 14 which shows the relative time change as a function of angle. Figure 14 indicates that the vertical and horizontal directions are the major directions of velocity anisotropy around the hole. These directions in turn coincide with the secondary principal stress directions from the USBM deformation gage results.

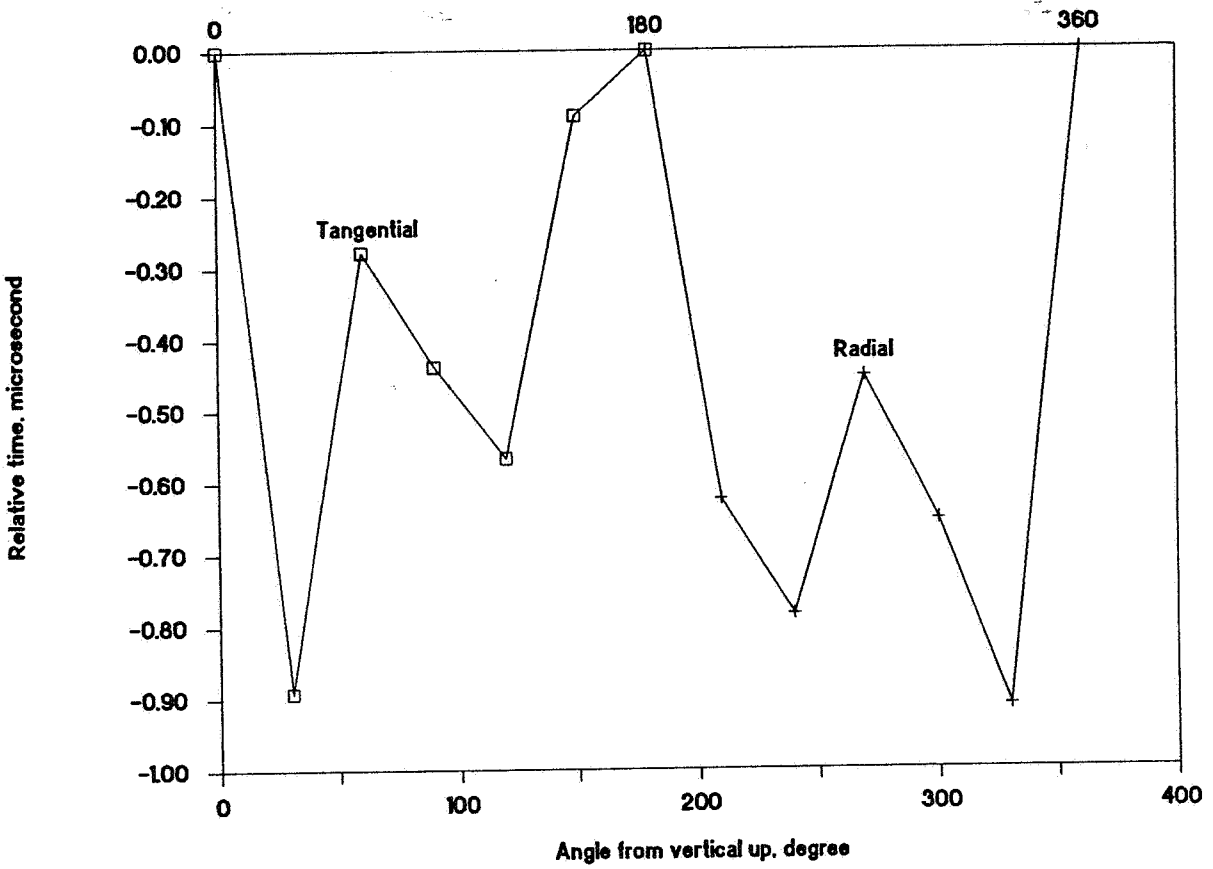

Figure 14. Orientational effect on travel time around the test hole.

Table 4 shows the results of comparison of redundant files. It is designed to show the degree of consistency of the data. The discrepancies range from -0.31 to 1.19 microsecond. Five out of ten pairs have a discrepancy less than 0.1 microsecond. The largest discrepancy of 1.19 microsecond is between D31C18 and C31D00 which has a time correction of 7.14 microsecond.

8. CONCLUSIONS AND SUMMARY

Results from field test indicate that

* the quality of the data varies greatly from file to file.

* the data contains many inconsistencies, even after the timing corrections.

* the data indicate inconsistent pressure effect. In some cases even the sign is different from the theoretically predicted one. Furthermore, all the pressure effects are seen only from the first 500 psi (3.45 MPa) pressure. The effect for pressure above 500 psi (3.45 MPa) is very small.

* the only information that could be extracted from these data is the orientation of the secondary principal stresses.

We cannot at present entirely explain the cause of the inconsistency. However, the failure of the redundant check within the data makes us wonder whether the inconsistency is due to inhomogeneity of the rock around the hole. There are large chunks of feldspar reported in Climax granodiorite. However, we did not see any through borescope when we examined the hole.

The results from field test exposed some shortcomings of the present system. However, the fundamental concept of measuring velocity anisotropy around a hole to estimate in-situ stresses is still a sound one. Some engineering problems regarding the transducers and bladder system would have

to be investigated and solved before attempting another field test. For instance, it would be highly desirable to have separate pressure control for each individual transducer. In this way, if the signals from a particular transducer is poor due to poor contact, we always can depressurize that particular transducer and pressurize it again to change the contact. The current probe may have enough room to handle 4 separate pressure lines but probably not 12 separate lines. The compromise is to make each group of transducers controlled by separate pressure lines. Another possible improvement is to dedicate one pressure run for the pulsed phase-lock loop technique (Mao et al. 1983). Pulsed phase-lock loop technique is particularly good for measuring the change of the lock-in frequency (proportional to the reciprocal of travel time) due to pressure change. However, it requires a continuous run. In other words, we can not shift from one set of transducers to another set after each pressure increment as we did during the field test.

In summary we have made progress in hardware design and we established an operating procedure. We also demonstrated the two-receiver system. However, during the field test in Climax we found that a dual pressurization system created some problems for the far pair transducers under pressure. Nevertheless, the pressure effect of the velocity can be measured from the near pair transducers only.

The results of the field test are inconclusive as far as the estimation of the magnitude of in-situ stresses is concerned. However, the orientation of the velocity anisotropy around the hole is consistent with that of the secondary principal stresses measured by USBM deformation gages.

9. APPENDIX A

Appendix A contains all the plots of the raw waveforms and the cross-correlation results. The upper plot shows the raw waveforms and the lower plot shows the cross-correlation results. In the cross-correlation plot, the top trace is the autocorrelation of the reference trace itself and the other traces show the time differences relative to the reference trace. The three peaks marked T0, T1, and T2 in the cross-correlation plots are the time differences shown in Table 1 as DT0, DT1, and DT2. They should not be confused with T0, T1, and T2 in Table 1.

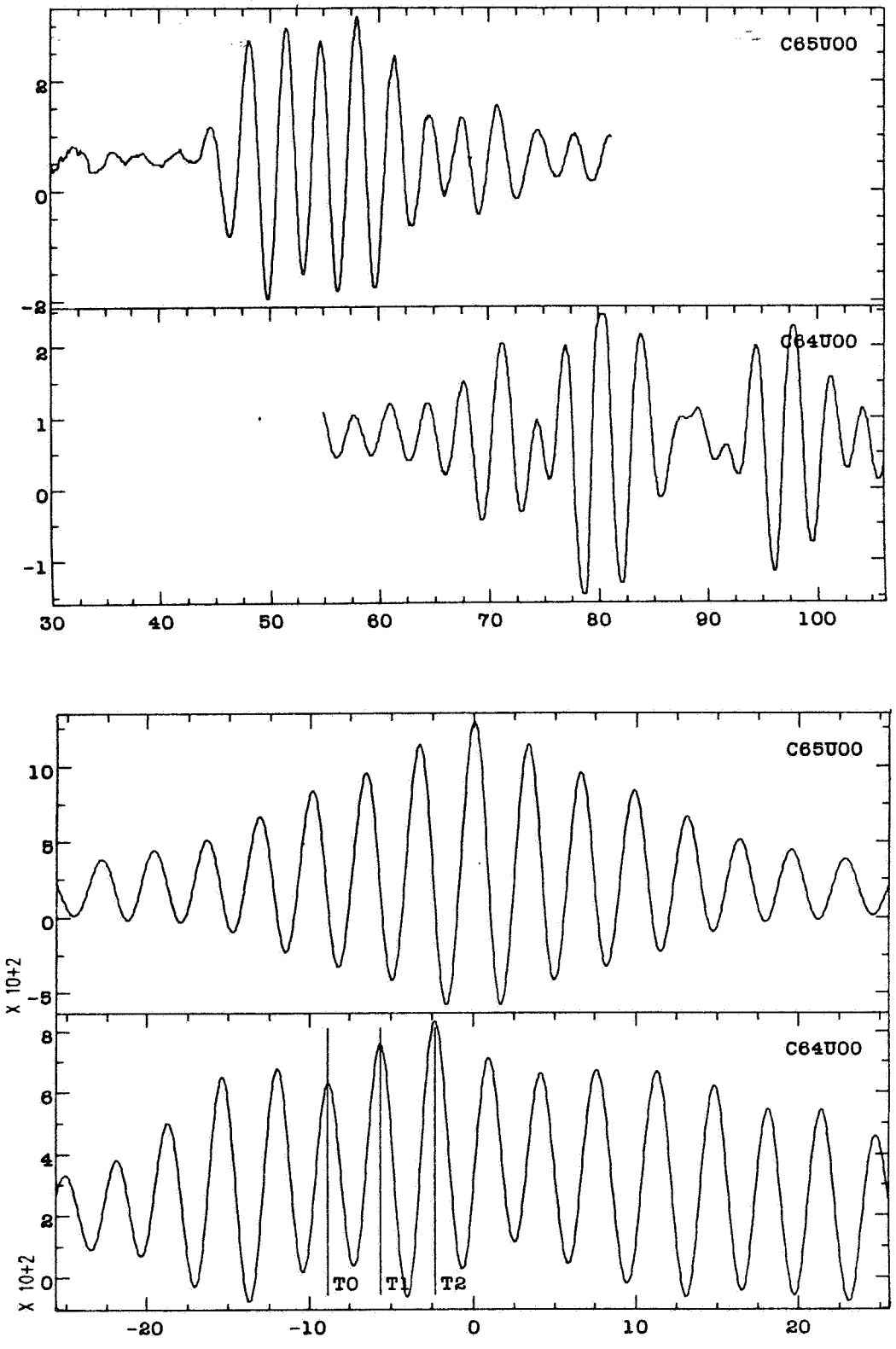

Records of C65U00 and C64U00. Upper plot shows the raw waveforms. Lower plot shows the cross-correlation results.

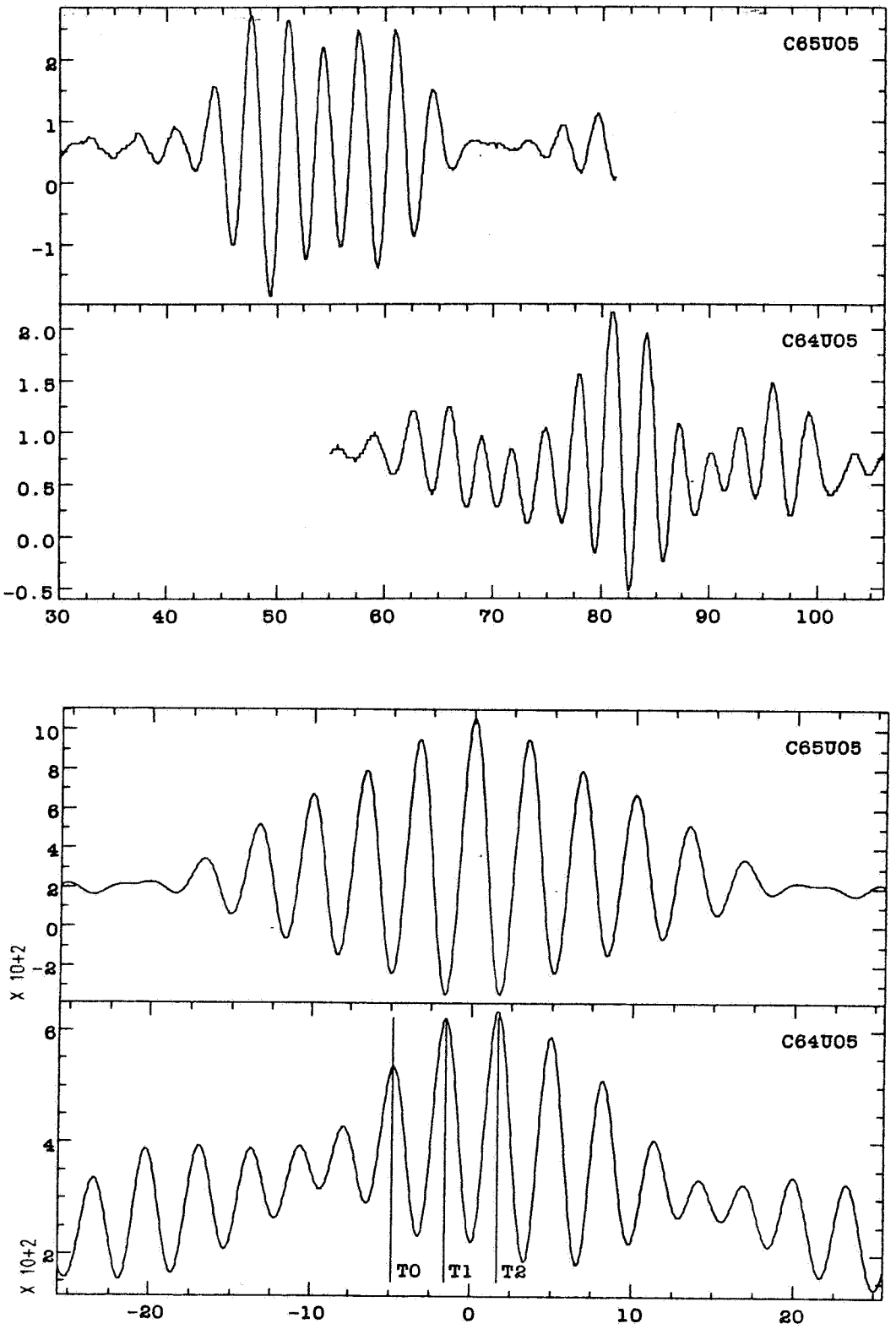

Records of C65U05 and C64U05. Upper plot shows the raw waveforms. Lower plot shows the cross-correlation results.

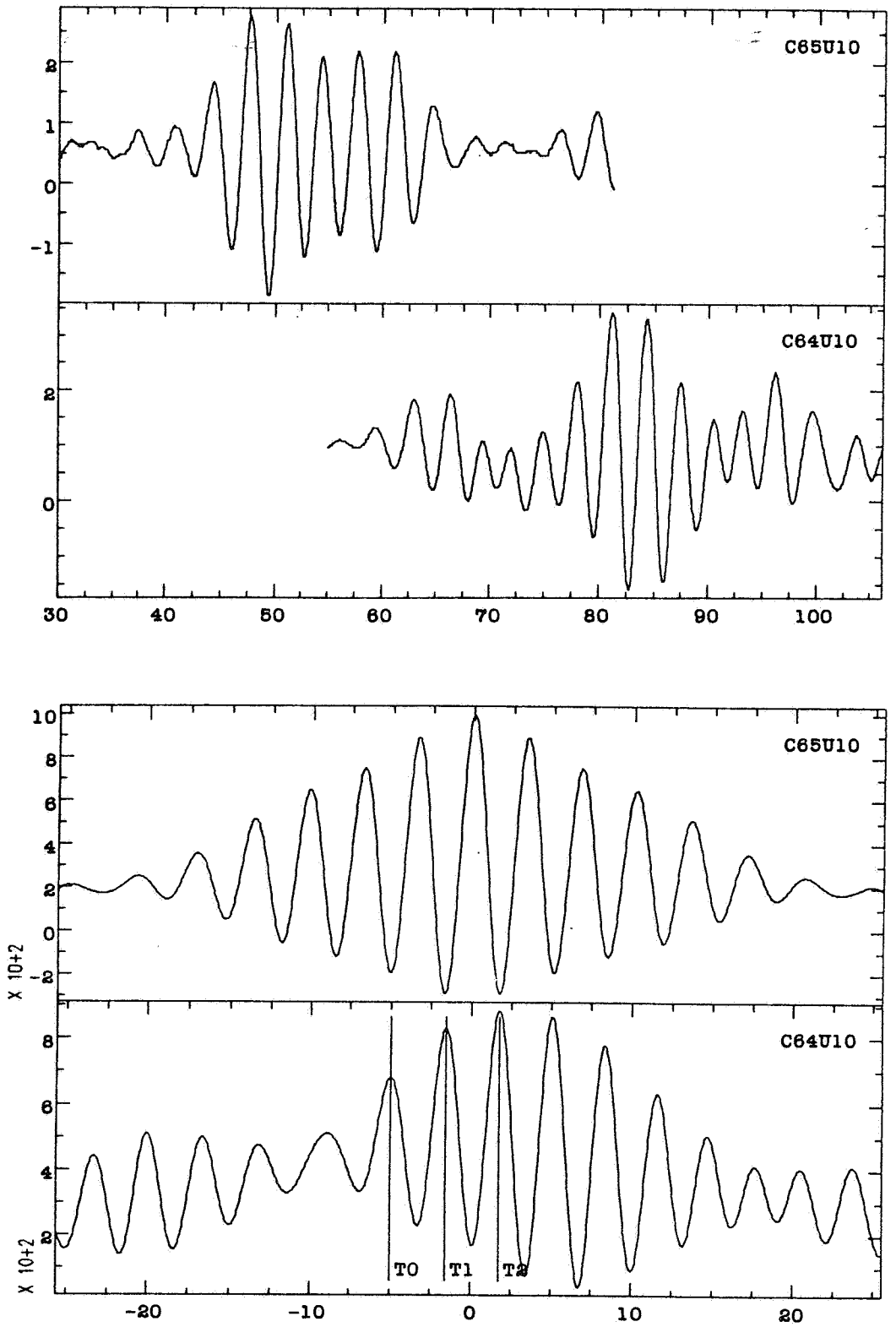

Records of C65U10 and C64U10. Upper plot shows the raw waveforms. Lower plot shows the cross-correlation results.

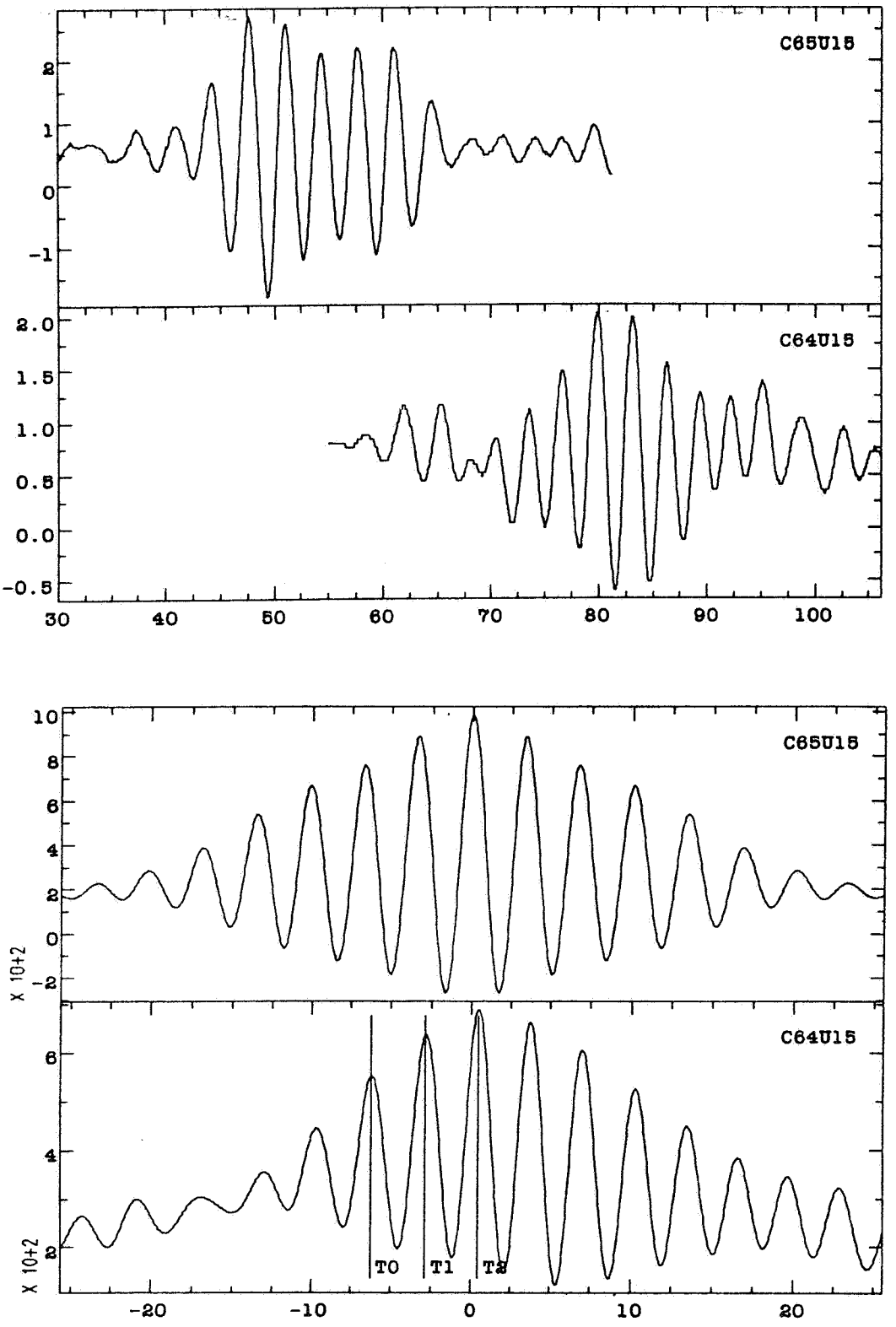

Records of C65U15 and C64U15. Upper plot shows the raw waveforms. Lower plot shows the cross-correlation results.

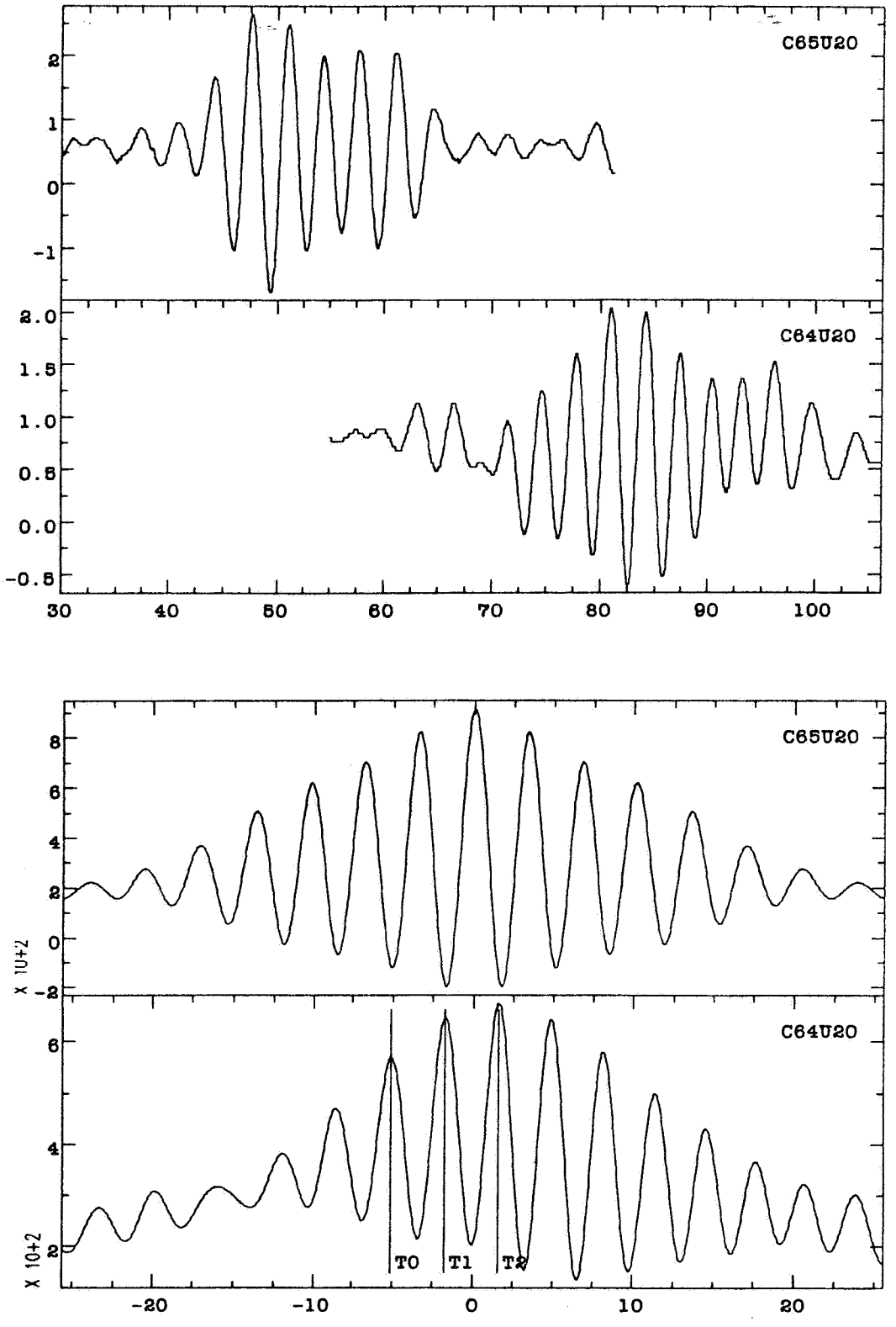

Records of C65U20 and C64U20. Upper plot shows the raw waveforms. Lower plot shows the cross-correlation results.

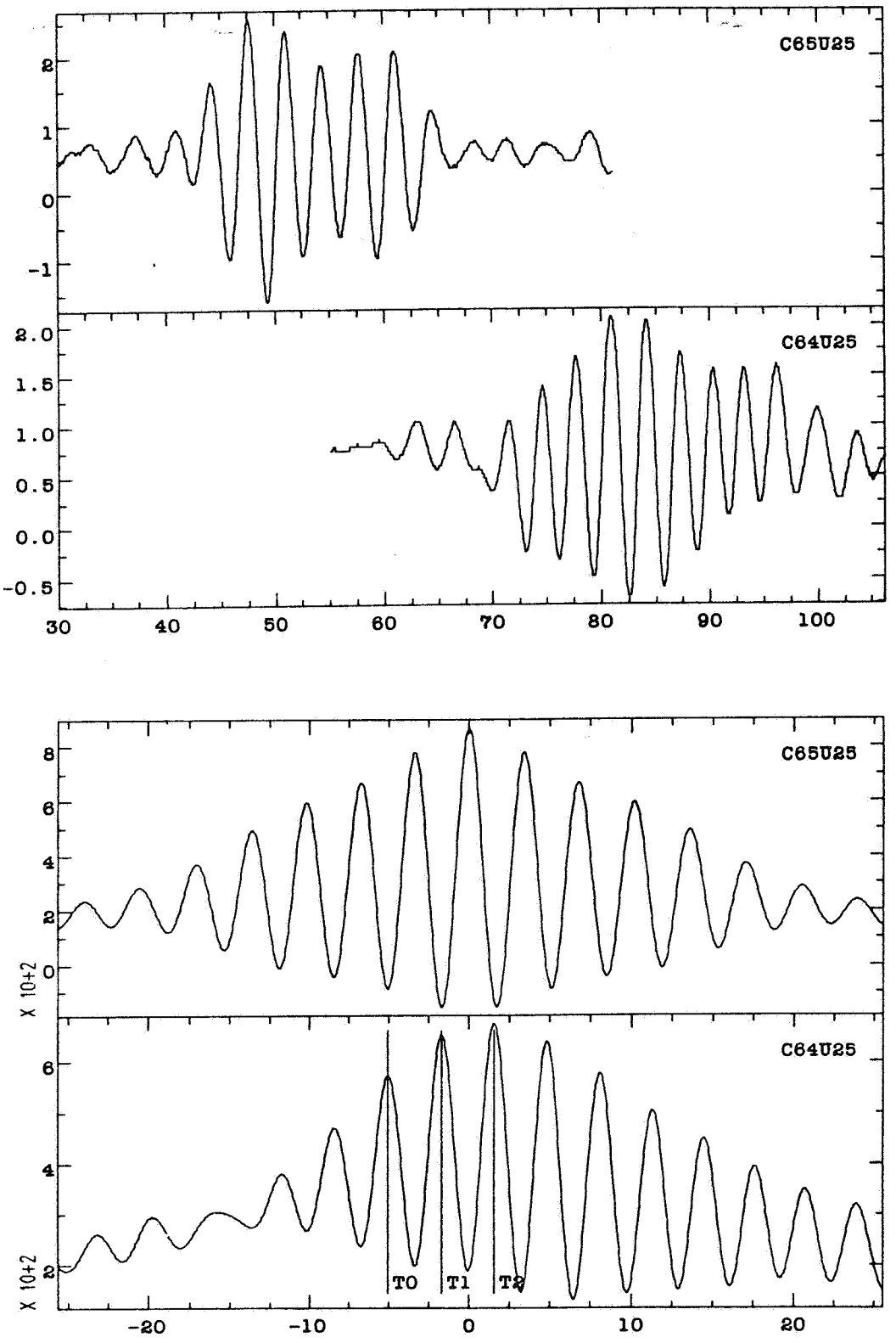

Records of CtrU25 and C64U25. Upper plot shows the raw waveforms. Lower plot shows the cross-correlation results.

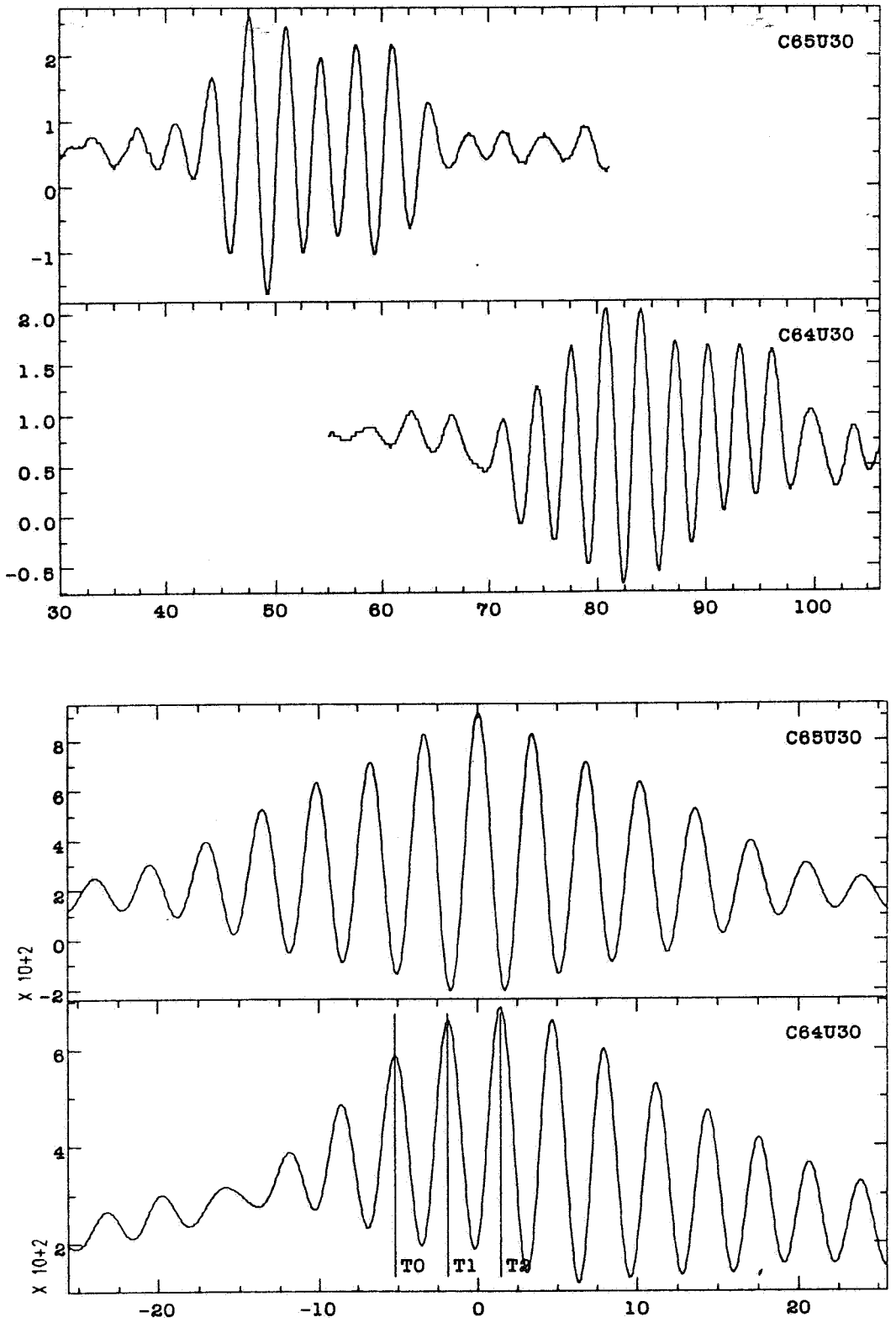

Records of C65U30 and C64U30. Upper plot shows the raw waveforms. Lower plot shows the cross-correlation results.

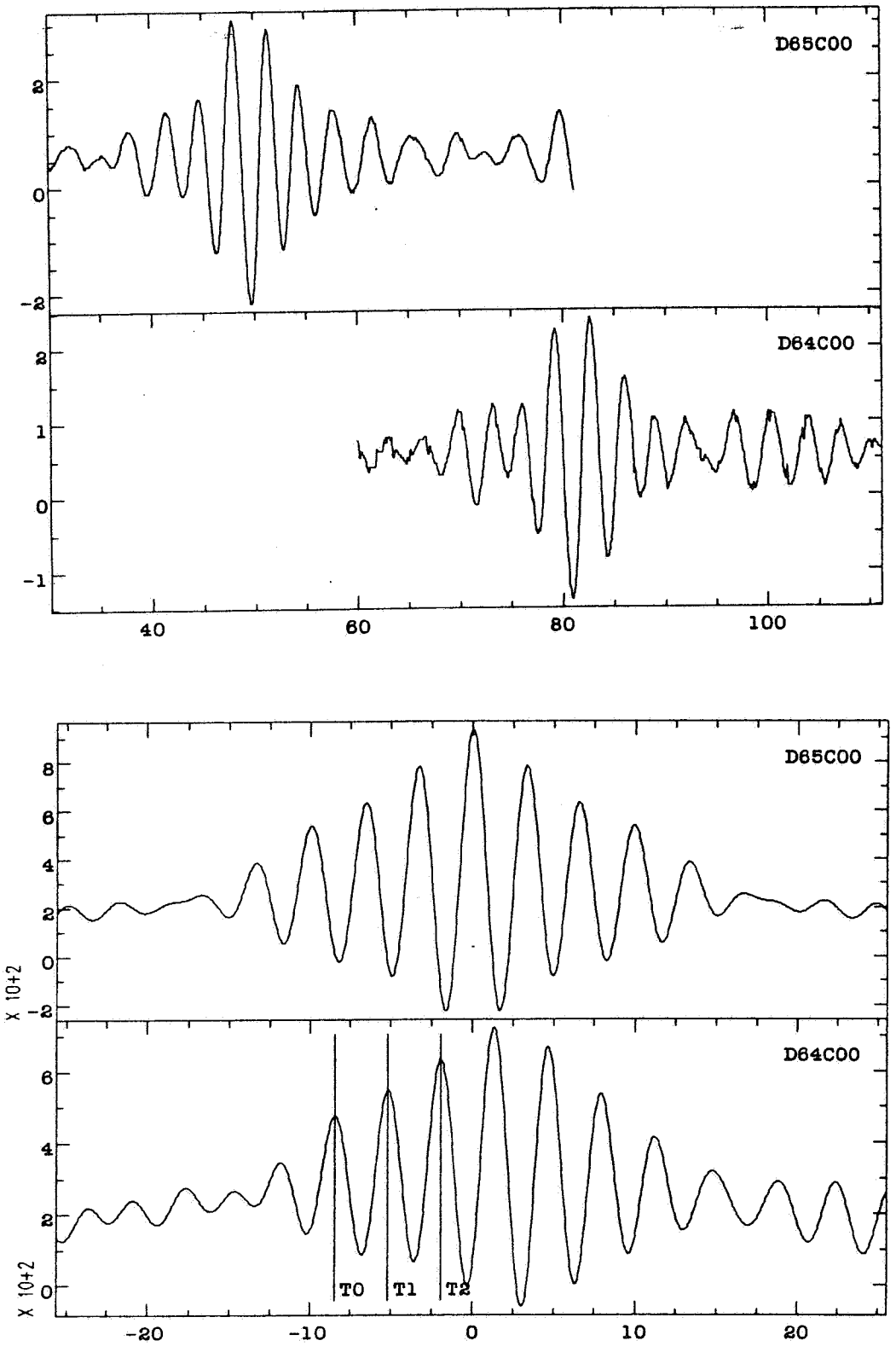

Records of D65C00 and D64C00. Upper plot shows the raw waveforms. Lower plot shows the cross-correlation results.

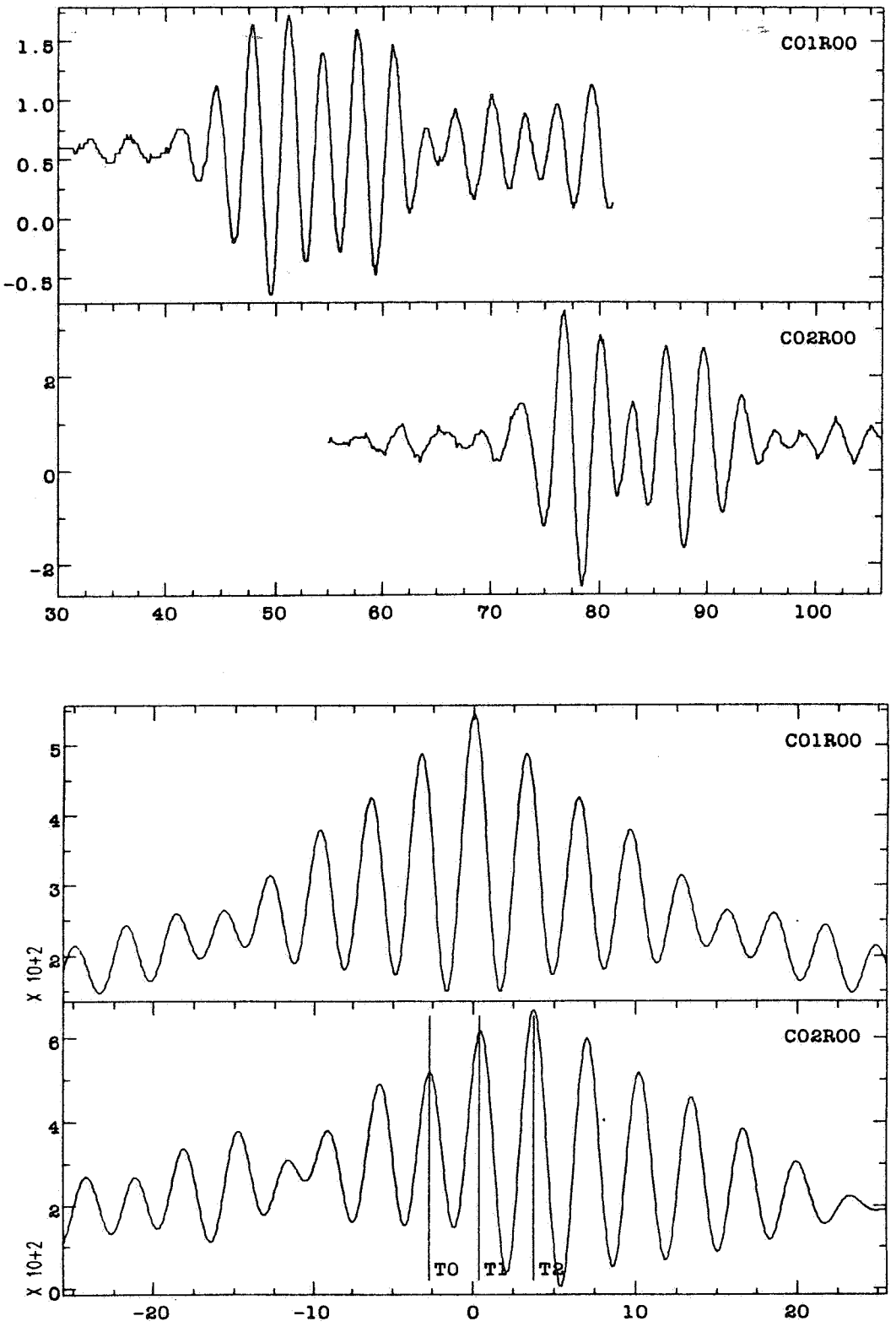

Records of C01R00 and C02R00. Upper plot shows the raw waveforms. Lower plot shows the cross-correlation results.

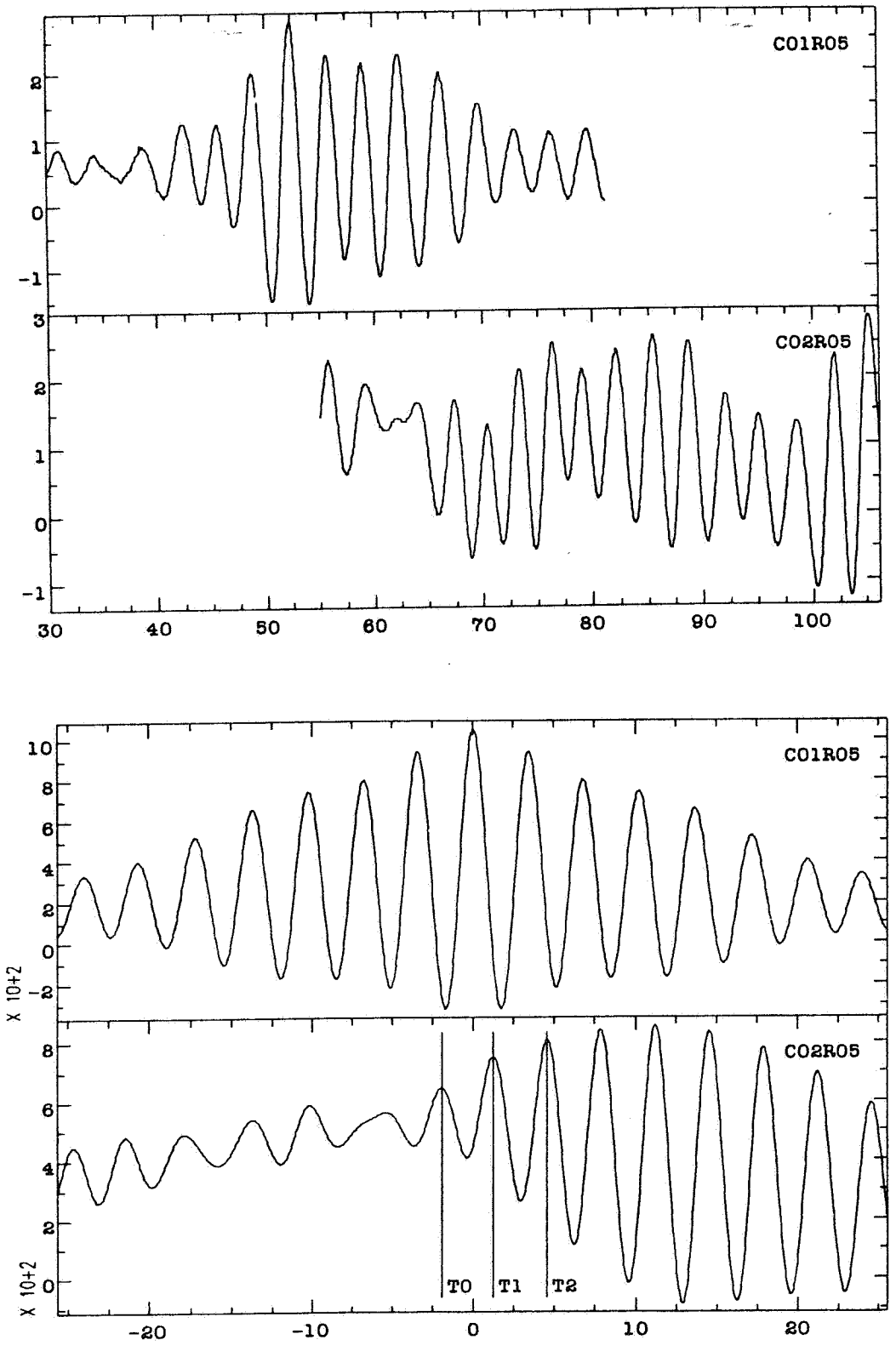

Records of C01R05 and C02R05. Upper plot shows the raw waveforms. Lower plot shows the cross-correlation results.

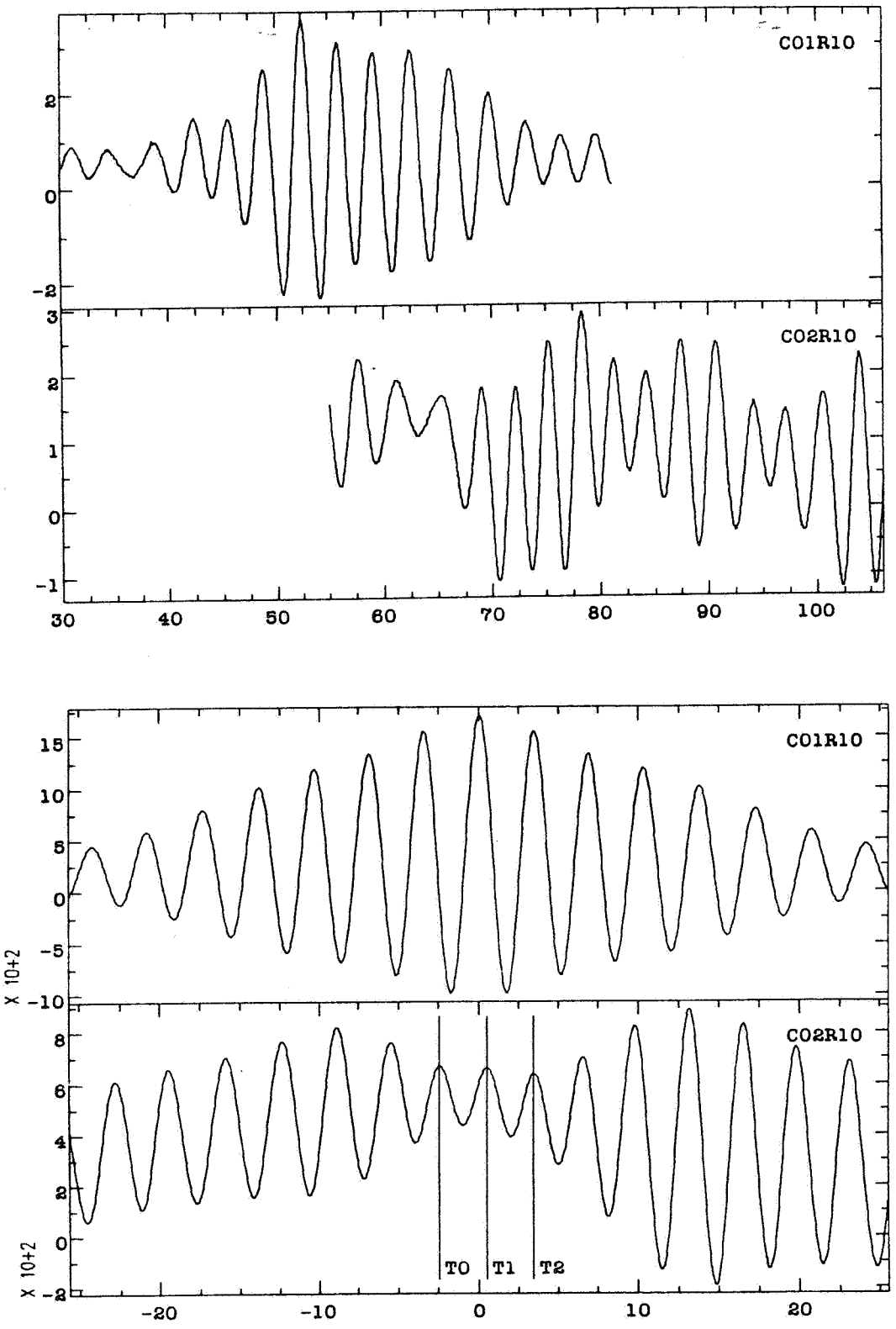

Records of C01R10 and C02R10. Upper plot shows the raw waveforms. Lower plot shows the cross-correlation results.

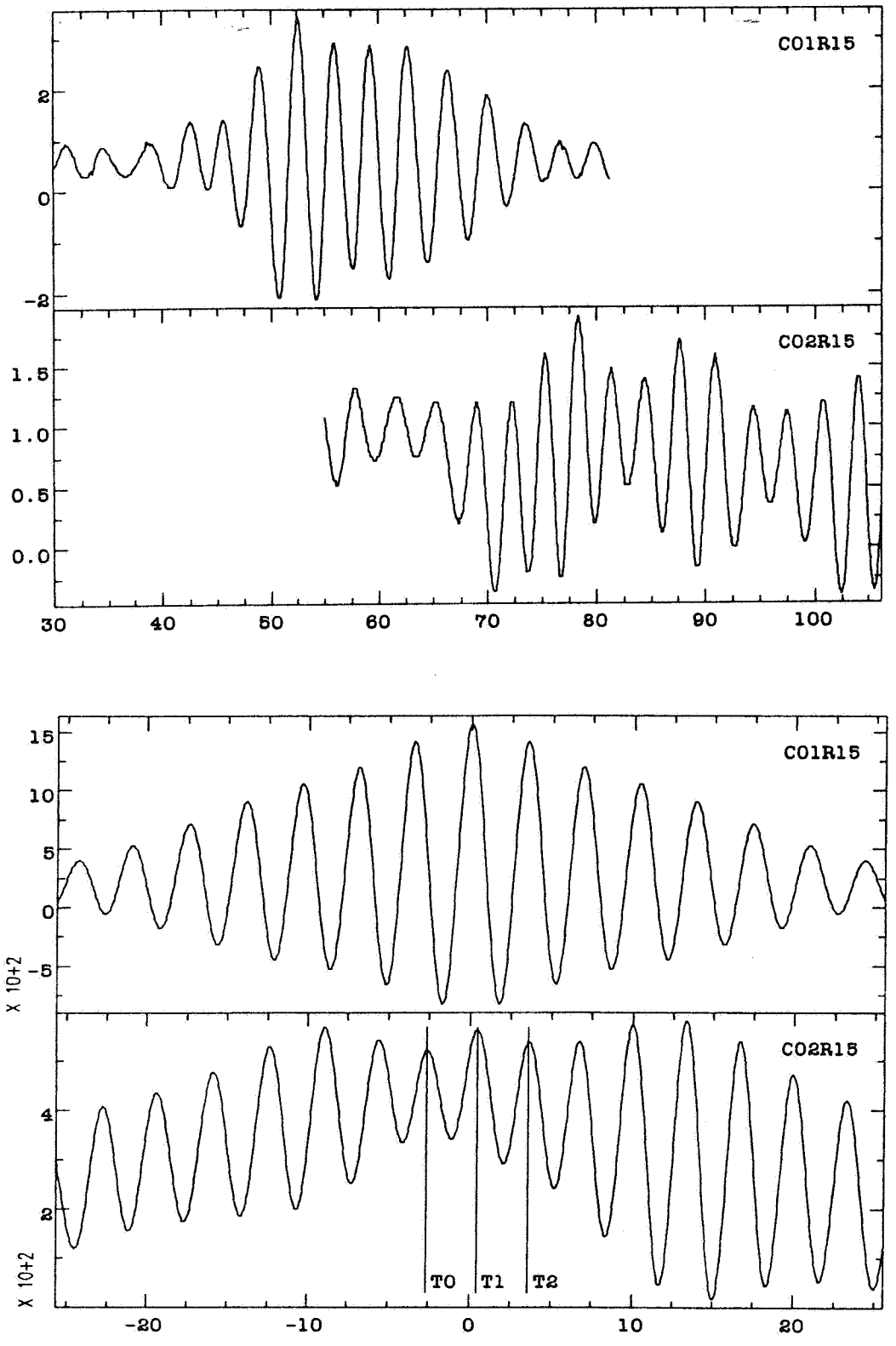

Records of C01R15 and C02R15. Upper plot shows the raw waveforms. Lower plot shows the cross-correlation results.

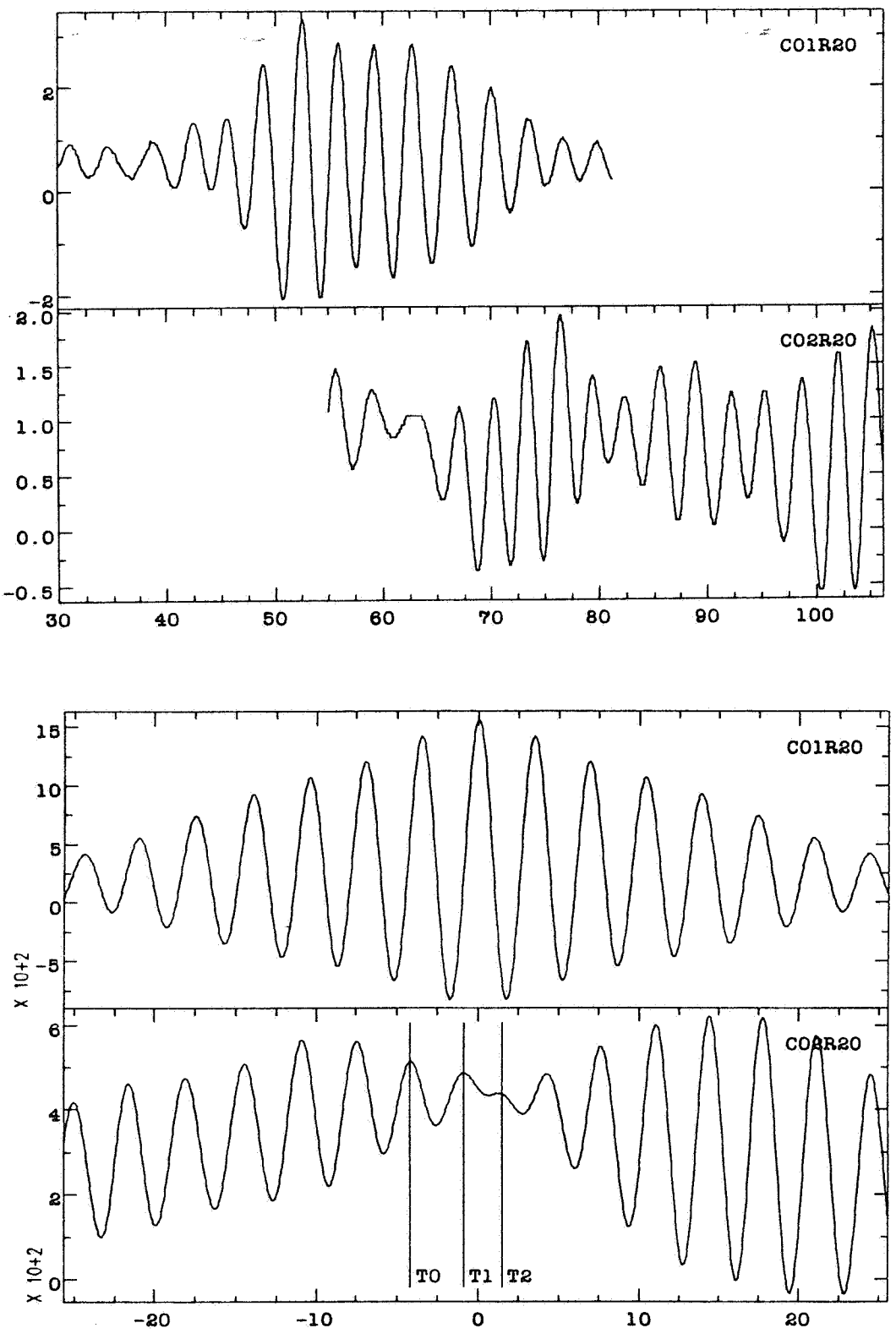

Records of C01R20 and C02R20. Upper plot shows the raw waveforms. Lower plot shows the cross-correlation results.

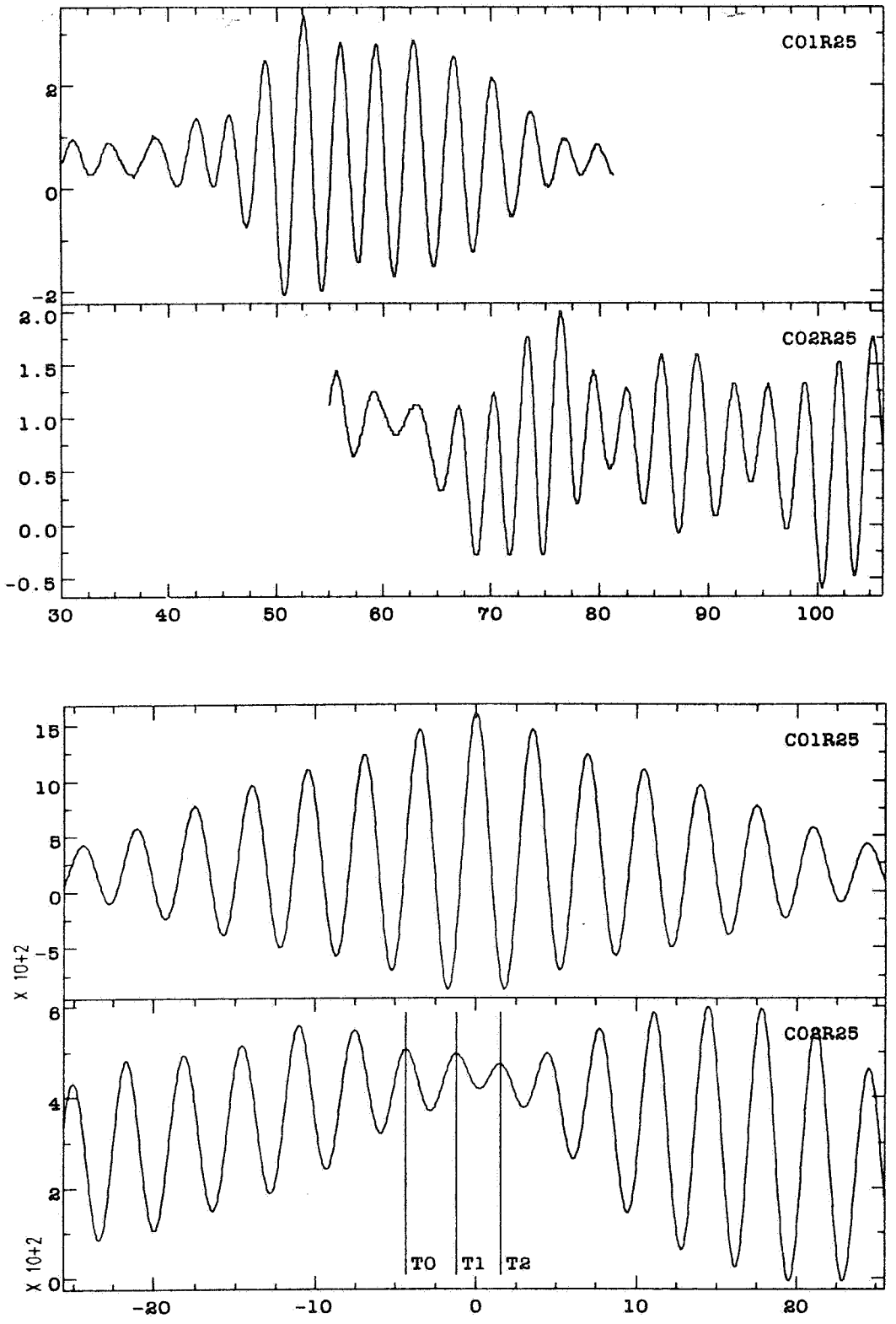

Records of C01R25 and C02R25. Upper plot shows the raw waveforms. Lower plot shows the cross-correlation results.

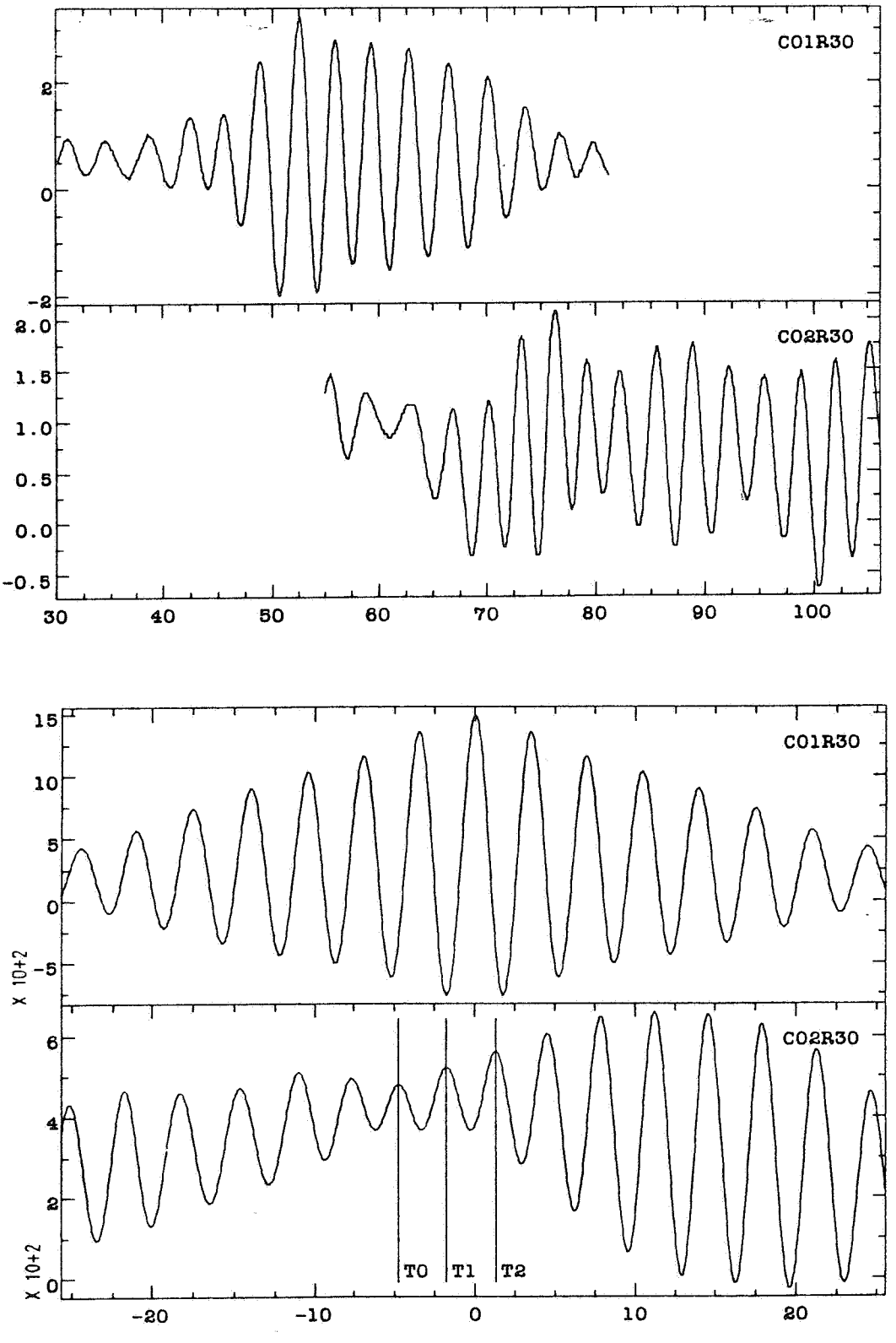

Records of C01R30 and C02R30. Upper plot shows the raw waveforms. Lower plot shows the cross-correlation results.

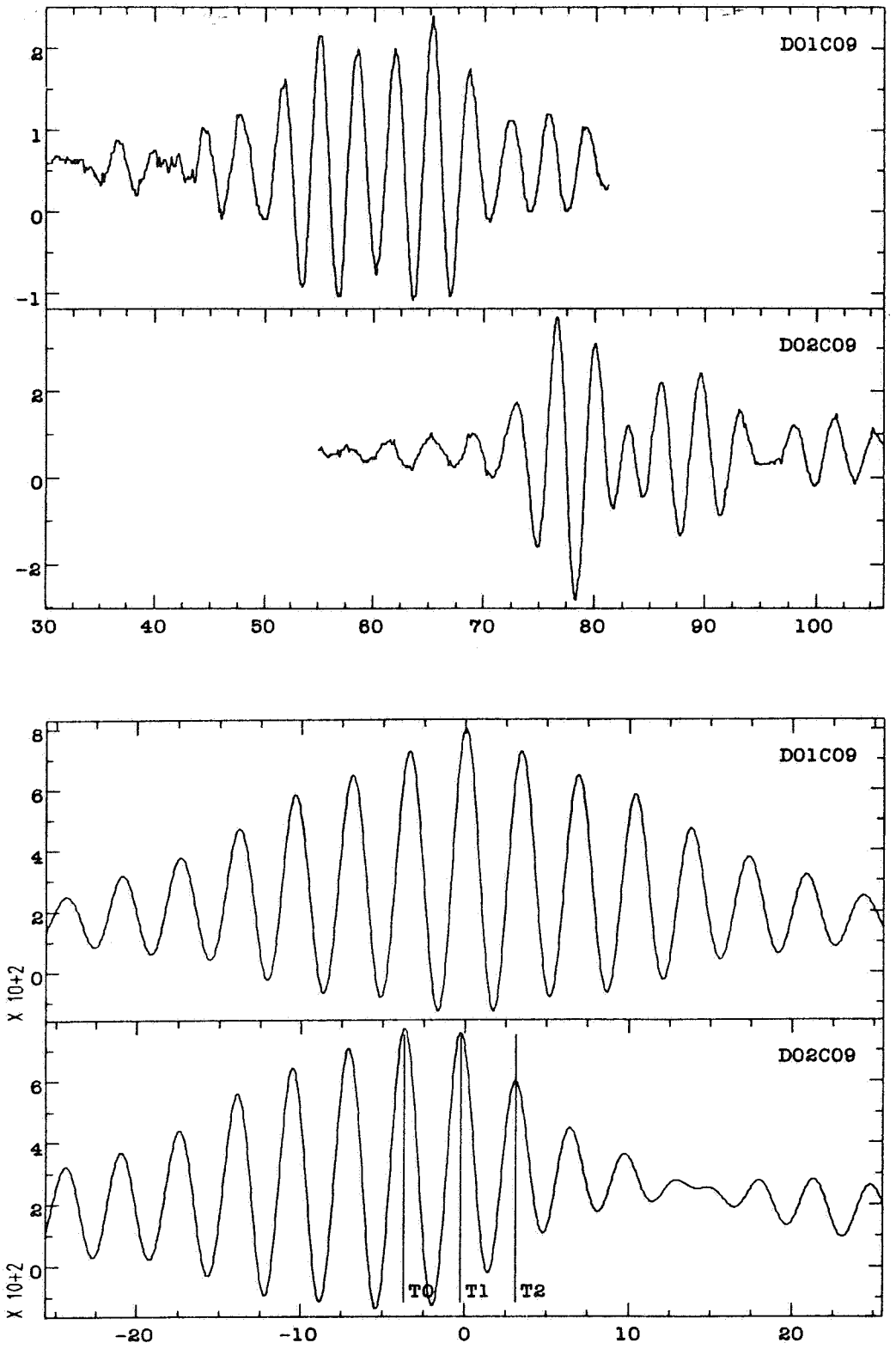

Records of D01C09 and D02C09. Upper plot shows the raw waveforms. Lower plot shows the cross-correlation results.

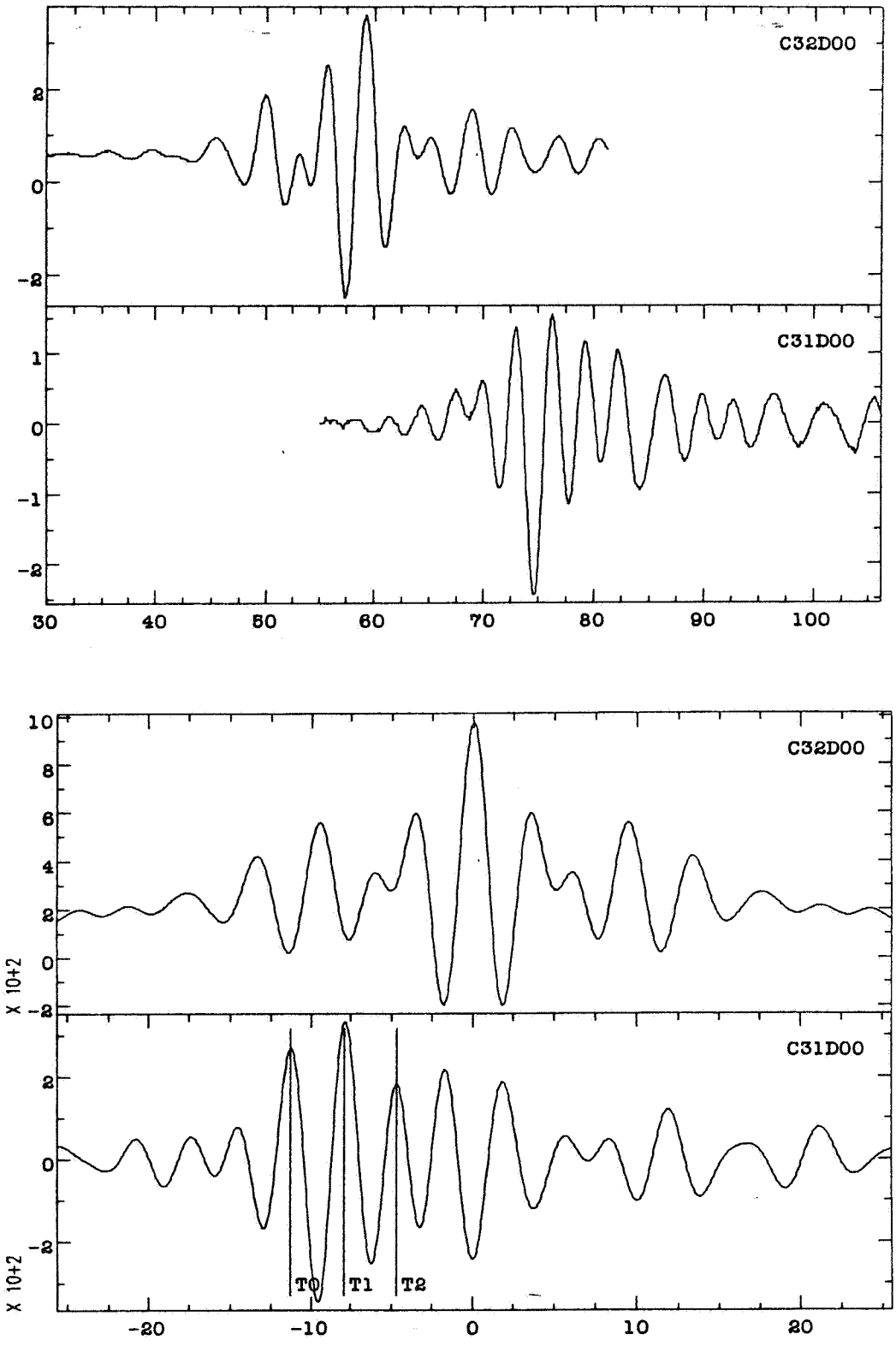

Records of C32D00 and C31D00. Upper plot shows the raw waveforms. Lower plot shows the cross-correlation results.

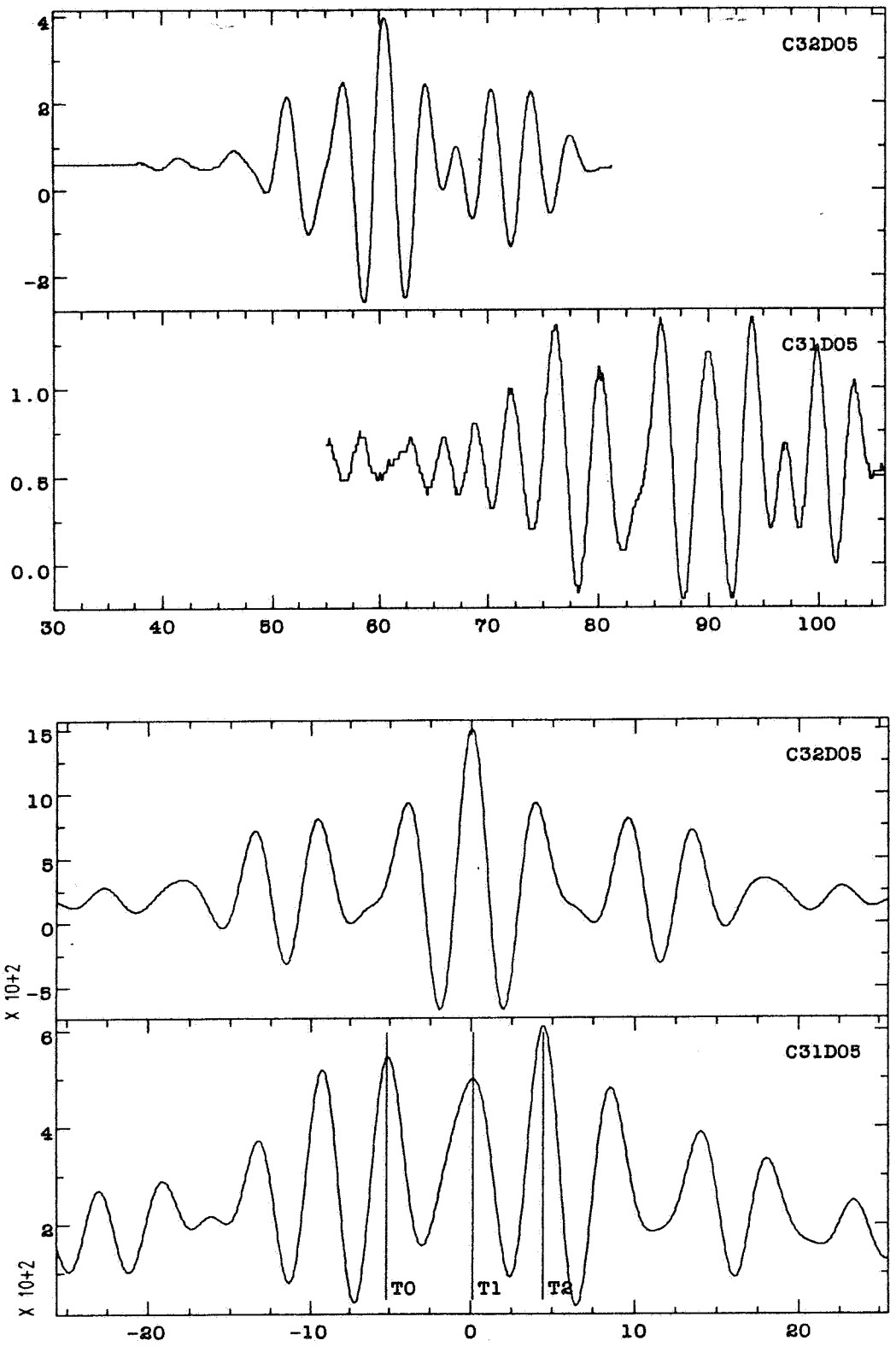

Records of C32D05 and C31D05. Upper plot shows the raw waveforms. Lower plot shows the cross-correlation results.

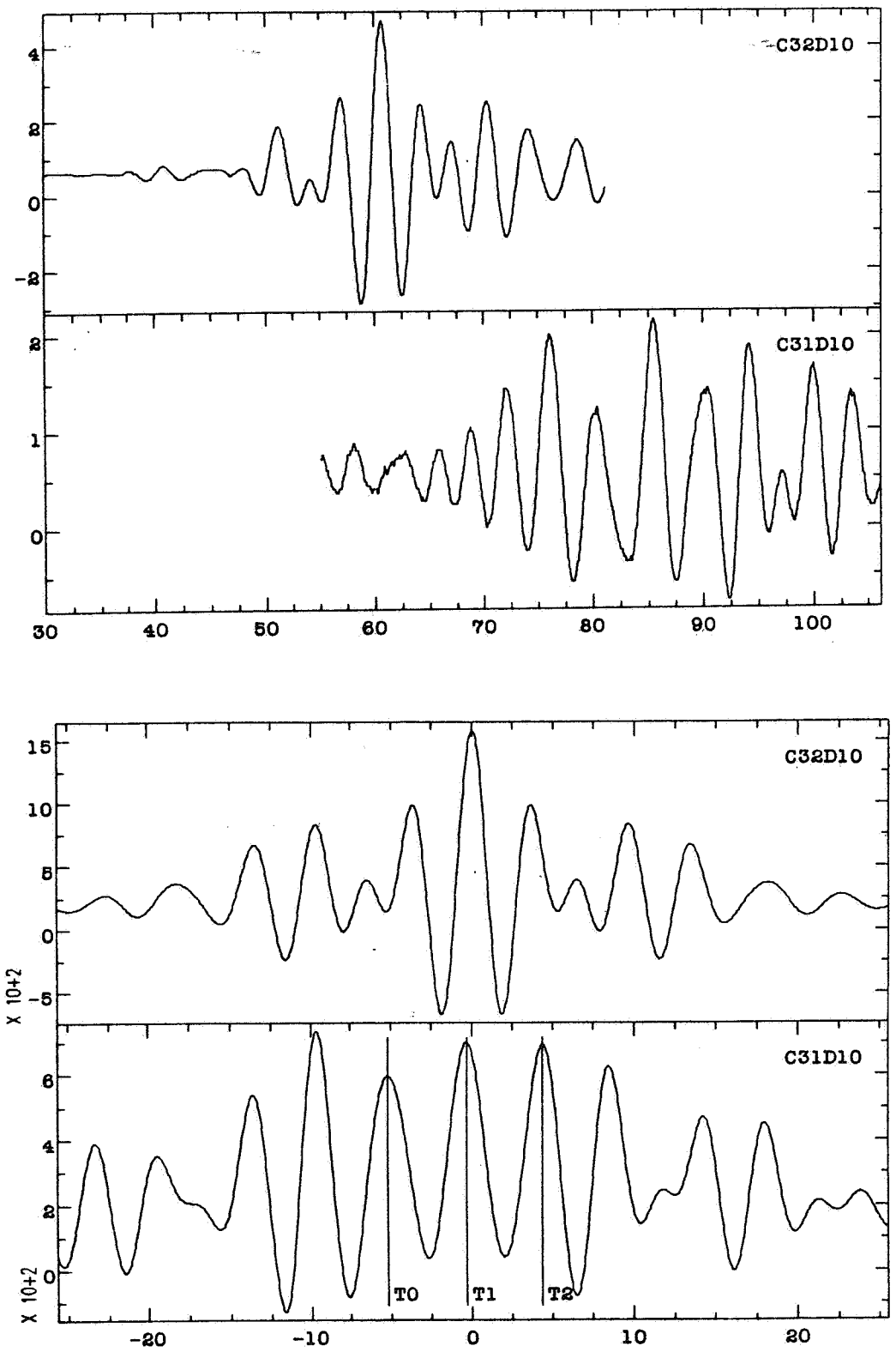

Records of C32D10 and C31D10. Upper plot shows the raw waveforms. Lower plot shows the cross-correlation results.

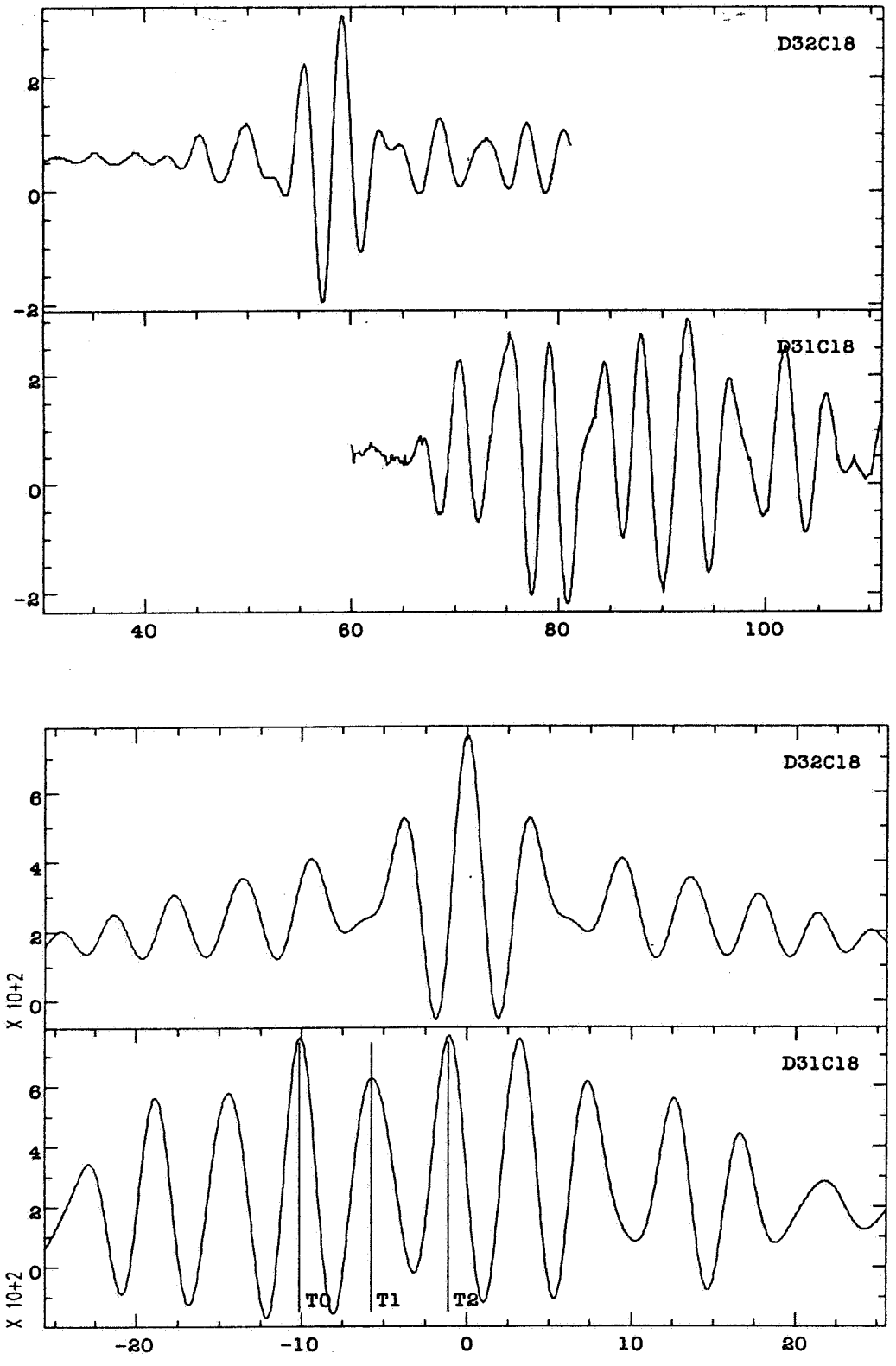

Records of D32C18 and D31C18. Upper plot shows the raw waveforms. Lower plot shows the cross-correlation results.

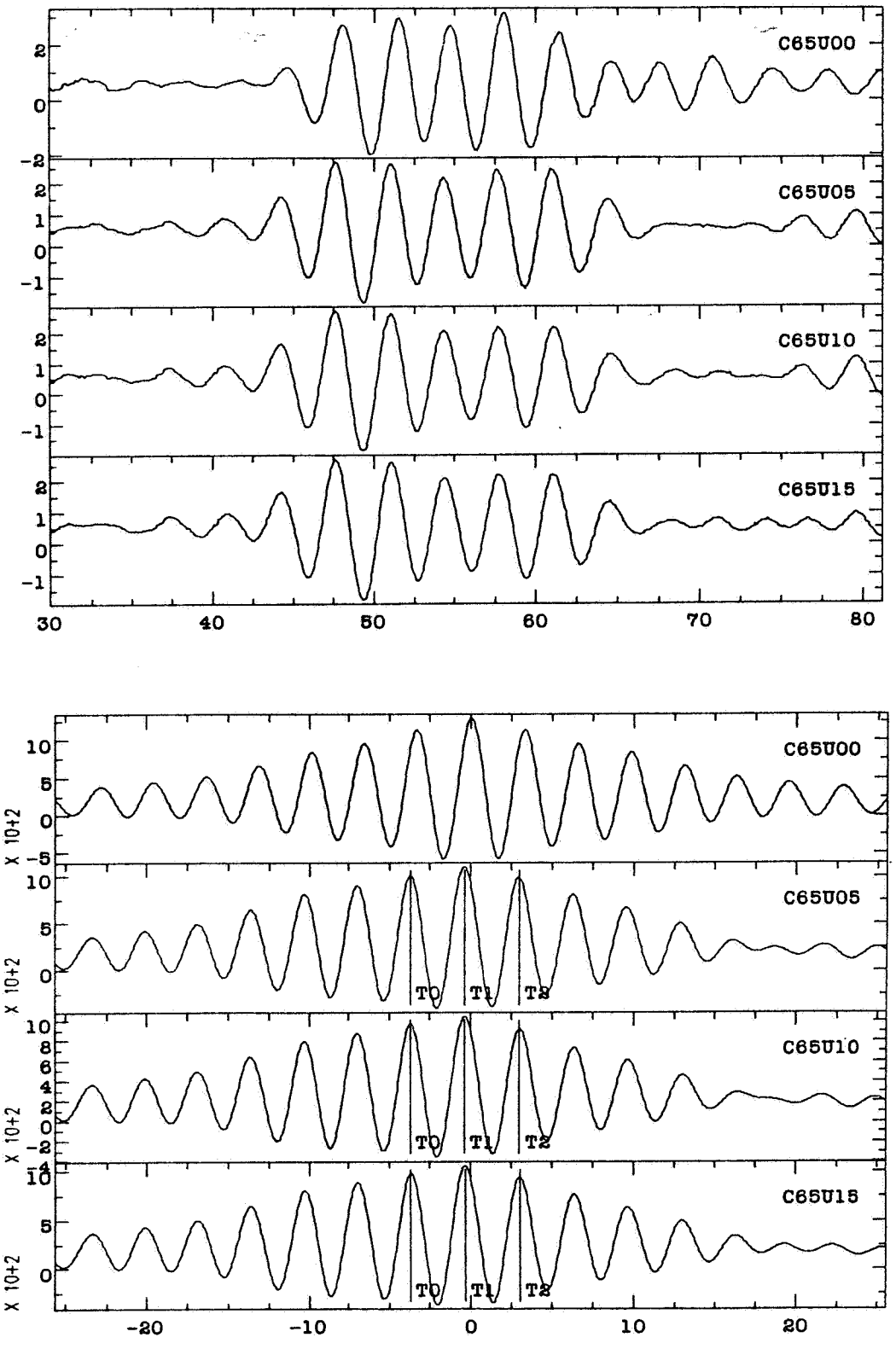

Records of C65U00, C65U05, C65U10 and C65U15. Upper plot shows the raw waveforms. Lower plot shows the cross-correlation results.

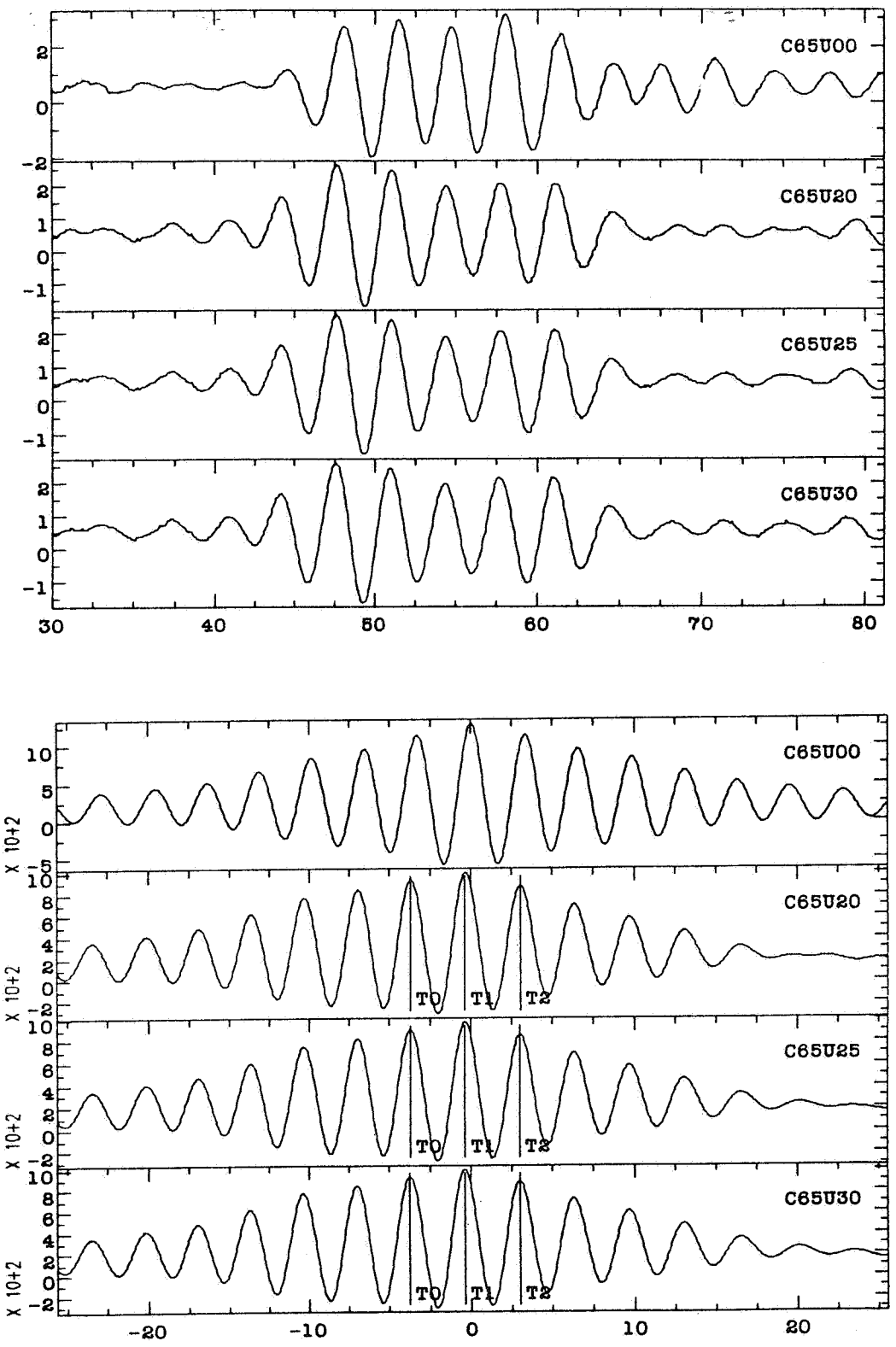

Records of C54U00, C65U20, C65U25 and C65U30. Upper plot shows the raw waveforms. Lower plot shows the cross-correlation results.

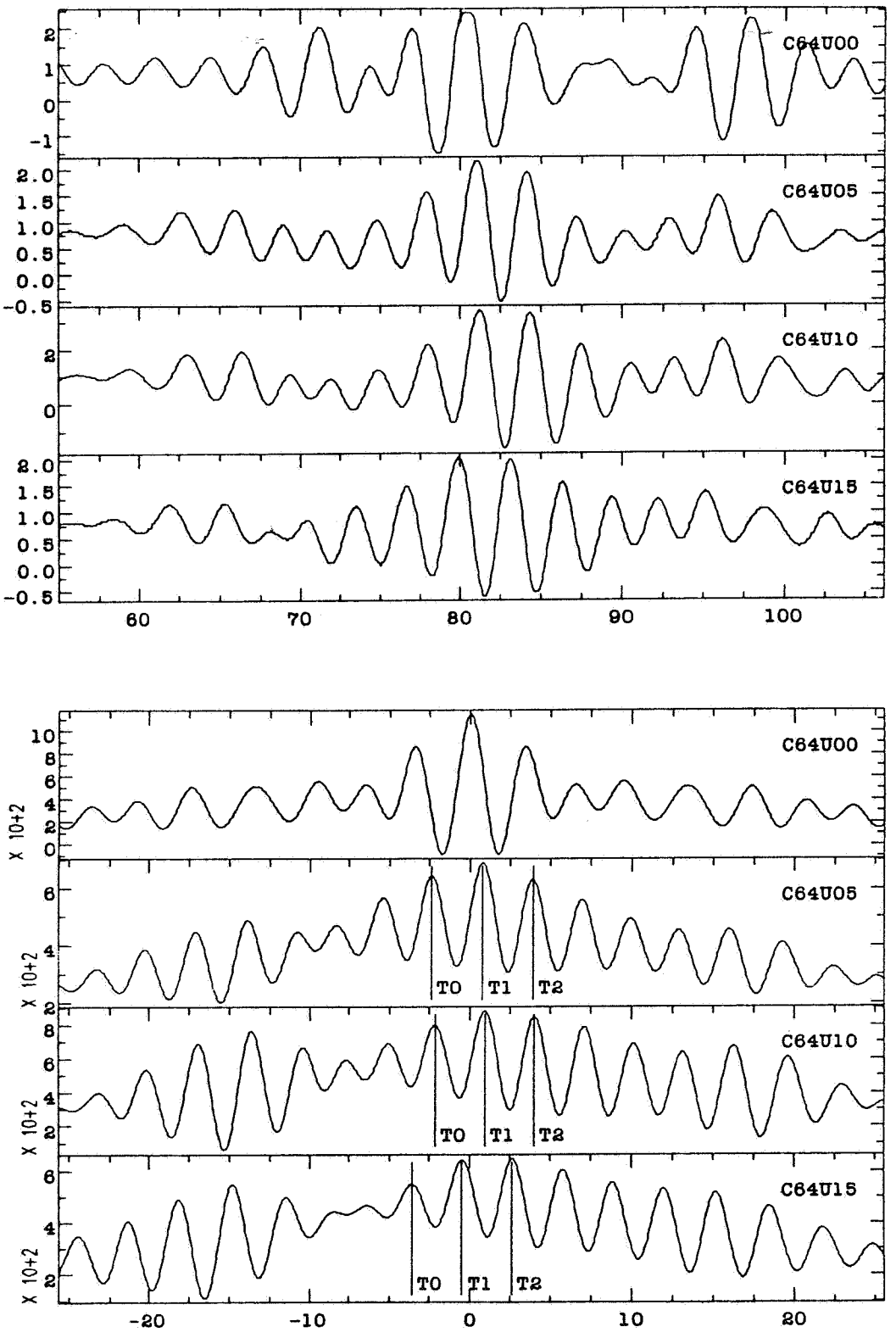

Records of C64U00, C64U05, C64U10, and C64U15. Upper plot shows the raw waveforms. Lower plot shows the cross-correlation results.

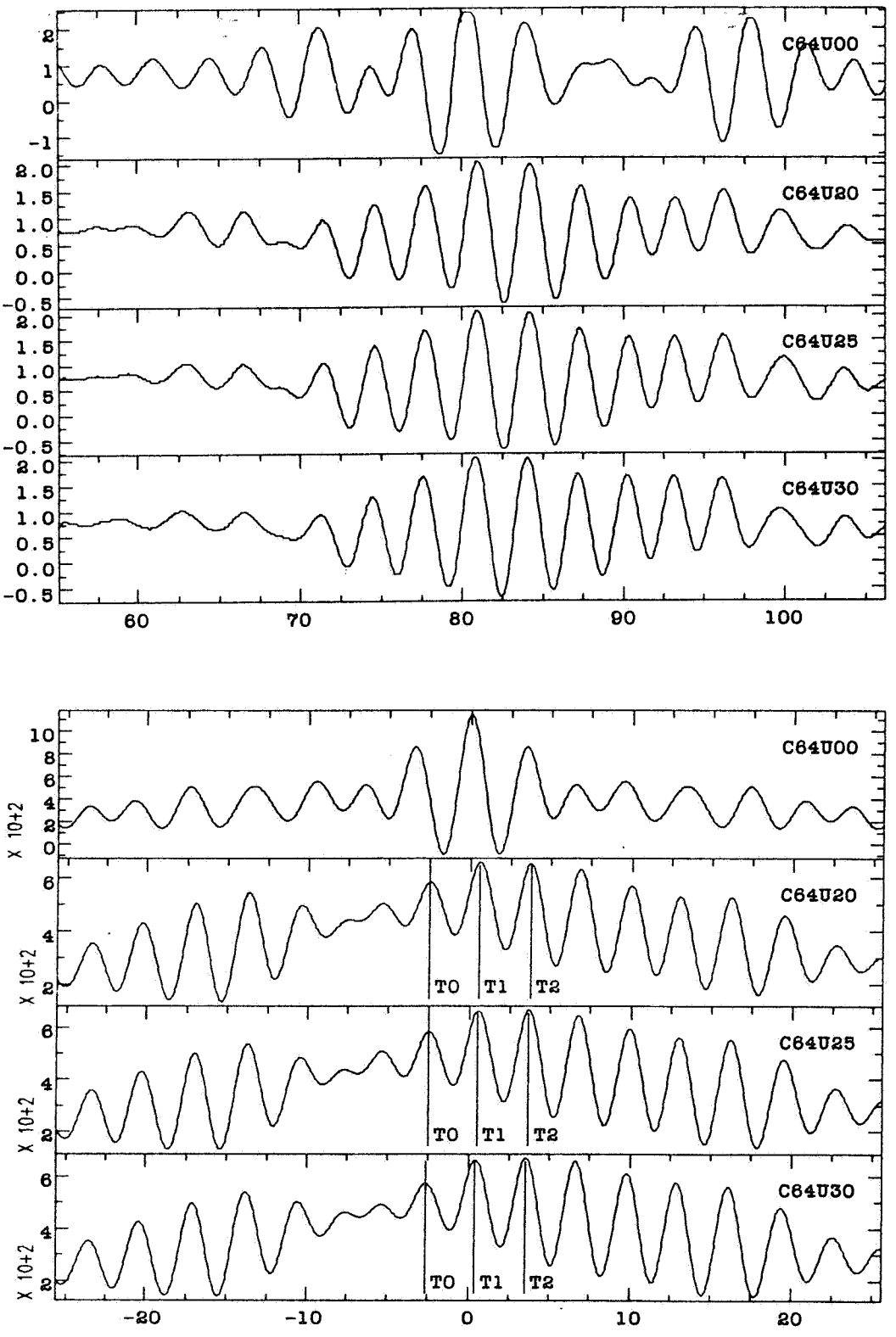

Records of C64U00, C64U20, C64U25 and C64U30. Upper plot shows the raw waveforms. Lower plot shows the cross-correlation results.

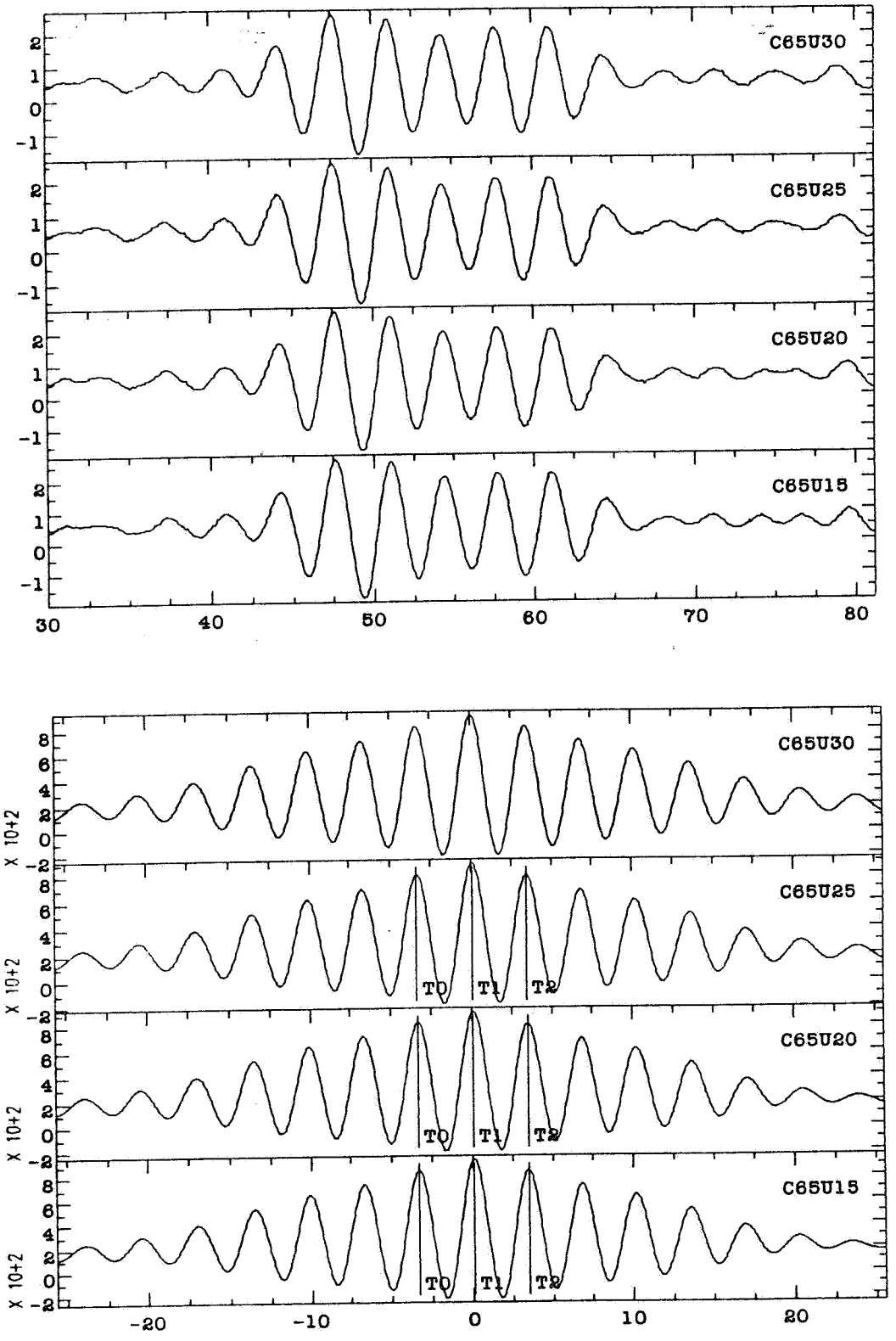

Records of C54U30, C65U25, C65U20, and C65U15. Upper plot shows the raw waveforms. Lower plot shows the cross-correlation results.

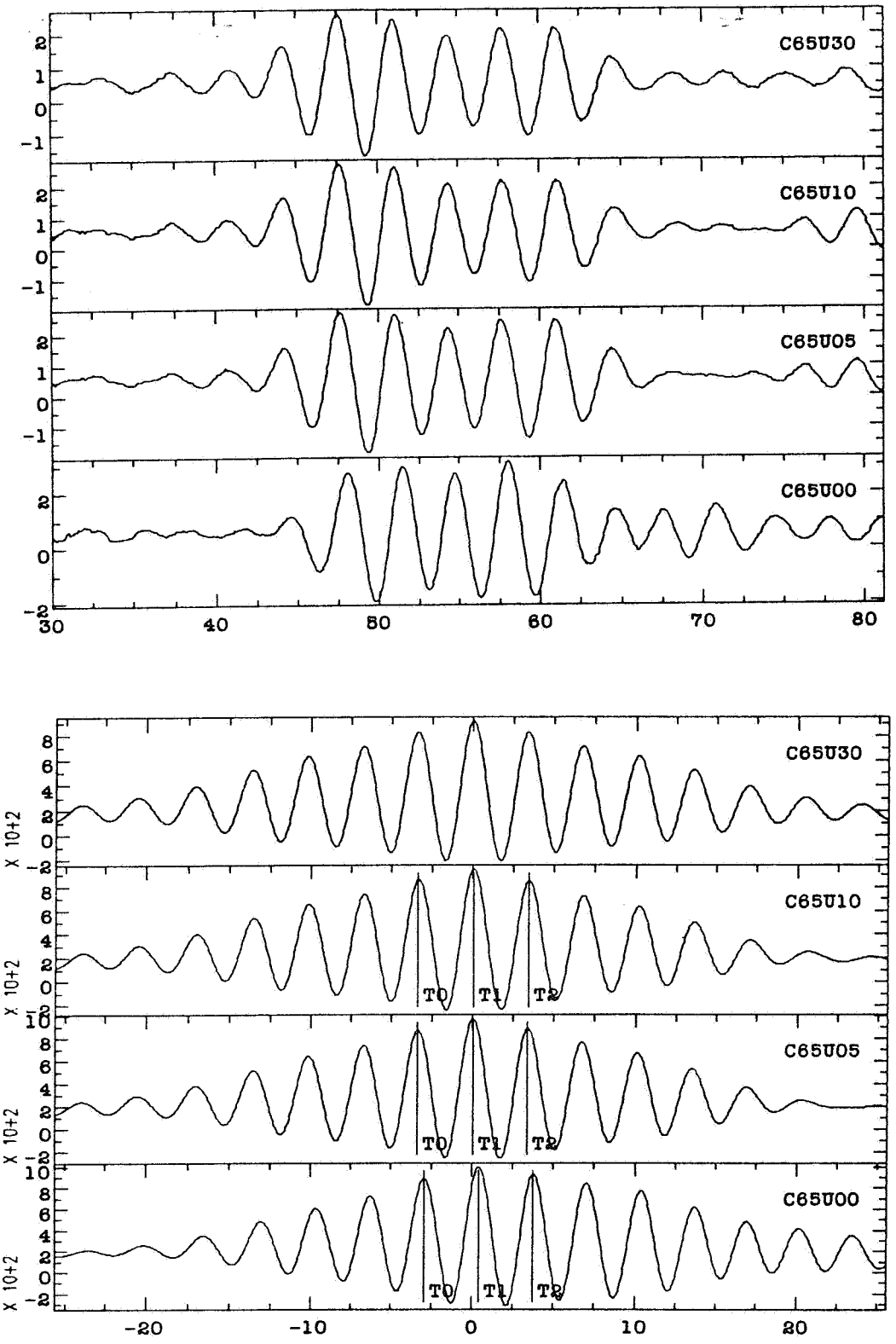

Records of C65U30, C65U10, C65U05 and C65U00. Upper plot shows the raw waveforms. Lower plot shows the cross-correlation results.

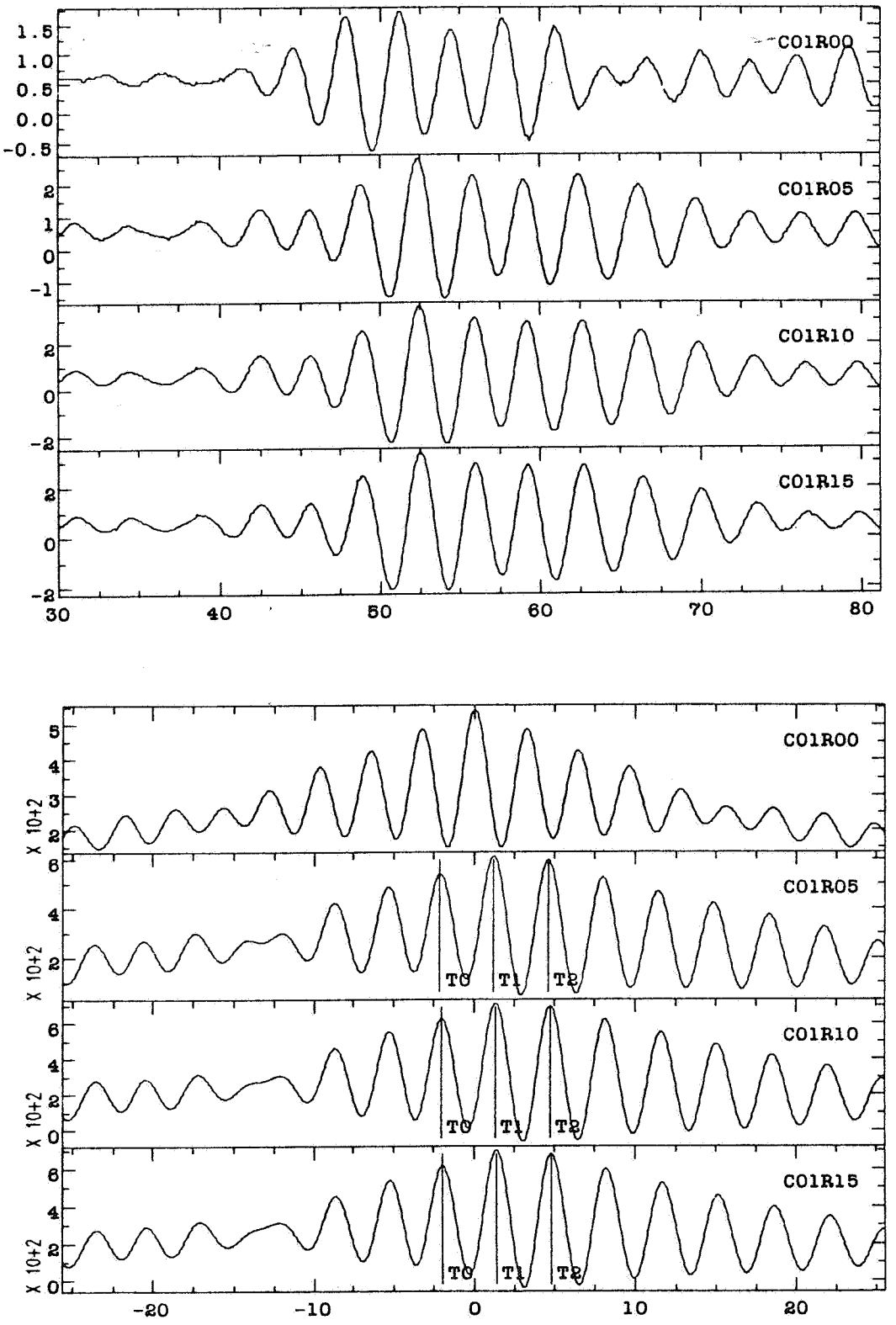

Records of C01R00, C01R05, C01R10 and C01R15. Upper plot shows the raw waveforms. Lower plot shows the cross-correlation results.

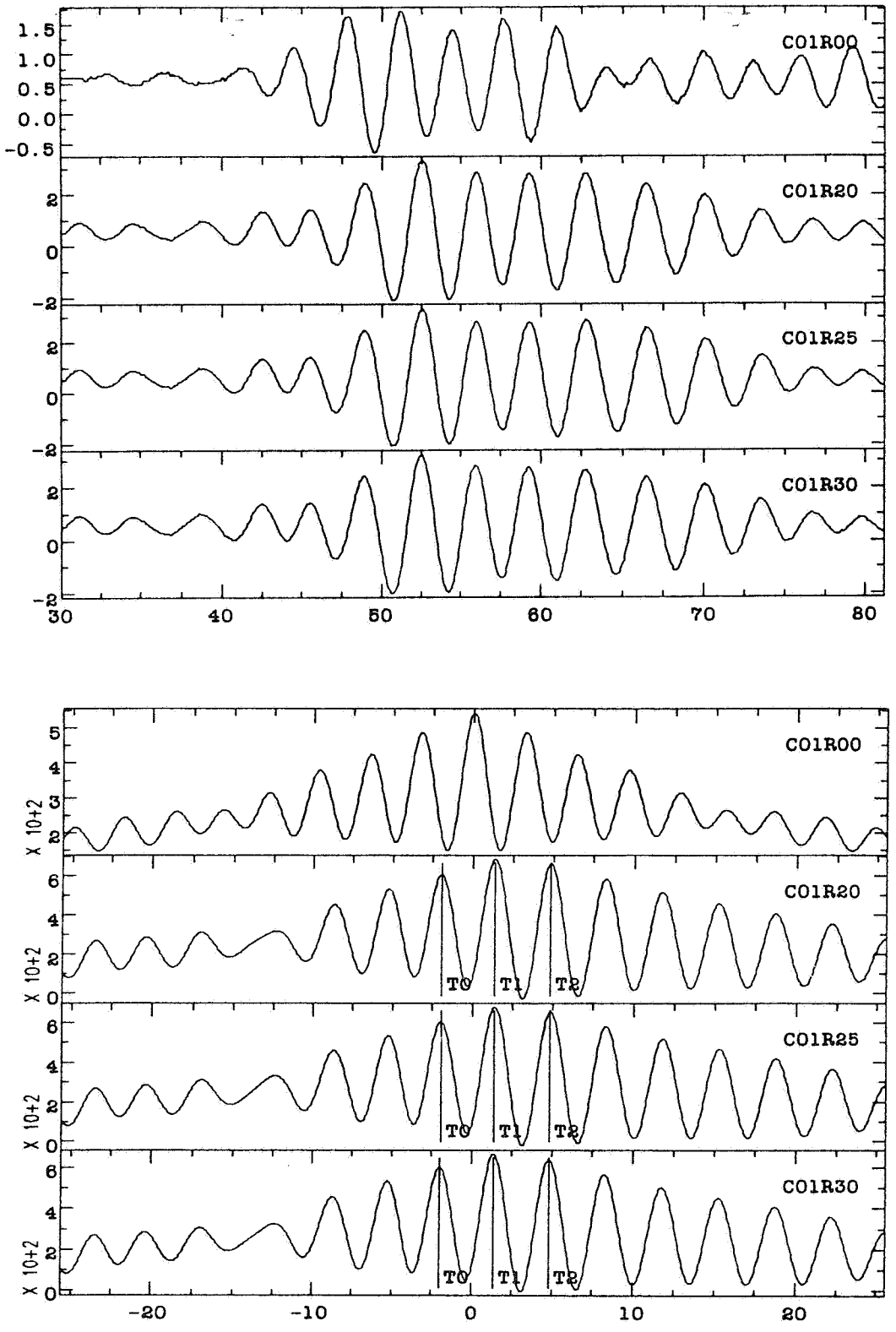

Records of C01R00, C01R20, C01R25 and C01R30. Upper plot shows the raw waveforms. Lower plot shows the cross-correlation results.

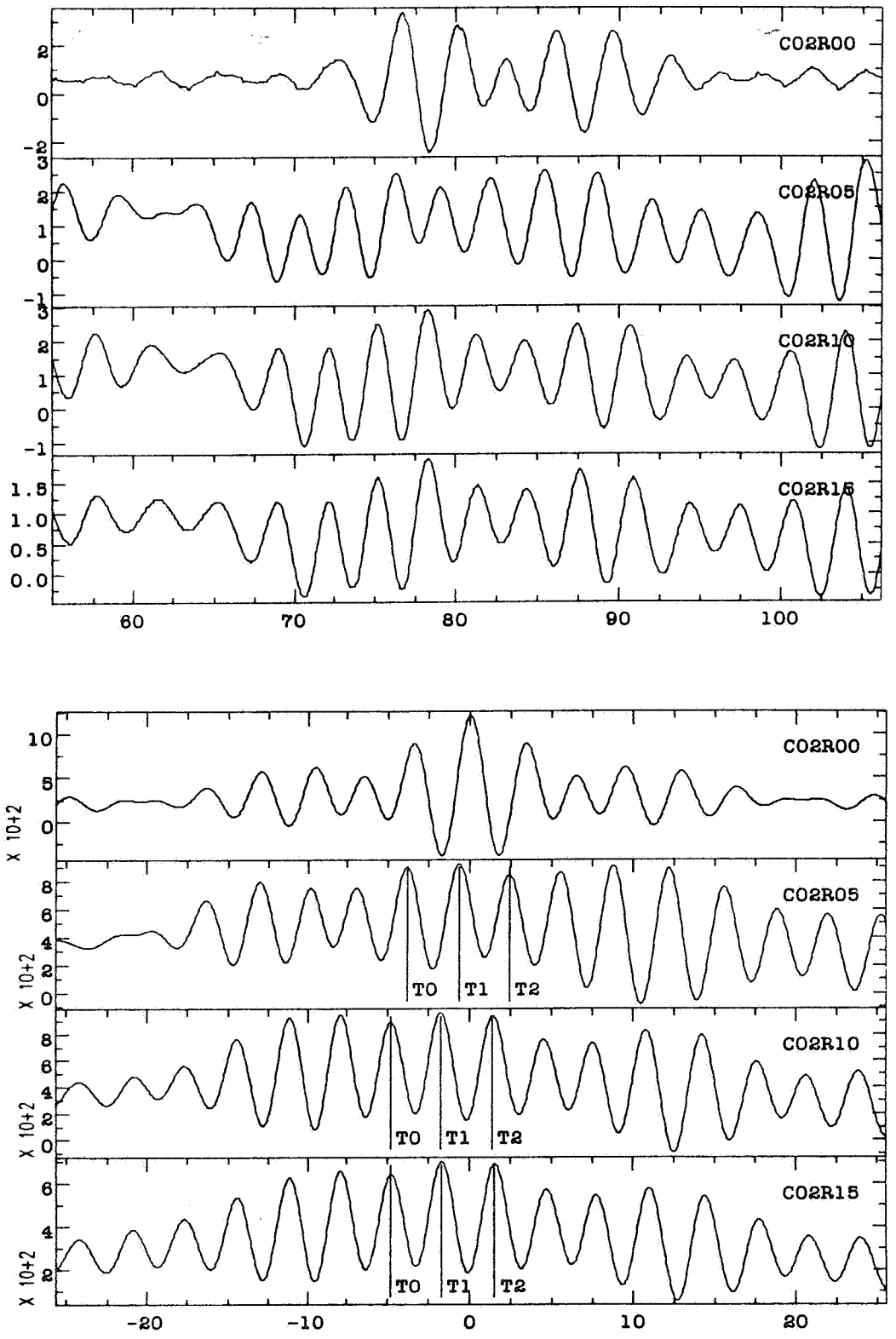

Records of C02R00, C02R05, C02R10 and C02R15. Upper plot shows the raw waveforms. Lower plot shows the cross-correlation results.

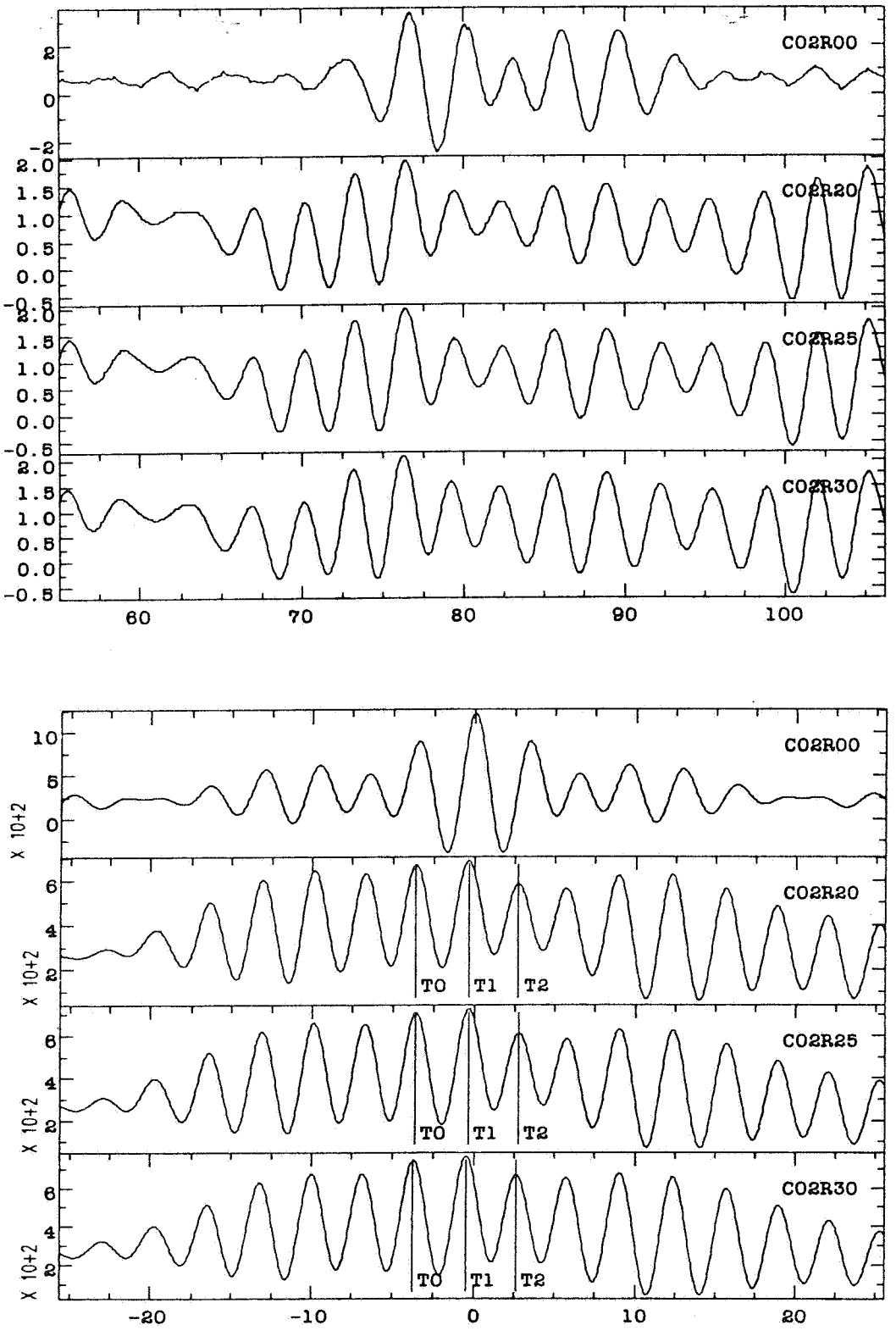

Records of C02R00, C02R20, C02R25 and C02R30. Upper plot shows the raw waveforms. Lower plot shows the cross-correlation results.

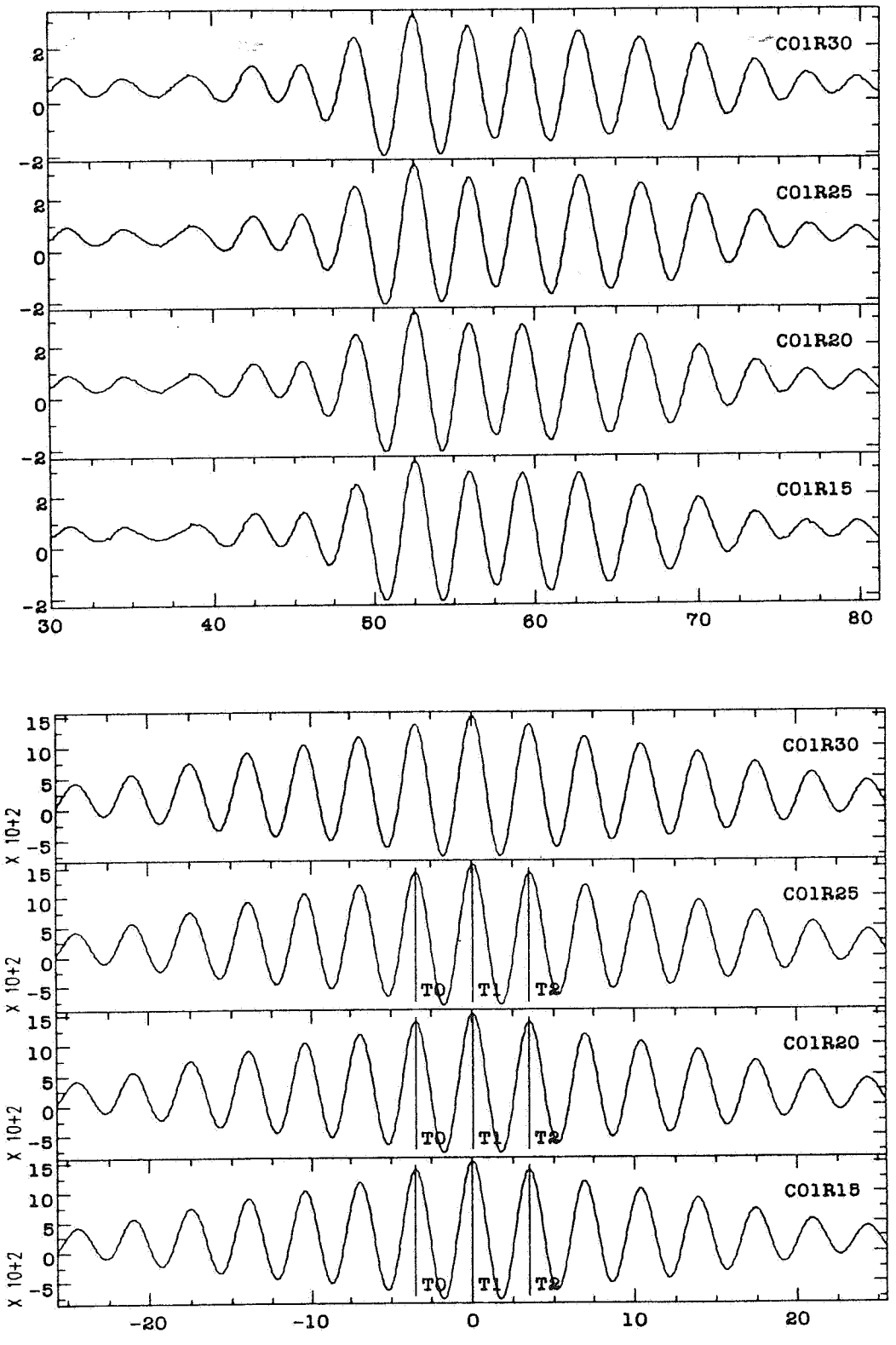

Records of C01R30, C01R25, C01R20 and C01R15. Upper plot shows the raw waveforms. Lower plot shows the cross-correlation results.

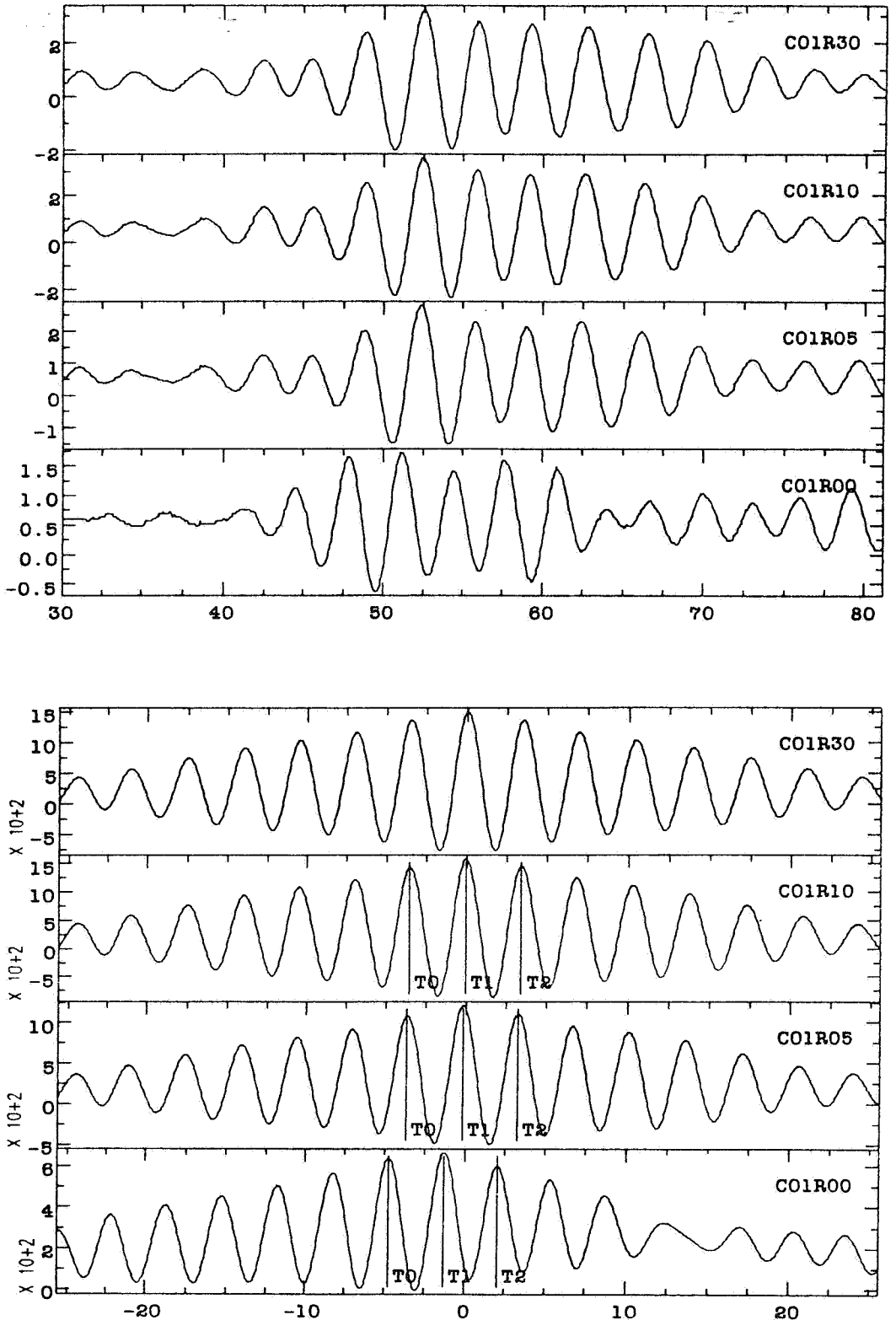

Records of C01R30, C01R10, C01R05, and C01R00. Upper plot shows the raw waveforms. Lower plot shows the cross-correlation results.

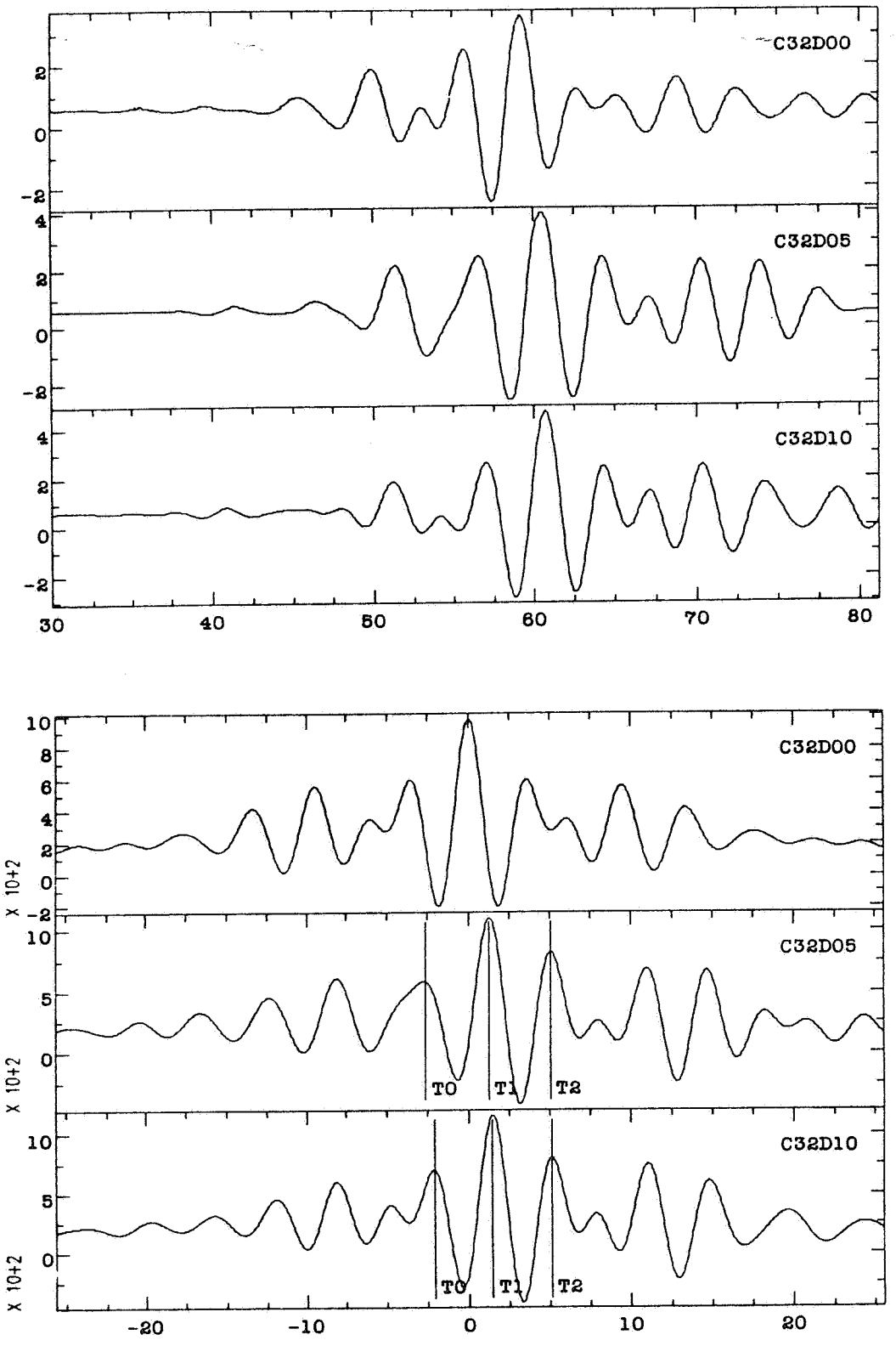

Records of C32D00, C32D05, and C32D10. Upper plot shows the raw waveforms. Lower plot shows the cross-correlation results.

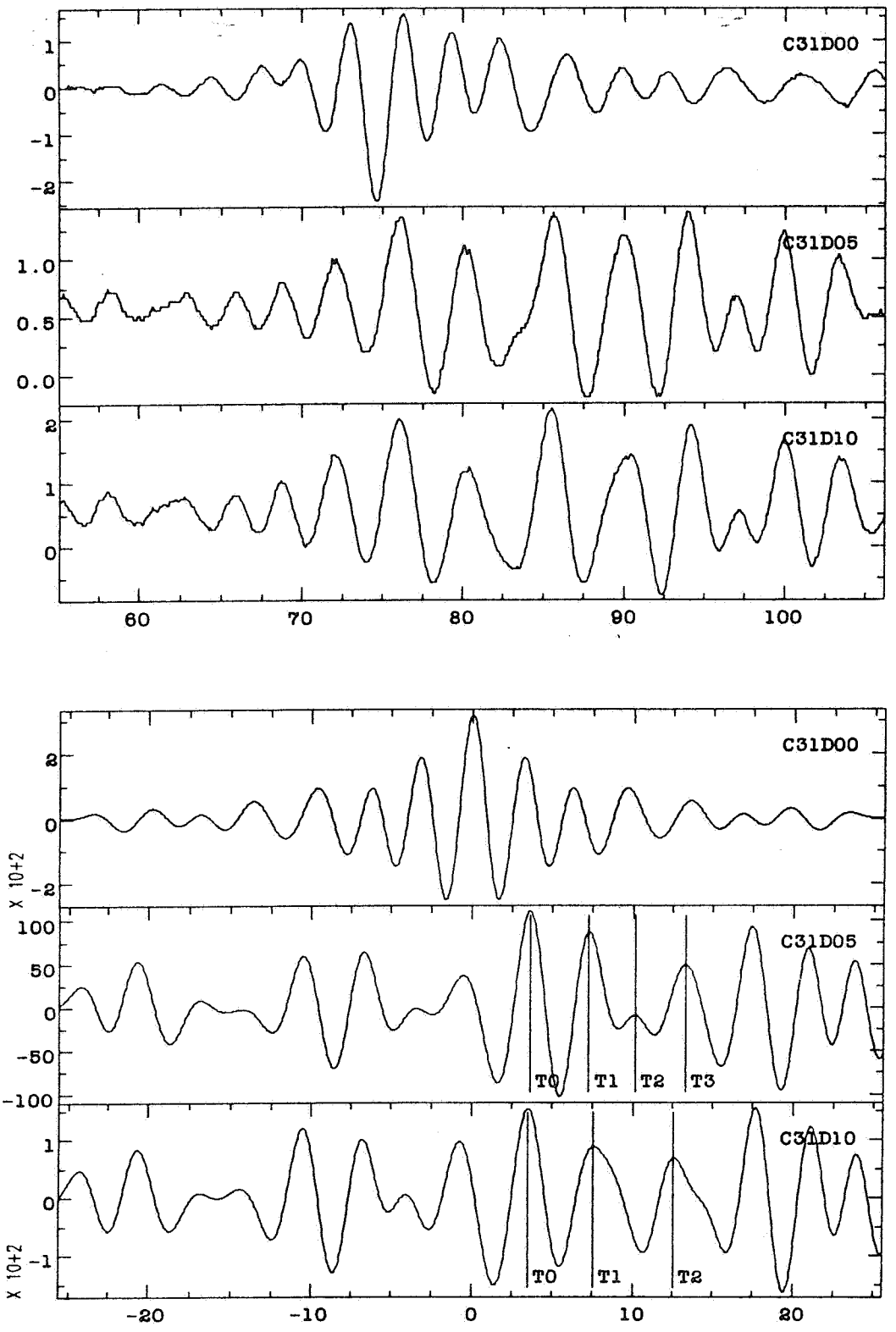

Records of C31D00, C31D05 and C31D10. Upper plot shows the raw waveforms. Lower plot shows the cross-correlation results.

10. APPENDIX B

Appendix B contains all the tables of data from the cross-correlation results.

Table 1: Timing Analysis For The Stressmeter Field Test Data
----Absolute Velocity.

Angle	File 1	File 2	Typ	Tc 1 µs	Tc 2 µs	DT µs	TPOS1 µs	TPOS2 µs	T µs	L mm	V km/s	QUA
0	C65U00	C64U00	T	0.00	1.91	-2.39	30.00	55.00	24.52	82.55	3.37	GF
"	C65U05	C64U05	T	0.00	0.00	-1.63	30.00	55.00	23.37	82.55	3.53	GF
"	C65U10	C64U10	T	0.00	0.00	-1.65	30.00	55.00	23.35	82.55	3.53	GF
"	C65U15	C64U15	T	0.00	0.00	-2.90	30.00	55.00	22.10	82.55	3.74	GF
"	C65U20	C64U20	T	0.00	0.00	-1.79	30.00	55.00	23.21	82.55	3.56	GG
"	C65U25	C64U25	T	0.00	0.00	-1.77	30.00	55.00	23.23	82.55	3.55	GF
"	C65U30	C64U30	T	0.00	0.00	-1.90	30.00	55.00	23.10	82.55	3.57	GF
"	D65C00	D64C00	T	0.00	0.00	-5.23	30.00	60.00	24.77	82.55	3.33	GG
90	C01R00	C02R00	T	0.00	0.00	0.47	30.00	55.00	25.47	82.55	3.24	GF
"	C01R05	C02R05	T	0.00	0.00	1.25	30.00	55.00	26.25	82.55	3.15	GP
"	C01R10	C02R10	T	0.00	0.00	0.49	30.00	55.00	25.49	82.55	3.24	GP
"	C01R15	C02R15	T	0.00	0.00	0.46	30.00	55.00	25.46	82.55	3.24	GP
"	C01R20	C02R20	T	0.00	0.00	-1.20	30.00	55.00	23.80	82.55	3.47	GP
"	C01R25	C02R25	T	0.00	0.00	-1.35	30.00	55.00	23.65	82.55	3.49	GP
"	C01R30	C02R30	T	0.00	0.00	-1.75	30.00	55.00	23.25	82.55	3.55	GF
"	D01C09	D02C09	T	0.00	0.00	-0.31	30.00	55.00	24.69	82.55	3.34	FF
180	C32D00	C31D00	R	0.00	7.14	-7.96	30.00	55.00	24.18	82.55	3.41	FG
"	C32D05	C31D05	R	0.00	0.00	-0.22	30.00	55.00	24.78	82.55	3.33	FP
"	C32D10	C31D10	R	0.00	0.00	-0.43	30.00	55.00	24.57	82.55	3.36	FP
"	D32C18	D31C18	R	0.00	0.00	-5.65	30.00	60.00	24.35	82.55	3.39	GF

Table 1 (continued)

Angle	File 1	File 2	Typ	DT0 µs	DT1 µs	DT2 µs	T0 µs	T1 µs	T2 µs	Tav µs
0	C65U00	C64U00	T	-5.68	-2.37	0.88	21.23	24.54	27.79	24.52
"	C65U05	C64U05	T	-4.89	-1.61	1.62	20.12	23.39	26.62	23.37
"	C65U10	C64U10	T	-5.06	-1.60	1.72	19.94	23.40	26.72	23.35
"	C65U15	C64U15	T	-6.27	-2.86	0.42	18.73	22.14	25.42	22.10
"	C65U20	C64U20	T	-5.17	-1.75	1.53	19.83	23.25	26.53	23.21
"	C65U25	C64U25	T	-5.10	-1.73	1.52	19.90	23.27	26.52	23.23
"	C65U30	C64U30	T	-5.23	-1.87	1.40	19.77	23.13	26.40	23.10
"	D65C00	D64C00	T	-8.49	-5.20	-1.99	21.51	24.80	28.01	24.77
90	C01R00	C02R00	T	-2.72	0.43	3.70	22.28	25.43	28.70	25.47
"	C01R05	C02R05	T	-2.03	1.24	4.53	22.97	26.24	29.53	26.25
"	C01R10	C02R10	T	-2.44	0.45	3.46	22.56	25.45	28.46	25.49
"	C01R15	C02R15	T	-2.63	0.42	3.59	22.37	25.42	28.59	25.46
"	C01R20	C02R20	T	-4.18	-0.88	1.46	20.82	24.12	26.46	23.80
"	C01R25	C02R25	T	-4.35	-1.22	1.52	20.65	23.78	26.52	23.65
"	C01R30	C02R30	T	-4.77	-1.77	1.28	20.23	23.23	26.28	23.25
"	D01C09	D02C09	T	-3.73	-0.29	3.09	21.27	24.71	28.09	24.69
180	C32D00	C31D00	R	-11.27	-7.87	-4.74	20.87	24.28	27.40	24.18
"	C32D05	C31D05	R	-5.18	0.12	4.39	19.82	25.12	29.39	24.78
"	C32D10	C31D10	R	-5.23	-0.38	4.32	19.77	24.62	29.32	24.57
"	D32C18	D31C18	R	-10.06	-5.77	-1.11	19.94	24.23	28.89	24.35

Legend:

Angle: Transducer location with reference to the vertical up position.

File 1, File 2: File name convention is C for pressure records and D for orientation records. The first two digits indicate which transmitter to which reciever. The letters in the middle indicate the position of the transducer where D for down, U for up, R for right, L for left, and C for clockwise. The last two digits are the pressure in 100 psi (i.e. 05=500 psi etc) for C records or in amount of 10 degrees (i.e. 06=60 degress) from vertical up for D records.

Typ: Type, R for radially polarized and T for tangentially polarized.

Tc 1, Tc 2: Time correction for files 1 and 2.

DT: Time difference between File 1 and File 2 from cross correlation.

TPOS1, TPOS2: Trigger position for File 1 and File 2.

T: Time difference between File 1 and File 2.

L: Transducer separation.

V: Calculated velocity (L/T).

DT/DP: Calculated pressure gradient.

QUA: Quality of waveform, G for good, F for fair, and P for poor.

Table 2: Timing Analysis For The Stressmeter Field Test Data
----Pressure Effect. (see Table 1 for Legend)

Angle	File 1	File 2	Typ	Tc 1 µs	Tc 2 µs	DT µs	TPOS1 µs	TPOS2 µs	T µs	DT/DP	QUA
0	C65U00	C65U05	T	0.00	0.00	-0.42	30.00	30.00	-0.42	-0.08	GG
"	"	C65U10	T	0.00	0.00	-0.38	30.00	30.00	-0.38	0.01	GG
"	"	C65U15	T	0.00	0.00	-0.34	30.00	30.00	-0.34	0.01	GG
"	"	C65U20	T	0.00	0.00	-0.34	30.00	30.00	-0.34	0.00	GG
"	"	C65U25	T	0.00	0.00	-0.37	30.00	30.00	-0.37	-0.01	GG
"	"	C65U30	T	0.00	0.00	-0.41	30.00	30.00	-0.41	-0.01	GG
0	C64U00	C64U05	T	1.91	0.00	0.75	30.00	30.00	-1.16	-0.23	FF
"	"	C64U10	T	1.91	0.00	0.90	30.00	30.00	-1.01	0.03	FF
"	"	C64U15	T	1.91	0.00	-0.50	30.00	30.00	-2.41	-0.28	FF
"	"	C64U20	T	1.91	0.00	0.59	30.00	30.00	-1.32	0.22	FF
"	"	C64U25	T	1.91	0.00	0.54	30.00	30.00	-1.37	-0.01	FF
"	"	C64U30	T	1.91	0.00	0.41	30.00	30.00	-1.50	-0.03	FF
90	C01R00	C01R05	T	0.00	0.00	1.23	30.00	30.00	1.23	0.25	GG
"	"	C01R10	T	0.00	0.00	1.34	30.00	30.00	1.34	0.02	GG
"	"	C01R15	T	0.00	0.00	1.39	30.00	30.00	1.39	0.01	GG
"	"	C01R20	T	0.00	0.00	1.39	30.00	30.00	1.39	0.00	GG
"	"	C01R25	T	0.00	0.00	1.40	30.00	30.00	1.40	0.00	GG
"	"	C01R30	T	0.00	0.00	1.35	30.00	30.00	1.35	-0.01	GG
90	C02R00	C02R05	T	0.00	0.00	-0.73	30.00	30.00	-0.73	-0.15	FP
"	"	C02R10	T	0.00	0.00	-1.75	30.00	30.00	-1.75	-0.21	FP
"	"	C02R15	T	0.00	0.00	-1.67	30.00	30.00	-1.67	0.02	FP
"	"	C02R20	T	0.00	0.00	-0.43	30.00	30.00	-0.43	0.25	FP
"	"	C02R25	T	0.00	0.00	-0.43	30.00	30.00	-0.43	-0.00	FP
"	"	C02R30	T	0.00	0.00	-0.55	30.00	30.00	-0.55	-0.02	FP
180	C32D00	C32D05	R	0.00	0.00	1.17	30.00	30.00	1.17	0.23	FF
"	"	C32D10	R	0.00	0.00	1.46	30.00	30.00	1.46	0.06	FF
"	C32D05	C32D10	R	0.00	0.00	0.25	30.00	30.00	0.25	-0.24	FF
180	C31D00	C31D05	R	7.14	0.00	7.50	55.00	55.00	0.36	0.07	GP
"	"	C31D10	R	7.14	0.00	7.86	55.00	55.00	0.72	0.07	GP
"	C31D05	C31D10	R	0.00	0.00	0.08	55.00	55.00	0.08	-0.13	PP

Table 2 (Continued)

Angle	File 1	File 2	Typ	DT0 µs	DT1 µs	DT2 µs	T0 µs	T1 µs	T2 µs	Tav µs	QUA
0	C65U00	C65U05	T	-3.75	-0.41	2.91	-3.75	-0.41	2.91	-0.42	GG
"	"	C65U10	T	-3.74	-0.37	2.98	-3.74	-0.37	2.98	-0.38	GG
"	"	C65U15	T	-3.70	-0.34	3.01	-3.70	-0.34	3.01	-0.34	GG
"	"	C65U20	T	-3.71	-0.34	3.04	-3.71	-0.34	3.04	-0.34	GG
"	"	C65U25	T	-3.73	-0.38	3.01	-3.73	-0.38	3.01	-0.37	GG
"	"	C65U30	T	-3.76	-0.39	2.94	-3.76	-0.39	2.94	-0.41	GG
0	C64U00	C64U05	T	-2.38	0.74	3.89	-4.29	-1.18	1.98	-1.16	FF
"	"	C64U10	T	-2.19	0.89	4.00	-4.10	-1.02	2.09	-1.01	FF
"	"	C64U15	T	-3.61	-0.50	2.61	-5.52	-2.41	0.70	-2.41	FF
"	"	C64U20	T	-2.50	0.58	3.70	-4.41	-1.33	1.79	-1.32	FF
"	"	C64U25	T	-2.51	0.51	3.61	-4.42	-1.40	1.70	-1.37	FF
"	"	C64U30	T	-2.66	0.40	3.48	-4.57	-1.52	1.57	-1.50	FF
90	C01R00	C01R05	T	-2.11	1.19	4.62	-2.11	1.19	4.62	1.23	GG
"	"	C01R10	T	-2.01	1.30	4.73	-2.01	1.30	4.73	1.34	GG
"	"	C01R15	T	-1.98	1.37	4.80	-1.98	1.37	4.80	1.39	GG
"	"	C01R20	T	-2.00	1.36	4.82	-2.00	1.36	4.82	1.39	GG
"	"	C01R25	T	-2.00	1.36	4.83	-2.00	1.36	4.83	1.40	GG
"	"	C01R30	T	-2.04	1.30	4.79	-2.04	1.30	4.79	1.35	GG
90	C02R00	C02R05	T	-3.88	-0.67	2.37	-3.88	-0.67	2.37	-0.73	FP
"	"	C02R10	T	-4.84	-1.80	1.38	-4.84	-1.80	1.38	-1.75	FP
"	"	C02R15	T	-4.80	-1.71	1.51	-4.80	-1.71	1.51	-1.67	FP
"	"	C02R20	T	-3.62	-0.40	2.74	-3.62	-0.40	2.74	-0.43	FP
"	"	C02R25	T	-3.63	-0.40	2.73	-3.63	-0.40	2.73	-0.43	FP
"	"	C02R30	T	-3.74	-0.53	2.63	-3.74	-0.53	2.63	-0.55	FP
180	C32D00	C32D05	R	-2.73	1.24	5.01	-2.73	1.24	5.01	1.17	FF
"	"	C32D10	R	-2.15	1.44	5.09	-2.15	1.44	5.09	1.46	FF
"	C32D05	C32D10	R	-3.52	0.18	4.09	-3.52	0.18	4.09	0.25	FF
180	C31D00	C31D05	R	3.59	7.23	11.67	-3.55	0.08	4.53	0.36	GP
"	"	C31D10	R	3.48	7.56	12.55	-3.66	0.42	5.42	0.72	GP
"	C31D05	C31D10	R	-4.20	0.08	4.37	-4.20	0.08	4.37	0.08	PP

Table 3: Timing Analysis For The Stressmeter Field Test Data
----Orientation Effect. (see Table 1 for Legend)

File 1	File 2	Typ	Tc 1 µs	Tc 2 µs	DT µs	TPOS1 µs	TPOS2 µs	T µs	QUA
D32C18	D32C21	R	0.00	0.00	-0.75	30.00	30.00	-0.75	GG
"	D32C24	R	0.00	0.00	-0.93	30.00	30.00	-0.93	GG
"	D32C27	R	0.00	0.00	-0.57	30.00	30.00	-0.57	GF
"	D32C30	R	0.00	0.00	-0.81	30.00	30.00	-0.81	GG
"	D32C33	R	0.00	0.00	-1.09	30.00	30.00	-1.09	GG
"	D32C36	R	0.00	0.00	-0.28	30.00	30.00	-0.28	GG
D65C00	D65C03	T	0.00	0.00	-0.34	30.00	30.00	-0.34	GF
"	D65C06	T	0.00	0.00	-0.51	30.00	30.00	-0.51	GF
"	D65C09	T	0.00	0.00	-0.25	30.00	30.00	-0.25	GP
"	D65C12	T	0.00	0.00	-0.43	30.00	30.00	-0.43	GF
"	D65C15	T	0.00	0.00	0.24	30.00	30.00	0.24	GG
"	D65C18	T	0.00	0.00	0.90	30.00	30.00	0.90	GG
D01C09	D01C12	T	0.00	0.00	-0.81	30.00	30.00	-0.81	FF
"	D01C15	T	0.00	0.00	4.71	30.00	25.00	-0.29	FP
"	D01C18	T	0.00	0.00	0.47	30.00	30.00	0.47	FP
"	D01C21	T	0.00	0.00	-1.43	30.00	30.00	-1.43	FP
"	D01C24	T	0.00	0.00	-1.66	30.00	30.00	-1.66	FF
"	D01C27	T	0.00	0.00	0.61	30.00	30.00	0.61	FF

Table 4: Timing Analysis For The Stressmeter Field Test Data
-----Comparison. (see Table 1 for Legend)

Angle	File 1	File 2	Typ	Tc 1 µs	Tc 2 µs	DT µs	TPOS1 µs	TPOS2 µs	T µs	QUA
0	D65C00	C65U00	T	0.00	0.00	0.14	30.00	30.00	0.14	GG
"	"	D32C36	TR	0.00	0.00	1.11	30.00	30.00	1.11	GG
"	D64C00	C64U00	T	0.00	1.91	2.78	60.00	55.00	-0.31	GF
90	C01R00	D01C09	T	0.00	0.00	0.62	30.00	30.00	0.62	GF
"	"	D65C09	T	0.00	0.00	0.06	30.00	30.00	0.06	GP
"	D02C09	C02R00	T	0.00	0.00	0.04	55.00	55.00	0.04	FF
120	D65C12	D01C12	T	0.00	0.00	-0.05	30.00	30.00	-0.05	FF
150	D65C15	D01C15	T	0.00	0.00	4.79	30.00	25.00	-0.21	GP
180	D65C18	D01C18	T	0.00	0.00	0.06	30.00	30.00	0.06	GP
"	C32D00	D32C18	R	0.00	0.00	-0.09	30.00	30.00	-0.09	FG
"	D31C18	C31D00	R	0.00	7.14	-0.95	60.00	55.00	1.19	FG
"	D01C18	D32C18	TR	0.00	0.00	-1.09	30.00	30.00	-1.09	FG
210	D01C21	D32C21	TR	0.00	0.00	1.15	30.00	30.00	1.15	GP
240	D01C24	D32C24	TR	0.00	0.00	1.26	30.00	30.00	1.26	GF
270	D01C27	D32C27	TR	0.00	0.00	-0.60	30.00	30.00	-0.60	FG

Table 4 (Continued)

Angle	File 1	File 2	Typ	DT0 µs	DT1 µs	DT2 µs	T0 µs	T1 µs	T2 µs	QUA
0	D65C00	C65U00	T	-3.20	0.15	3.46	-3.20	0.15	3.46	GG
"	"	D32C36	TR	-2.05	1.13	4.26	-2.05	1.13	4.26	GG
"	D64C00	C64U00	T	-0.55	2.72	6.18	-3.64	-0.38	3.09	GF
90	C01R00	D01C09	T	-2.73	0.59	4.00	-2.73	0.59	4.00	GF
"	"	D65C09	T	-3.46	0.03	3.60	-3.46	0.03	3.60	GP
"	D02C09	C02R00	T	-3.41	0.03	3.50	-3.41	0.03	3.50	FF
120	D65C12	D01C12	T	-3.67	0.01	3.53	-3.67	0.01	3.53	FF
150	D65C15	D01C15	T	1.04	4.88	8.45	-3.97	-0.12	3.45	GP
180	D65C18	D01C18	T	-4.00	0.45	3.72	-4.00	0.45	3.72	GP
"	C32D00	D32C18	R	-3.80	-0.08	3.61	-3.80	-0.08	3.61	FG
"	D31C18	C31D00	R	-4.21	-1.01	2.37	-2.07	1.13	4.51	FG
"	D01C18	D32C18	TR	-5.02	-1.11	2.88	-5.02	-1.11	2.88	FG
210	D01C21	D32C21	TR	-2.01	1.07	4.39	-2.01	1.07	4.39	GP
240	D01C24	D32C24	TR	-2.09	1.21	4.65	-2.09	1.21	4.65	GF
270	D01C27	D32C27	TR	-3.67	-0.70	2.57	-3.67	-0.70	2.57	FG

11. REFERENCES

1. Christensen, M. (1986), Lawrence Livermore National Laboratory Internal Memo.

2. Creveling, J. B., F. S. Shuri, K. M. Foster, and S. V. Mills (1984), "In Situ Stress Measurements at the Spent Fuel Test--Climax Facility," Lawrence Livermore National Laboratory, UCRL-15628, May

3. Heuze, F. E. (1986), "The Unconventional Gas Program at Lawrence Livermore National Laboratory," Lawrence Livermore National Laboratory, UCID-20610, January.

4. Mao, N., J. Sweeney, J. Hanson, and M. Costantino (1983), "On the Feasibility of Using Sonic Techniques to Estimate In-Situ Stresses," Lawrence Livermore National Laboratory, UCRL-53424, June.

5. Mao, N. (1984), "Overcoring and Calibration of IRAD GAGE Stressmeters at the Spent Fuel Test in Climax Granite," Lawrence Livermore National Laboratory, UCID-20318, September.

6. Mao, N. (1987), "Shear Wave Transducer for Stress Measurements in Boreholes," United States Patent No. 4,641,520, Feb. 10.

7. Miller, F. E. and H. A. Doeringsfeld (1955), "Mechanics of Material", International Textbook Company, Pennsylvania, 514 P.

8. Timoshenko, S. and J. N. Goodier (1951), "Theory of Elasticity," McGraw-Hill Book Company, Inc., New York, 506 P.

12. ACKNOWLEDGMENTS

This research was performed as a part of the LLNL Unconventional Gas Program, under Contract W-7405-ENG-48 with the U.S. Department of Energy. Program monitoring is performed by Morgantown Energy Technology Center, Morgantown, WV. I would like to thank M. Christensen for developing the data acquisition software, R. Ruiz for helping me to setup the experiments, and F. Heuze, LLNL, Gas Program Leader, for reviewing the manuscript. Serata Geomechanics built the bladder system, and Precision Acoustics made the transducers. L. Grabowski carefully typed this document. I thank them for their help.